PROCEEDINGS

of the

2nd ONE-DAY WORKSHOP

on New Aspects and Perspectives in Nuclear Physics

DEPARTMENT OF PHYSICS
ARISTOTLE UNIVERSITY OF THESSALONIKI

APRIL 12, 2014

EDITORS
Ch. Moustakidis
G. Lalazissis
A. Pakou

HELLENIC INSTITUTE OF NUCLEAR PHYSICS

HELLENIC INSTITUTE OF NUCLEAR PHYSICS

PROCEEDINGS

OF THE

2nd ONE-DAY WORKSHOP

on New Aspects and Perspectives in Nuclear Physics

DEPARTMENT OF PHYSICS
ARISTOTLE UNIVERSITY OF THESSALONIKI
APRIL 12, 2014

2nd Hellenic Institute of Nuclear Physics
Workshop (HINPw2) - April 12, 2014

Physics Department, Aristotle University of Thessaloniki

HINPw2

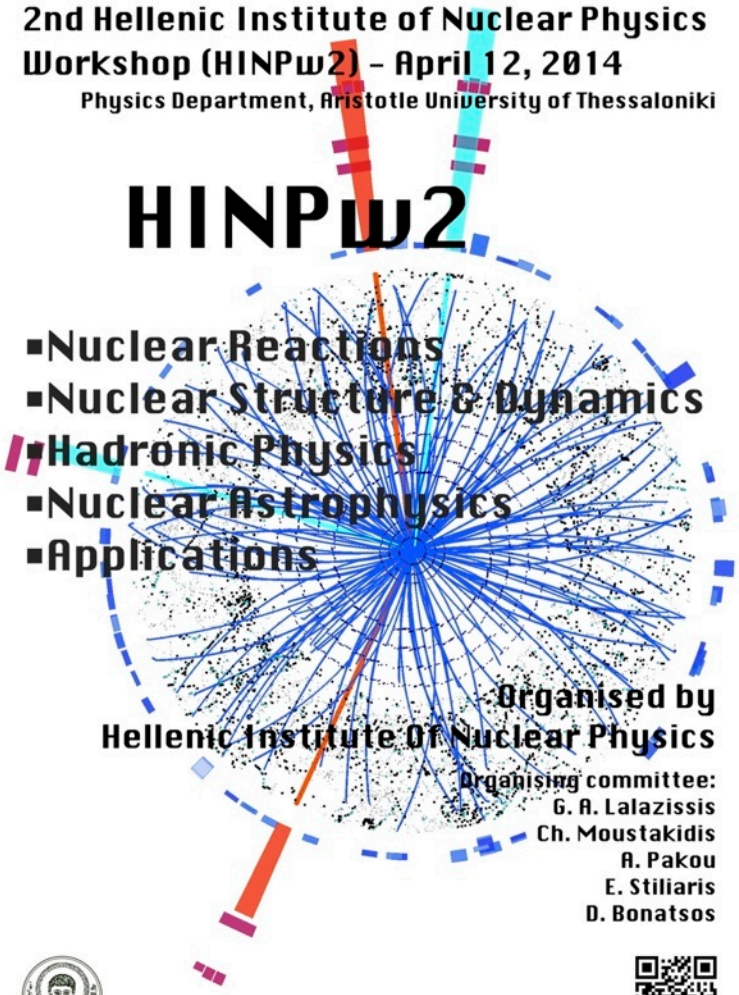

- Nuclear Reactions
- Nuclear Structure & Dynamics
- Hadronic Physics
- Nuclear Astrophysics
- Applications

Organised by
Hellenic Institute Of Nuclear Physics

Organising committee:
G. A. Lalazissis
Ch. Moustakidis
A. Pakou
E. Stiliaris
D. Bonatsos

http://hinpw2.physics.auth.gr

FOREWORD

This volume contains the proceedings of the 2nd annual Workshop on new Aspects and Perspectives in Nuclear Physics, held at the Department of Physics of the Aristotle University of Thessaloniki on 12th of April, 2014.

The Workshop was organized by the Hellenic Institute of Nuclear Physics (HINP) and was under the auspices of the Department of Physics of the Aristotle University of Thessaloniki and it was sponsored by the Research Committee of the Aristotle University of Thessaloniki.

About 160 participants came to the Workshop including more than 50 scientists and more than 100 undergraduate and graduate students. Especially, the enthusiastic response of the students was the most promising and encouraging event of the Workshop.

The topics of the Workshop were quite wide and included:

A. Nuclear Reactions
B. Nuclear Structure and Dynamics
C. Hadronic Physics
D. Nuclear Astrophysics
E. Applications

The various contributions are contained in this volume in the order of their presentation, according to the Workshop Program.

I would like to thank, on behalf of the Organizing Committee, the Department of Physics for hosting the Workshop also the Research Committee of the Aristotle University of Thessaloniki for the financial support. I would like also to express our thanks to all those who supported or assisted in the organization of the Workshop and to express my special thanks to Dr. Vasileios Psonis for his technical support during the preparation of the Workshop and the Proceedings editing.

Charalampos Moustakidis
On behalf of the organizing Committee

Thessaloniki, 20 March 2015

EPILOGUE

Dear colleagues,

Members of the virtual Hellenic Institute of Nuclear Physics (HINP)
Two days after our successful meeting in Thessaloniki and in the same spirit, I would like to make now the epilog.
Three years after its foundation, the main goal of HINP for SYNERGY between its members starts slowly but surely to develop.

- Two workshops have been successfully organized- one in Ioannina and one in Thessaloniki. Hopefully next year, a third one will take place in the University of Athens.
- Three programs have been submitted –Thalis between Ioannina, Thessaloniki and Athens (Pakou-Lalazissis-Stiliaris), Aristeia between Athens and Thessaloniki (Bonatsos-Lalazissis), Aristeia beteen Ioannina and Athens (Pakou-Stiliaris). No program was financed; however the effort was significant and marks our synergy actions.
- Two courses on technical matters concerning Monte-Carlo simulations with the tool kit GATE were offered from the University of Athens (Stiliaris) to the PhD students of the University of Ioannina. This effort should have been more advertised (I apologize for that) and in the future, efforts on that direction should be intensified and organized in a broader basis.
- A strong scientific collaboration was developed on equal basis between the laboratories of Ioannina and Athens (Pakou and Stiliaris groups) on research referring on reactions with weakly bound projectiles. Four proposals, which were submitted at LNL and LNS, have been approved on an ENSAR financial basis. The experiments have been performed and already the first published papers, mark the successful collaboration. Perhaps you have noticed the paper given in the HINPw2 workshop by Prof. Stiliaris which proves that a combined effort can give excellent results as long as it develops on an equal contribution from all sides.
- A webpage has been developed describing our scientific and educational achievements. Msc's, PhD's and numerous papers are out to be "evaluated" by the International Community of Nuclear Physics.
  Lets keep up the good work!, hoping that in the future the Community will be more generous with us.

We didn't have the time to discuss all the above in our meeting. We have preferred to give the stage to the hope of our community, the young graduate students, who raised the "excellency" flag of our Institution, presenting most of them, talks of high quality, being ready to give a worthy competition on an international level. Perhaps in the next meeting we could organize a competition between them rewarding the best presentation!

I will close this epilog of the 2nd HINP workshop in Thessaloniki, congratulating the local organizers and especially Babis Moustakidis for the excellent organization. I feel indebted to the numerous students who "filled up" the amphitheater applauding us to our efforts. The young generation of Greeks, remained there till the end of the

sessions exhibiting not only their interest on subjects of Nuclear physics but also their dignity, ethos and respect to their senior teachers.
Least but certainly not least, I ought from my heart to warmly acknowledge the participation in this meeting of Nicola Alamanos from IRFU, an exceptionally distinguished Nuclear Physicist abroad, who sacrificed his precious time, giving us an invited talk. He did actively participate in all sessions with continuous questions and comments to all the speakers enriching the quality of the workshop.

Thank you Nicola!
Thank you Thessaloniki! for the good work.
Members of HINP please keep up the good work!

With my best wishes for the Easter Holidays-ΚΑΛΗ Ανάσταση

Αθηνά Πάκου
Καθηγήτρια Φυσικής
Πρόεδρος του εικονικού Ελληνικού Ινστιτούτου Πυρηνικής Φυσικής

CONTENTS

The Institute of Research into the Fundamental laws of the Universe

Nicolas Alamanos

CEA, Centre de Saclay, IRFU/DIR

91191 Gif-sur Yvette Cédex, France

Abstract: The Institute of Research into the Fundamental laws of the Universe (IRFU), which is one of the seven institutes of the Physical Sciences Division (DSM – Direction des Sciences de la Matière) of the French atomic energy and alternative energies commission (CEA), is briefly presented with special mention on the activities in the domain of low energy nuclear physics. This text is part of "IRFU's 2020 Plan, 2008-2013 Report", a 353 pages document, which was made for the French evaluation agency (AERES).

1) The French atomic energy and alternative energies commission (CEA)

The CEA is a science and technology based research organization. It employs 16,000 employees and has a budget of €4.7 billion. CEA carries out research in four scientific areas: nuclear and renewable energies, information and health technologies, Very Large Research Infrastructures, and defense and security. In each of these fields, CEA relies on strong fundamental research carried out in collaboration with academia, and provides support to the industry. It is organized in 5 scientific divisions: the Physical Sciences Divisions (DSM), the Life Sciences Division (DSV), the Technological Research Division (DRT), the Nuclear Energy Division (DEN) and the Military Applications Division (DAM).

2) The Physical Sciences Division (DSM)

The (DSM) gathers CEA's fundamental research cluster in physics and chemistry. It employs 2,350 permanent CEA employees, 750 external collaborators and 750 PhD students and postdoctoral fellows. Its budget amounts to about €350 million. DSM is divided into seven institutes located on the CEA Grenoble, Cadarache, and Saclay centres with a local branch in Caen:

- GANIL, the Large Heavy Ion accelerator.
- INAC, the Nanoscience and Cyrogenics Institute.
- IPhT, the Institute for theoretical Physics.
- IRAMIS, the Saclay Institute of Matter and Radiation.
- IRFM, the Institute for Research on Magnetic Confinement Fusion.
- Irfu, the Institute for Research into the Fundamental law of the Universe.
- LSCE, the Laboratory for Climate and Environment Sciences.

3) The Institute of Research into the Fundamental laws of the Universe (Irfu)

Irfu has both a scientific and technological mission. The Institute has a matrix organization and calls upon the resources of its 6 departments for all projects. This organization enables Irfu to gather a coherent ensemble of professions, technological and financial means around each project. Located in Saclay, Irfu was set up in 1992 and succeeds Dapnia. It became an institute in 2008. Irfu gathers in one single department all astrophysics, nuclear physics, and particle physics activities and all associated technical units. These three disciplines enable researchers to probe the Universe in a complementary manner, from the infinitely small to the infinitely large.

In 2012, Irfu counted 823 employees in Saclay, including 619 permanent CEA researchers, 8 CNRS researchers, 9 academics, and 197 PhD students and postdoctoral fellows. Its budget amounts to €84 million including €53.7 million fungible subsidies. Irfu is one of the four administrative supervisors of APC, a laboratory that employs 200 people including 134 permanent researchers, and located on the Paris-Diderot University Campus. Irfu is also the administrative supervisor, together with CNRS, of the Modane Underground Laboratory (LSM Laboratoire Souterrain de Modane) and of the Champagne- Ardenne Neutrino Laboratory in Chooz.

Irfu counts six departments according to CEA's standard organization. These departments are quite significant in size and range from 100 to over 200 people.

Three physics departments: Each one of the three physics department focuses on one of the disciplines at the core of the Institute's research:

- SAP, the Astrophysics department, conducts research related to ground and space observations, as well as theory and simulations. This department includes professionals and facilities related to specific spatial instruments.
- SPhN, the nuclear physics department, covers research on nuclear structure, from quark-gluon plasma, to hadron physics and its applications.
- SPP, the particle physics department, combines accelerator experiments, observations of radiations from the cosmos, and observations of radioactive and reactor sources.

Three technological departments: The three other departments are technological units and gather the skills, tools, and facilities necessary to instrumental developments:

- SACM, the accelerator, cryogenics, and magnetism department, gathers the know-how on accelerators and magnets (superconducting or not).
- SEDI, the department for detector electronics and computer sciences, controls the whole production process and the real- or-simulated data processing process.
- SIS, the system engineering department, provides all instrumental developments with the necessary mechanical engineering and general instrumentation skills.

Irfu's policy is completely oriented toward international collaborations. The Institute is involved, together with the other French players, both at strategic level in international coordination's, and at operational level in scientific collaborations. So as to reach its ambitious objectives, the Institute develops collaboration networks with local (CEA, CNRS, universities, and CNES) and international (European Union, United States, Japan and China) partners and relies on large international organizations.

National collaborations

On a national scale, CNRS, in conjunction with universities and higher-education institutes, is the most active organization in research into the fundamental laws of the Universe. It counts many institutes active in this research area: IN2P3 for nuclear and particle physics, INSU for astrophysics and INP for parts of the theory. CNES is an essential partner for space astrophysics. Various types of organizations were set up to coordinate CEA, DSM and Irfu with their partners.

In the field of nuclear and high-energy physics (PNHE), Irfu participates in two thematic coordination committees (CCT) between CEA, CNRS, and the French Department of Higher Education and Research. Within this committee, IN2P3 and Irfu elaborate national prospects in this research area. Irfu is a member of the management committee of GANIL, the French national heavy ion accelerator.

In the field of astrophysics, Irfu is integrated into the INSU and CNES prospects on space research. It participates in CNES inter-organization committees (CIO) at general level and for each mission. Irfu participates or is represented in all CNES meetings. Irfu space activities involving SAP, SEDI and SIS are carried out under a contract agreement between CEA and CNES.

For large projects, Irfu participates in French steering committees with CNRS and the other players, among which the French Department of Higher Education and Research and the higher-education institutes concerned. For CTA, for instance, the steering committee comprises IN2P3, INSU, the Paris Observatory, the French Department of Higher Education and Research and Irfu. Irfu is also a member of the national programs and research groups coherent with its research.

Local collaborations

Irfu shares two Joint Research Units (UMR - Unité Mixte de Recherche) with Paris-Diderot University: AIM (Astrophysics, Instrumentation and Modeling Laboratory), a UMR in which INSU is also involved and which comprises most of SAP and one SEDI laboratory, and APC (AstroParticle and Cosmology Laboratory), a UMR with IN2P3 and the Observatory, located on Paris-Diderot University campus, where a dozen SAP and SPP researchers work. The LSM (Modane Underground Laboratory) and LNCA (Champagne-Ardenne Neutrino Laboratory) are operated together with IN2P3.

Irfu is also a member of two Scientific Interest Groups (GIS) together with CNRS and the associated education institutes: the SupraTech GIS for particle accelerators and the MoteSpace GIS for space instruments.

On the Saclay Plateau, Irfu and IPhT are major partners (40%) of the P2IO “Physics of the two infinities and of the Origins” LabEx which brings together CEA, CNRS, Paris-Sud University, and Ecole Polytechnique laboratories. The LabEx’s mission is to strengthen one of the main international clusters in physics of the two infinities. It benefits from the support of the exceptional concentration of laboratories and technological means on the Paris-Saclay campus. Irfu has been in charge of its coordination since 2012. Under the Paris-Saclay IdEx, the setup of a department with a scope close to this of P2IO has been proposed. As indicated in the 2010 report of the French Academy of Science “Evolution of French scientific space research: perspectives over 15 years”, the Saclay plateau is also a hot spot for space research. The plateau gathers a wide range of skills and research topics and Irfu is one of its major players. This cluster is currently being re-organized under the Paris-Saclay IdEx project.

Thanks to its AIM and APC joint research units, Irfu is also a partner of the UnivEarths (Paris-Diderot University) and Focus (Grenoble) LabEx.

International collaborations

Research on the infinitely large and the infinitely small require large instruments. The international scientific community gets together around co-managed instruments. CERN is a pioneering example of such collaborations. Irfu collaborates on the large facilities in its field from accelerators, to observatories, to satellites.

Irfu participates in the international coordination and governance of these organizations, disciplines, and experiments. Its strategy is in line with national and international roadmaps and it contributes actively to the prospective studies leading to their establishment, in common agreement with European intergovernmental organizations (CERN, ESA, ESO), European coordination bodies (ApPEC, NUPECC), the French Space Agency (CNES), the CNRS institutes (INSU and IN2P3) and the French Department of Higher Education and Research.

Irfu has chaired the group of nine large laboratories participating in CERN's experiments and participates in the European strategy meetings of the CERN Council. It has representatives at ApPEC/ ASPERA and NUPECC, respectively the European structures of cooperation and consultation for astroparticle and nuclear physics. It participates in bilateral meetings between France (CEA-CNRS) and the BMBF, the STFC, the INFN, the DOE and the KEK.

On an international scale, Irfu's action focuses on Europe with very strong partnerships in Germany (Desy, GSI), Spain (CIEMAT), and Italy (INFN, ENEA). Last but not least, since the 6th Contract Program for Research & Development, the European Union has become Irfu's second financial partner right after CNES.

Outside Europe, Irfu has strong partnerships in the US with Fermilab, JLab, SLAC, and NASA and in Japan with KEK, JAEA and Riken. Irfu works with CNRS in many Associated European and International Laboratories (AEL/AIL: China, Japan, India, Vietnam, Italy, and Poland).

3-1) Low energy nuclear physics - Nuclear forces and nuclear structure

In this part of this article I will present few aspects concerning IRFU's contributions in the domain of low energy nuclear physics.

Nuclei are complex quantum objects. The force which binds the nucleons is an effective force between composite particles linked in a complex manner to the strong interaction between the quarks and gluons of which they are comprised. Several parameters can be modified to test the properties of the nuclei and reveal their structure and the origin of their cohesion and thus deduce the properties of the interactions between nucleons. Irfu therefore focused its research on studying:

- Exotic nuclei, extremely rich in neutrons or protons and used to test the stability limits.
- Deformed nuclei, systems presenting spontaneous symmetry breaking.
- Super-heavy nuclei, systems stabilized against fission by the quantum structure of the nucleus.

SPIRAL2 is a world-class facility which will enable all of these questions to be addressed. The decision to build SPIRAL2, a large facility for intense stable and exotic beams on a par with the best in the world, and associated with a range of high-performance and versatile detection systems, was taken in 2005. It is the French community's priority. SPIRAL2 is internationally supported, as demonstrated by the large number of letters of intent for various experimental programs.

Irfu is in charge of the contribution by CEA (excluding GANIL) to the project. In this respect, Irfu is a CEA/DSM member of the SPIRAL2 steering committee with IN2P3.
From the technical viewpoint, Irfu has considerable responsibility in the construction of the machine with:

- The deuterons injector.
- The RFQ, radio-frequency quadrupole accelerator cavity.
- The type A accelerator cavities and associated cryomodules.
- The control systems.

This activity has represented an average of more than 25 full-time equivalents every year since about 2005.
At the same time, Irfu is preparing future experiments giving priority to the NFS and S3 facilities, which are part of the phase 1 of the project and should be operational at 2015 or 2016. NFS comprises a neutron secondary beam line for which Irfu, as spokesperson for a letter of intent, is developing an experimental program focused on fission. Irfu has responsibilities both the development of the line and in finalizing an instrument for detecting fission fragments.
Irfu is the technical coordinator and joint manager for the S^3 spectrometer project and joint spokesperson for the letter of intent concerning very heavy nuclei spectroscopy. The S^3 super separator spectrometer will use extremely intense and stable ion beams from the SPIRAL2 linear accelerator, in particular to study and synthesize heavy and super- heavy nuclei.

The study of exotic nuclei

Direct nuclear reactions are a means of probing the structure of nuclei. The physicists at Irfu have developed their expertise in the field of exotic nuclei and for many years have focused on the use of hydrogen-induced direct reactions, such as inelastic scattering, low-energy nucleon transfer or ejection of nucleons at intermediate energies. In theory, these reactions can provide information about the initial state of the ejected or transferred nucleon before the reaction. Experiments performed at Riken and GANIL with the MUST2 detector were able to analyze the limits of the current reaction mechanisms theoretical approaches and to quantify their validity domain for the study of exotic nuclei. The data obtained act as the reference for modelling the knockout and transfer of a nucleon in the considered energy domain.
At the same time, the past period was marked by numerous technical developments paving the way for future experiments designed to observe reactions with exotic nuclei.
An active target, both gaseous target and tracker (Actar-TPC), will be used to measure particles emitted at very low energy. Considering the low intensities of the radioactive nuclei beams, these systems are ideal for studying induced reactions because as the reactions occur within the detector they cannot escape measurement. Time projection chambers (TPC) require specific electronic developments which are the subject of the GET (General Electronics for TPC) project. This project is run by Irfu within the framework of a major international collaboration.

Spectroscopy of nuclei extremely rich in neutrons is developing, notably within the MINOS program, which has benefited from ERC funding since November 2010. The experimental technique consists in using thick hydrogen targets and in detecting de-excitation gamma photons emitted by the nuclei produced. To correct the extremely important Doppler Effect at the relativistic energies at RIKEN in Japan and GSI/FAIR in Germany, the reaction vertex is determined by measuring the protons with a Micromegas TPC.
Neutron-induced reactions are also a great spectroscopic tool to probe the nuclear structure in the continuum near the neutron separation energy. The experiments performed at the n_TOF facility at CERN allowed characterizing specifically this structure for medium and heavy mass nuclei. These measurements also serve as an anchoring point for nuclear level-density calculations, which are critical in issues related to stellar nucleosynthesis. Irfu is spokesperson for the commissioning phase of the second experimental area of n_TOF and for the development of pixelized detectors for the characterization of the neutron beam.

Study of super-heavy nuclei

In recent years, Irfu developed a research program in the field of very heavy or even super-heavy nuclei. Irfu more particularly specialized in studying odd nuclei (Md, Lr, etc.) and "K" isomer states, excited states with a very long lifetime, which can in certain heavy nuclei increase their stability to spontaneous fission. These K isomers, with a relatively pure structure, because they correspond to nucleons in clearly defined orbits, provide valuable information on the structure of nuclei and allow extreme testing of the effective interactions used.

The spectroscopy experiments are performed at Jyväskylä University (Finland) which is currently the leading laboratory in this field. For example, Irfu was the spokesperson for the first combined gamma and electron spectroscopy experiment which discovered numerous new states in the nucleus of ^{251}Md. Furthermore, spectroscopy was recently carried out on ^{256}Rf, the heaviest nucleus (Z=104) ever studied using gamma spectroscopy. This experiment, which revealed a rotational type of gamma spectrum, invalidated all the models which failed to predict deformation at Z=104. Implementation of Vamos-GFS, Gas-Filled VAMOS Spectrometer with the MUSETT focal plane at GANIL in 2015, once coupling with AGATA will increase sensitivity by at least one order of magnitude for the spectroscopy of heavy nuclei. In the medium term, with S3, Irfu will support a research program devoted to the synthesis and spectroscopy of heavier nuclei.

Study of the deformation of nuclei

In recent years, Irfu has built up a robust experimental program to study the "deformation" of nuclei, a fundamental property reflecting the spatial distribution of nucleons. The study more particularly focuses on open shell nuclei because in these nuclei, the occupancy of certain particular orbits can lead to deformation. In certain nuclei, shape coexistence phenomena, in which two extremely different configurations have very similar energy, can even be observed. Irfu was the spokesperson for several experiments on this subject using the EXOGAM multi-detector at GANIL, for instance the recent experiment which examined the shape of fission fragments by measuring the lifetime of their excited states. This analysis focused on the nuclei of Zr, Ru, Mo and Pd with mass A~100, a highly

interesting region, because rapid shape changes from one isotope to another are predicted in it. Irfu is heavily involved in all the phases of the AGATA detector: definition of the scientific program (spokesperson for experiments and letter of intent, member of the steering committee, campaign coordinator at GSI), development, construction and integration. After the measurement campaign in Legnaro, in 2012, the AGATA demonstrator was installed at GSI. During the AGATA campaign in Legnaro, Irfu was the spokesperson for a spectroscopy experiment on nuclei of 70-74Zn, rich in neutrons around neutron number N=40. This experiment highlights rare properties which have yet to be understood, such as the low collectivity of excited states by comparison with usual rotational or vibrational type behaviors. Additional measurements in this mass region were accepted at HIE-Isolde (74-80Zn) or are already being analyzed (^{70}Zn at HIL- Warsaw).

Together with GANIL and the AGATA collaboration, Irfu is now preparing the future AGATA campaign GANIL for the period 2014-2016. Jointly with GANIL, Irfu is co-promoter of an ANR request for the VAMOS project in gas-filled mode, and for four letters of intent.

Theory: revolutionary ab-initio approaches

In parallel with the above mentioned experimental researches, theoretical studies are being carried out for the development of ab initio and density-functional models, with the aim of understanding and predicting the properties of the structure of the nucleus. Drawing on the constantly increasing power of the large high-performance computers (GENSI), Irfu recently achieved a major step forward by developing and implementing the “self-consistent Gorkov Green’s function” for open shell nuclei, an ab initio method for describing nuclei based on first principles and realistic nucleon-nucleon interaction potentials. This progress, which allows a significant extension of the scope of methods “without phenomenological parameters” to mid-mass, open shell nuclei - and therefore those with pairing correlations - is crucial for the interpretation of current and future experiments with new exotic beam facilities.

3-2) Few aspects concerning the production and academic attractiveness of the Institute

Number of articles published

The annual number of publications in peer-reviewed journals has been rising regularly. Over the period 2008-2012, this number practically doubled, reaching 936 peer-reviewed publications. 2013 should be even slightly better than 2012, because by mid-2013, the number of publications is already 5% up on 2012 at the same date. Of the 4,063 articles published by the Institute during the period 2008–mid-2013, 388 –some 10 %–appeared in Nature, Science or Physical Review Letters and 295 in Physics Letters B. Over this same period, Irfu also published more than 1,000 conference articles, of which one-third were in peer-reviewed journals. In 2012, Irfu made a contribution of nearly 20% to CEA publications.

Citations and impact factor

At the same time, the institute’s impact factor has progressed. It is today the highest within the DSM. This impact factor is the actual citations picture, in other words the average number of citations per article and per year integrated over the period. Overall, the 4,063 articles published from 2008 to mid-2013 were cited 81,900 times. It should be noted that 322 of these articles – some 8% – have

already exceeded 50 citations and 108 articles more than 100. A second indicator of the quality of the institute's publications is the proportion of its articles listed in the world's top 0.01%, 0.1% and 1% of the most cited articles in physics or in all disciplines taken together. For example, on 29th September 2013, 6 articles from 2012, (0.64% of the Irfu's articles in 2012), were ranked in the top 0.01%, more than 2% in the top 0.1%, 13% in the top 1% and nearly 43% in the top 10%. The most cited articles correspond to the major advances, for example in 2012, the discoveries at the LHC with ATLAS and CMS, the results from Double Chooz and the catalogue of Fermi sources. In all these publications which come from the main collaborations, Irfu played a major role. In ATLAS and CMS the institute was well-positioned for the analysis of the key channels for the decay of particles involving photons and muons. It was the originator of the Double Chooz experiment and is responsible for the Fermi catalogue. In the previous years, the situation was similar with other programs, such as Herschel. The growth in the number of publications, their impact and their visibility is the result of this scientific policy adopted by Irfu, which is to play a key role in experiments and collaborations with significant potential for progress and discoveries.

Researchers Recognized by awards, distinctions and funding

The recognition received by the researchers and their work can be seen by the list of awards and distinctions. Since 2008, the physicists at the institute have received about forty awards and distinctions which are among the most prestigious in their fields. Particularly worthy of note are three prizes awarded by the French Academy of Sciences, the prize of the Royal Academy of Belgium, the scientific grand prize from the Simone and Cino-del-Duca Foundation, a silver and two bronze CNRS medals, as well as three Joliot-Curie prizes from the French Society of Physics, obtained three years in a row, in 2010, 2011, and 2012. Since 2011, the Irfu staff has included a member recently elected to the French Academy of Sciences. These prizes are supplemented by the 12 ERC grants, including 3 advanced grants. This represents a highly significant share of all French grants in these disciplines. In the field of subatomic physics, Irfu obtained 4 of the 8 French grants – although it only represents 10% of the national community – and in astrophysics 8 of the 23 grants, or some 35% of the French grants – even though it accounts for less than 6% of the community.

From 2008 to mid-2013, the researchers at the institute also obtained more than 150 research contracts from the ANR (French national research agency), the Île-de-France region, and FP6 (Sixth Framework Program) and FP7 (Seventh Framework Program). The annual amounts thus received are about ~1 M€ for the ANR, ~0.8 M€ for the local authorities and 5 M€ for Europe. These contracts are supplemented by those obtained under the EquipEx (S3, Cilex) and LabEx (P2IO, UnivEarthS, Focus) investing in the future programs, for an amount of about one million euros per year.

Communicating researchers

The visibility and attractiveness of Irfu's researchers also comes from their commitment to disseminating knowledge to students, the general public and the media. Over the past five years, most researchers have taken part in this type of action at various levels. On the occasion of important discoveries or events, more than about fifty researchers were frequently contacted by the public and the media: TV appearances, podcasts, radio interviews, conferences, scientific films, etc. Irfu's members also include about fifty authors of more than a hundred science popularization books and sixty or so academic courses and books.

Editors in scientific reviews and recognized scientific experts

Eight physicists from the institute are members of the editorial boards of peer-reviewed science journals. One of them is member of the board of the supervisory editors for the Nuclear Physics A review, a second is editor-in-chief and managing reviews editor of the European Physical Journal A (EPJ A). The number of editorial responsibilities stands at 17. Furthermore, three physicists from the institute are also on the editorial committees of the Scholarpedia web encyclopedia and one of them is editor of the Nuclear Physics section of Scholarpedia. These permanent editors are supplemented by the numerous editors of the proceedings of the conferences they organize. It should also be noted that virtually all of the researchers at the institute have been a referee in recent years. If we now analyze the list of participations on science boards, given in a related document, we can see more than 220 mandates, generally of several years. This participation by the physicists concerns the most important boards in our disciplines, in particular those of international organizations such as ESO and the CERN, as well as those of the main laboratories in the institute's disciplines. We could mention the SPC and the SPSC of CERN, the ERC juries, the ANR committees, or ESA's AWG (see list in related document).

Recruiting the best in the world

The institute attaches particular importance to the quality of the researchers it hires, as demonstrated by its international calls for candidate applications. Over the period 2008-2013, 63 staff were hired on a full-time basis. This comprised 46 research-engineers (including 13 women) and 17 technicians (1 woman). Of the 46 research-engineers, the professional goal of 21 of them is to produce equipments - we will call them engineers - and the goal of the 25 others is to produce scientific- the physicists.

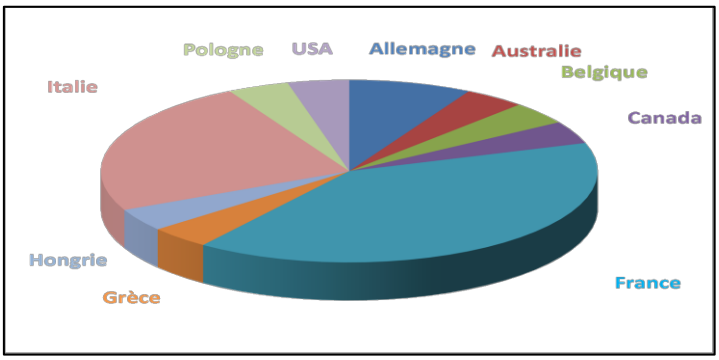

Each time a vacancy arises; there is considerable pressure, with dozens of candidates for each position. It is worth noting, and this is probably a sign of the institute's considerable openness that of the 25 physicists hired over the 2008-2013 period, 15 hold diplomas or PhDs obtained in countries other than France.

This breakdown shows the diversity of the origins of the young staff taken on at Irfu. The attractiveness of Irfu can also be measured by the PhDs and post-doctoral staff. During the period, 229 PhDs worked at Irfu, with the main limit on this number being funding rather than the candidates. It must be pointed out that the quality of the PhDs receiving CEA funding is strictly controlled by the Haut Commissaire. During the period 2008 – mid-2009, the number of PhDs in the institute rose significantly, up from 19 theses defended in 2008 to 33 in 2012. The post-doctoral flow is also a sign of attractiveness and, during the period, nearly 70 post-doctoral staff permanently reinforced the institute, giving a total of 352 men-years.

Production of neutron-rich nuclei in peripheral heavy-ion collisions in the energy range 15–25 MeV/nucleon

P.N. Fountas and G.A. Souliotis*

Laboratory of Physical Chemistry, Department of Chemistry,
National and Kapodistrian University of Athens, Athens 15771, Greece
*soulioti@chem.uoa.gr

Abstract

The production cross sections of projectile-like fragments from collisions of ^{86}Kr projectiles with $^{64,58}Ni$ and $^{124,112}Sn$ targets at 15 and 25 MeV/nucleon are studied systematically with emphasis on the neutron-rich isotopes. Our recent experimental data are compared with calculations employing a hybrid approach. The dynamical stage of the projectile-target interaction was described with either the phenomenological deep-inelastic transfer (DIT) model or the microscopic constrained molecular dynamics model (CoMD). For the de-excitation of projectile-like fragments, the statistical multifragmentation model (SMM) or the binary-decay code GEMINI were employed. A good agreement with the experimental results was obtained. We point out that our current understanding of the reaction mechanism at beam energies below the Fermi energy suggests that such nuclear reactions, involving peripheral nucleon exchange, can be exploited as a novel route to access extremely neutron-rich isotopes toward the r-process path and the hard-to-reach neutron drip-line.

Introduction

The study of the nuclear landscape toward the astrophysical r-process path and the neutron drip-line have recently received special attention by the nuclear physics community (see, e.g., [1,2] and references therein). Closely related to this effort is the efficient production of very neutron-rich nuclides which constitutes a central issue in current and future rare isotope beam facilities (see, e.g., [3–11]).

Neutron-rich nuclides are mainly produced by spallation, fission and projectile fragmentation [12]. Spallation is an efficient mechanism to produce rare isotopes for ISOL-type techniques [13]. Projectile fission is appropriate in the region of light and heavy fission fragments (see, e.g., [14] for recent efforts on ^{238}U projectile fission). Finally, projectile fragmentation offers a universal approach to produce exotic nuclei at beam energies above 100 MeV/nucleon (see, e.g., [15,16]). This approach is, nevertheless, based on the fact that optimum neutron excess in the fragments is achieved by stripping the maximum possible number of protons (and a minimum possible number of neutrons).

To reach a high neutron-excess in the products, apart from proton stripping,

it may be necessary to capture neutrons from the target. Such a possibility is offered by reactions of nucleon exchange at beam energies from the Coulomb barrier [17,18] to the Fermi energy (20–40 MeV/nucleon) [19,20]. Detailed experimental data in this broad energy range are scarce at present [18,21,22]. In multinucleon transfer and deep-inelastic reactions near the Coulomb barrier [18], the low velocities of the fragments and the wide angular and ionic charge state distributions may limit the collection efficiency for the most neutron-rich products. The reactions in the Fermi energy regime combine the advantages of both low-energy (i.e., near and above the Coulomb barrier) and high-energy (i.e., above 100 MeV/nucleon) reactions. At this energy, the synergy of the projectile and the target enhances the N/Z of the fragments, while the velocities are high enough to allow efficient in-flight collection and separation.

Our initial experimental studies of projectile fragments from 25 MeV/nucleon reactions of ^{86}Kr on ^{64}Ni [19] and ^{124}Sn [20] indicated substantial production of neutron-rich fragments. Motivated by recent developments in several facilities that will offer either very intense primary beams [5,8] at this energy range or re-accelerated rare isotope beams [4,5,8,9], we continued our experimental studies at 15 MeV/nucleon [23]. In this contribution, after a short overview of the experimental measurements, we present a systematic calculation of the production cross sections based on either the phenomenological deep-inelastic transfer (DIT) model or the microscopic constrained molecular dynamics model (CoMD). The good description of the experimental results with the CoMD code, as well as, with a properly modified version of the DIT code, suggest the possibility of using the present theoretical framework for the prediction of exotic nuclei employing radioactive beams that will soon be available in upcoming facilities. As an example, we present the production cros sections and the rates of neutron-rich nuclei using a radioactive beam of ^{92}Kr at 15 MeV/nucleon.

Outline of Results and Comparisons

A detailed presentation of the experimental results appear in [23] in which the mass spectrometric measurements of production cross sections of neutron-rich projectile fragments from the reactions of a 15 MeV/nucleon ^{86}Kr beam with ^{64}Ni, ^{58}Ni and ^{124}Sn, ^{112}Sn targets are given. We also note that the experimental results of the 25MeV/nucleon reactions and the relevant procedures are described in detail in our articles [19–22].

In Fig. 1 we present the experimental mass distributions of elements with Z = 35–30 of the reaction ^{86}Kr(15 MeV/nucleon)+^{64}Ni [23] compared to the calculations with the CoMD code [24,25] combined with the de-excitation codes SMM [26] (solid line) and GEMINI [27] (dotted line), used for the de-excitation of the quasiprojectiles emerging after the dynamical stage. The results of the calculations are in overall agreement with the experimental data

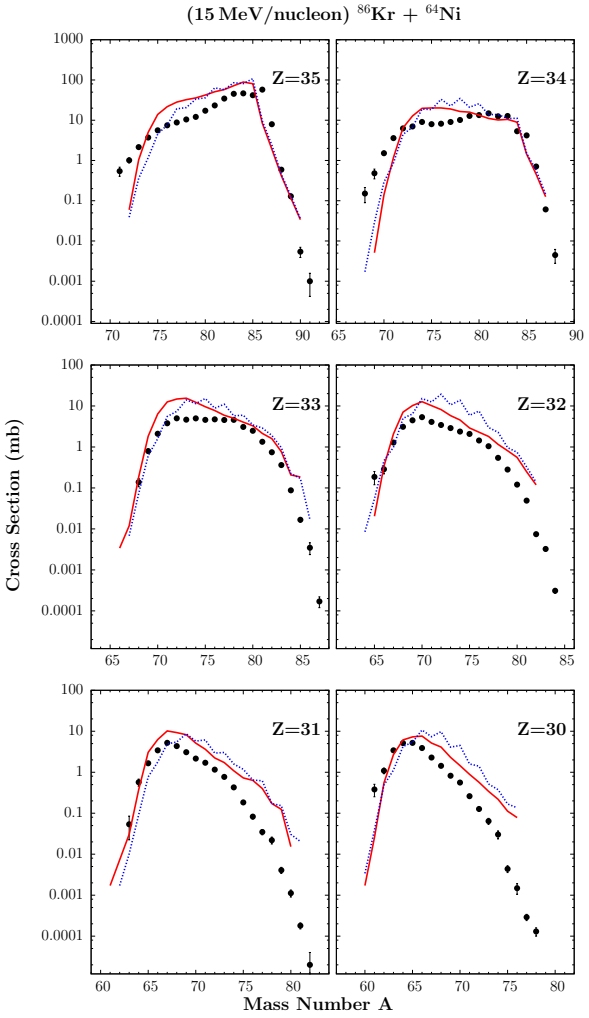

Fig. 1. (Color online) Experimental mass distributions (symbols) of elements with Z = 35–30 observed in the reaction ^{86}Kr(15 MeV/nucleon)+^{64}Ni [23] compared to the results of CoMD/SMM calculations (solid red line) and CoMD/GEMINI calculations (dotted blue line).

especially for the isotopes close to the projectile with Z = 35–32. We also observe that the microscopic CoMD model is able to describe even the rare neutron-rich products from this reaction that are the products for our main interest. The overestimation of the cross sections for the products with Z = 31,30 is related to issues of the excitation energy as calculated by CoMD and are currently under further investigation.

Subsequently, motivated by our previous studies [19,20], we employed Tassan-Got's phenomenological model of deep inelastic transfer (DIT) [28] coupled with SMM [26] or GEMINI [27]. The results of this standard version of DIT were not satisfactory. We thus proceeded with our modified version of the DIT model (DITm) [29] in which we have introduced a detailed description of the nuclear surface and the neutron skin of the involved nuclei. In Fig 2, we present the experimental mass distributions of elements with Z = 35–30 of the

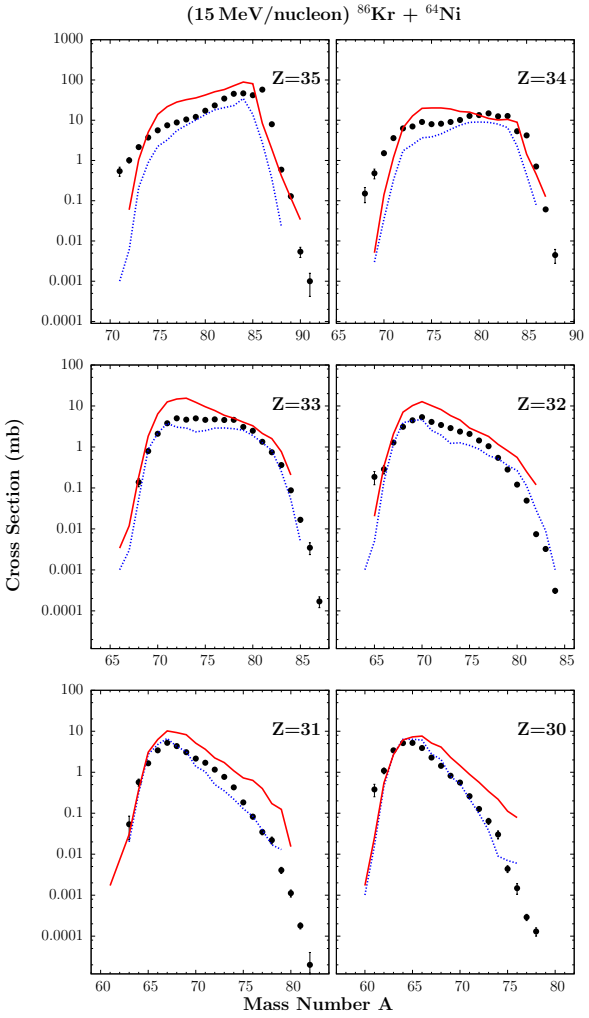

Fig. 2. (Color online) Experimental mass distributions (symbols) of elements with Z = 35–30 observed in the reaction ^{86}Kr(15 MeV/nucleon)+^{64}Ni [23] compared to the results of CoMD/SMM calculations (solid red line) and DITm/SMM calculations (dotted blue line).

reaction ^{86}Kr(15 MeV/nucleon)+^{64}Ni [23] and compare them to the results of the modified DIT (DITm) calculations (dotted line) and to the results of the CoMD calculations (solid line) using SMM as the de-excitation code. From this figure we observe that the modified DIT code describes the experimental results rather well at these beam energies. Moreover, it can better describe the products further away from the projectile, that cannot be well described by CoMD, as we mentioned previously.

We mention that a thorough comparison of the data with the calculations for the 15 MeV/nucleon, as well as the 25 MeV/nucleon reactions has been performed that appears in [30]. After this systematic comparison of the calulations with the experimental data of the stable ^{86}Kr beam, we proceeded to investigate what results we would obtain by using a neutron-rich radioactive beam, such as ^{92}Kr. In Fig. 3 we present again the experimental mass dis-

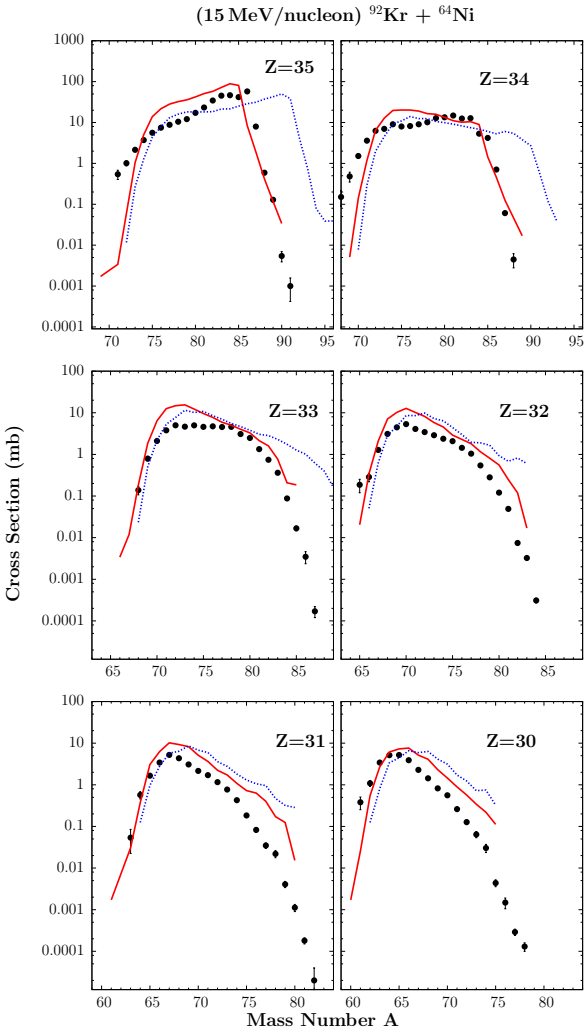

Fig. 3. (Color online) Experimental mass distributions (symbols) of elements with Z = 35–30 observed in the reaction ^{86}Kr(15 MeV/nucleon)+^{64}Ni [23], calculations CoMD/SMM for the reaction ^{86}Kr(15 MeV/nucleon)+^{64}Ni (solid red line), calculations CoMD/SMM for the reaction ^{92}Kr(15 MeV/nucleon)+^{64}Ni (dotted blue line).

tributions (black symbols) of the reaction ^{86}Kr(15 MeV/nucleon)+^{64}Ni, the CoMD/SMM calculations for this reaction (solid line) and, furthermore, the CoMD/SMM calculations for the reaction ^{92}Kr(15 MeV/nucleon)+^{64}Ni (dotted line). We observe that by using the neutron-rich radioactive beam of ^{92}Kr, we obtain more neutron-rich products. This is primarily true for the isotopes near the projectile. We point out that, e.g., for bromine (Z=35), isotopes that have up to 15 more neutrons (A = 96) than the corresponding stable isotope (A = 81) can be obtained. This observation indicates that by using neutron-rich radioactive beams, and through the mechanism of peripheral multinucleon transfer, we will have the possibility to produce even more neutron-rich nuclides toward neutron drip line.

In Table I, we present the predicted cross-sections and the production rates

Table 1
Cross sections and rate estimates (last column) of very neutron-rich isotopes from the reaction ^{92}Kr (15 MeV/nucleon) + ^{64}Ni. For the rates, a radioactive beam of ^{92}Kr with intensity 0.5 pnA (3.1×10^9 particles/sec) is assumed to interact with a ^{64}Ni target of 20 mg/cm^2 thickness.

Rare Isotope	Reaction Channel	Cross Section (mb)	Rate (sec^{-1})
^{93}Kr	-0p+1n	18.8	1.1×10^4
^{94}Kr	-0p+2n	2.3	1.3×10^3
^{95}Kr	-0p+3n	0.63	3.8×10^2
^{96}Kr	-0p+4n	0.2	1.2×10^2
^{92}Br	-1p+1n	4.5	2.7×10^3
^{93}Br	-1p+2n	0.75	4.5×10^2
^{94}Br	-1p+3n	0.078	47
^{95}Br	-1p+4n	0.040	23
^{96}Br	-1p+5n	0.008	5
^{90}Se	-2p+0n	2.7	1.6×10^3
^{91}Se	-2p+1n	0.6	3.5×10^2
^{92}Se	-2p+2n	0.12	70
^{93}Se	-2p+3n	0.04	23

of neutron rich isotopes from the reaction of the radioactive beam of ^{92}Kr (15 MeV/nucleon) with ^{64}Ni. For the rate calculations, the ^{92}Kr beam with intensity 0.5 pnA (3.1×10^9 particles/sec) is assumed to interact with a ^{64}Ni target of 20 mg/cm^2 thickness. We see that we have the possibility to produce extremely neutron-rich isotopes in these energies with the use of re-accelerated radioactive beams, such as ^{92}Kr, that will be available in upcoming rare-isotope facilities (e.g. [10,11]).

Summary and Conclusions

In summary, we perfomed a systematic study of the production cross sections of projectile-like fragments from collisions of ^{86}Kr projectiles with ^{64,58}Ni and ^{124,112}Sn targets at 15 and 25 MeV/nucleon with emphasis on the neutron-rich isotopes. Our experimental data were compared with systematic calculations employing a two-step approach. The calculations for the dynamical stage of the projectile-target interaction were carried out using either the

phenomenological deep-inelastic transfer (DIT) model or the the microscopic constrained molecular dynamics model (CoMD). For the de-excitation of the projectile-like fragments, the statistical multifragmentation model (SMM) or the binary-decay code GEMINI were employed. An overall good agreement with the experimental results was observed. With the current understanding of the reaction mechanism at these beam energies, we suggest that these nuclear reactions, involving peripheral nucleon exchange, be exploited as an efficient route to access neutron-rich rare isotopes toward the r-process path and the neutron drip-line. Therefore, future experiments in several accelerator facilities [12] can be planned that will enable a variety of nuclear structure and nuclear reaction studies in unexplored regions of the nuclear chart.

Acknowledgement

We are thankful to M. Veselsky and A. Bonasera for their continued contribution to the present project. Furthermore, we wish to thank Y.K. Kwon and K. Tshoo of the KOBRA team of RISP (Korea) for their motivation, support and recent discussions on our proposed RIB production approach.

References

[1] J. Erler et al, Nature **486**, 509 (2011).

[2] J. Äystö, W. Nazarewicz, M. Pfützner, C. Signorini, eds, Proceedings of the Fifth International Conference on Exotic Nuclei and Atomic Masses (ENAM'08), Ryn, Poland, September 7–13 (2008); Eur. Phys. J. A **42** (2009).

[3] D. F. Geesaman, C. K. Gelbke, R. V. F. Janssens, B. M. Sherrill, Ann. Rev. Nucl. Part. Sci. **56**, 53 (2006)

[4] FRIB main page: www.frib.msu.edu

[5] GANIL main page: www.ganil.fr

[6] GSI main page: www.gsi.de

[7] RIBF main page: www.rarf.riken.go.jp/Eng/facilities/RIBF.html

[8] ATLAS main page: www.phy.anl.gov/atlas/facility/index.html

[9] EURISOL main page: www.eurisol.org

[10] RISP main page: www.risp.re.kr/eng/pMainPage.do

[11] K. Tshoo, Y. K. Kim, Y. K. Kwon et al, Nucl. Instrum. Meth. B **317**, 242 (2013).

[12] Y. Blumenfeld, T. Nilsson and P. Van Duppen, Phys. Scr. T152 014023 (2013).

[13] A. Kelić, M. V. Ricciardi, K. -H. Schmidt, BgNS Transactions, **13**, 98 (2009).

[14] H. Alvarez-Pol et al., Phys. Rev. C **82**, 041602 (2010).

[15] O. B. Tarasov et al., Phys. Rev. C **80**, 034609 (2009).

[16] S. Lukyanov et al., Phys. Rev. C **80**, 014609 (2009).

[17] V. V. Volkov, Phys. Rep. **44**, 93 (1978).

[18] L. Corradi, G. Pollarolo, S. Szilner, J. Phys. G **36**, 113101 (2009).

[19] G. A. Souliotis et al., Phys. Lett. B **543**, 163 (2002).

[20] G. A. Souliotis et al., Phys. Rev. Lett. **91**, 022701 (2003).

[21] G. A. Souliotis et al., Nucl. Instrum. Methods **B 204** 166 (2003).

[22] G. A. Souliotis et al., Nucl. Instum. Methods **B 266**, 4692 (2008).

[23] G. A. Souliotis et al., Phys. Rev. C **84**, 064607 (2011).

[24] M. Papa et al., Phys. Rev. **C 64**, 024612 (2001).

[25] M. Papa et al, J. Comp. Phys. **208**, 403 (2005).

[26] J. Bondorf et al., Phys. Rep. **257**, 133 (1995).

[27] R. Charity et al., Nucl. Phys. **A 483**, 391 (1988); Phys. Rev. **C 58**, 1073 (1998).

[28] L. Tassan-Got and C. Stephan, Nucl. Phys. **A 524**, 121 (1991).

[29] M. Veselsky and G.A. Souliotis, Nucl. Phys. **A 765**, 252 (2006).

[30] P.N. Fountas, G.A. Souliotis, M. Veselsky and A. Bonasera, Phys. Rev. C 90, 064613 (2014).

Microscopic dynamical description of low and intermediate energy nuclear fission

N. Vonta and G.A. Souliotis*

Laboratory of Physical Chemistry, Department of Chemistry,
National and Kapodistrian University of Athens, Athens 15771, Greece
*soulioti@chem.uoa.gr

Abstract

The investigation of the mechanism of nuclear fission is a topic of current experimental and theoretical interest. In this work, we initiated a systematic study of low and intermediate energy fission calculations using the Constrained Molecular Dynamics (CoMD) code. The code implements an effective interaction with a soft isoscalar part and with several forms of the density dependence of the nucleon symmetry potential. In addition, CoMD imposes a constraint in the phase space occupation for each nucleon restoring the Pauli principle at each time step of the evolution of the nuclear system. Proper choice of the surface parameter of the effective interaction has been made to describe fission. In this work, we present CoMD calculations for several proton-incuded fission reactions at low and intermediate energy and compare them with recent experimental data. We found that the CoMD code is able to describe the complicated many-body dynamics of the fission process especially for intermediate and higher-energy fission reactions.

Introduction

The microscopic description of the mechanism of nuclear fission is a topic of intense nuclear research. Understanding of nuclear fission, apart from the theoretical many-body point of view, is of practical importance for energy generation, isotope production, as well as for the transmutation of nuclear waste. Furthermore, nuclear fission is essentially the process that defines the upper limit of the periodic table of the elements and plays a vital role in the production of heavy elements via the astrophysical r-process [1]. Motivated by the present state of affairs regarding fission research, we initiated a systematic study of low and intermediate energy fission using the Constrained Molecular Dynamics (CoMD) code of A. Bonasera and M. Papa [4,5].

Theoretical Framework

The Constrained Molecular Dynamics (CoMD) code is based on the gereral approach of molecular dynamics as applied to nuclear systems [2,3]. The nucleons are assumed to be localized gaussian wavepackets in coordinate and momentum space. A simplified effective nucleon-nucleon interaction is implemented with a nuclear-matter compressibility of K=200 (soft EOS) with

several forms of the density dependence of the nucleon-nucleon symmetry potential. In addition, a constraint is imposed in the phase space occupation for each nucleon, restoring the Pauli principle at each time step of the collision. Proper choice of the surface parameter of the effective interaction was made to describe fission.

In the calculations of the present work, the CoMD code was used essentially with its standard parameters. The soft density-dependent isoscalar potential was chosen (K=200). For the isovector part, several forms of the density dependence of the nucleon-nucleon symmetry potential are implemented. Two of them were used in the present work: the "standard" symmetry potential [red (solid) lines] and the "soft" symmetry potential [blue (dotted) lines] in the figures that follow. These forms correspond to a dependence of the symmetry potential on the 1 and the 1/2 power of the density, respectively. The surface term of the potential was set to zero to describe fission. For a given reaction, a total of approximately 5000 events were collected. For each event, the impact parameter of the collision was chosen in the range b = 0–6 fm, following a triangular distribution. Each event was followed up to 15000 fm/c and the phase space coordinates were registered every 50 fm/c. At each time step, fragments were recognized with the minimum spanning tree method ([4,5], and their properties were reported. Thus, information on the evolution of the fissioning system and the properties of the resulting fission fragments were obtained. In this way, the moment of scission of the deformed heavy nucleus could be determined. We allowed 2000 fm/c after scission for the nascent fission fragments to deexcite and we reported and analyzed their properties.

Results and Comparisons

Motivated by the present bibliography concerning the nuclear fission of uranium isotopes, we performed calculations related to the proton induced fission of ^{235}U, at 10 MeV, 30 MeV, 60 eV and 100 MeV. Moreover, calculations have been performed for the proton induced fission of ^{238}U, at 100 MeV and 660 MeV energies.

In Fig. 1, in the experimental data of the reaction p (27 MeV) + ^{232}Th, we observe the asymmetric nature of the fission of ^{232}Th. In contrast, the CoMD calculations result in a symmetric distribution with a flat top. The main reason is that the nucleon-nucleon interaction in the CoMD model does not include spin dependence, and thus the resulting mean field potential has no spin-orbit contribution. Consequently, the model cannot reproduce the correct shell effects necessary to describe the asymmetric low-energy fission of ^{232}Th.

When the proton energy increases (Fig. 2), it is expected that the shell effects will fade and the fissioning system will preferentially undergo symmetric fission. The mass yields for the same reaction at proton energy 63 MeV is pre-

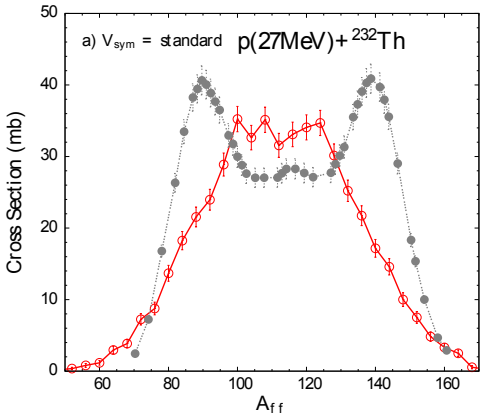

Fig. 1. (Color online) Normalized mass distributions (cross sections) of fission fragments from p (27 MeV) + ^{232}Th. Full points (grey): experimental data [6]. Open points: CoMD calculations with the standard symmetry potential.

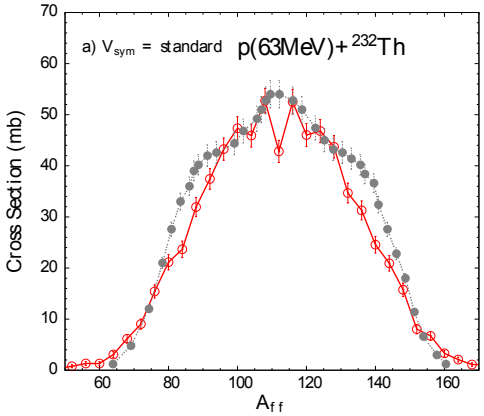

Fig. 2. (Color online) Normalized mass distributions (cross sections) of fission fragments from p (63 MeV) + ^{232}Th. Full points (grey): experimental data [6]. Open points: CoMD calculations with the standard symmetry potential.

sented. The experimental mass yield becomes more symmetric at this energy and the calculated yield curve is in better agreement with the data.

In Fig. 3, the mass distribution of proton induced fission of ^{238}U at 660 MeV is presented and it is in good agreement with the experimental data [8–10]. We observe, mostly the symmetric fission mode, due to the vanishing of the shell effects. Moreover, the calculations are able to describe satisfactorily the superasymmetric fission, which has been experimentallly seen at fission fragment masses ∼40–80 and ∼140–180.

In Fig. 4, we present the mass distribution for the neutron induced fission of ^{180}Hg at 10 MeV. The experimental data [11,12] are compared with the calculations. The work of [12] introduces a new type of asymmetric fission in proton-rich nuclei. It is related to the exotic process of β-delayed fission of ^{180}Tl. The experimental data represent the fission fragment mass distribution

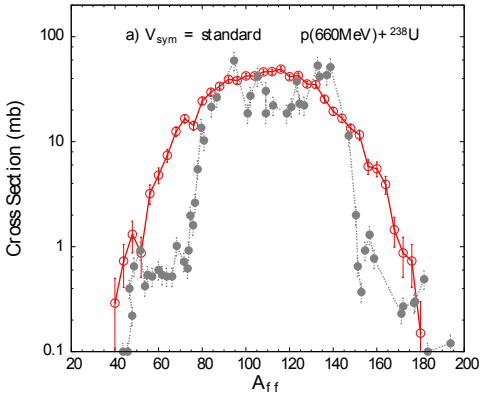

Fig. 3. (Color online) Normalized mass distributions (cross sections) of fission fragments from p (660 MeV) + ^{238}U. Full points (grey): experimental data [8–10]. Open points: CoMD calculations with the standard symmetry potential.

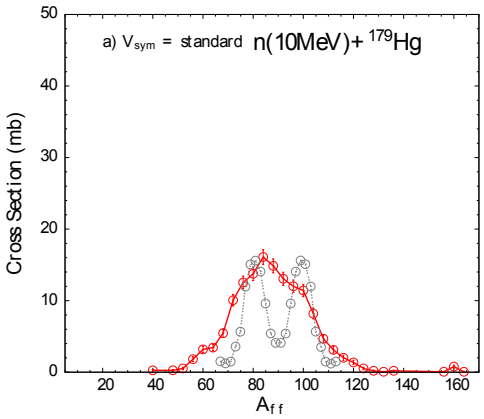

Fig. 4. (Color online) a) Normalized mass distributions (cross sections) of fission fragments from n (10 MeV) + ^{179}Hg. Full points (grey): experimental data [11,12]. Open points: CoMD calculations with the standard symmetry potential.

of the β-decay daughter nucleus ^{180}Hg, which is asymmetric. The asymmetric nature is surprising due to the fact that the nucleus ^{180}Tl is expected to be divided into two fragments of ^{90}Zr, with magic number of neutrons N=50 and semi-magic of protons Z=40, which are supposed to be more stable. The data of [11] are in arbitrary units and in order to be compared with the calculations, an appropriate scaling of the distribution has been made (multiplication factor 180). In the experimental data, the asymmetric nature of the fission is obvious. On the contrary, the CoMD calculations cannot describe correctly the shell effects and for this reason, the distribution is symmetric.

Apart from the fission fragment mass distributions, we investigated other fission fragment properties. The results are mostly with the standard symmetry potential. For the following figures, the red closed circles represent the proton induced fission of ^{235}U at 10 MeV, 30 MeV, 60 MeV, 100 MeV. Moreover, the red closed squares represent the proton induced fission of ^{238}U at 100 MeV 660 MeV, whilst the red closed triangles represent the proton induced fission

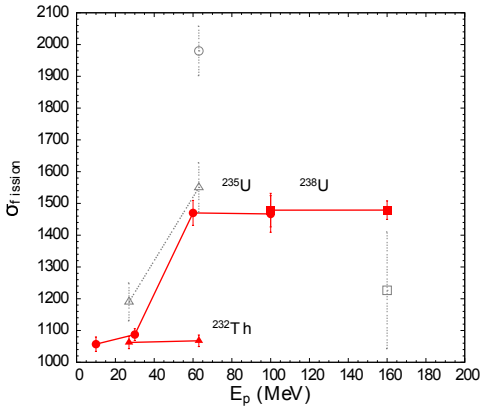

Fig. 5. (Color online) Calculated total fission cross section with respect to proton energy E_p. The CoMD calculations are carried out with the standard symmetry potential and are shown with full (red) symbols connected with full (red) lines. The reactions are indicated as follows: triangles: p (27, 63 MeV) + ^{232}Th, circles: p (10, 30, 60, 100 MeV) + ^{235}U, squares: p (100, 660 MeV) + ^{238}U. Some experimental data are shown with open symbols as follows: triangles: p (27, 63 MeV) + ^{232}Th [6], circles: p (60 MeV) + ^{235}U [7], square: p (660 MeV) + ^{238}U [9,10]. The point at E_p=660 MeV is displayed at E_p=160 MeV.

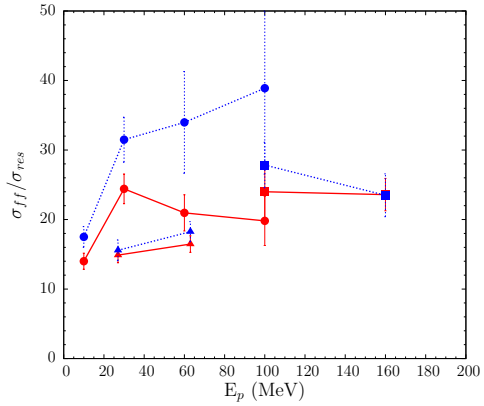

Fig. 6. (Color online) Calculated ratio of the fission cross section over residue cross section with respect to proton energy. CoMD calculations with the standard symmetry potential are with full (red) symbols connected with full (red) lines. Calculations with the soft symmetry potential are with full (blue) symbols connected with dotted (blue) lines. The reactions are indicated as follows: triangles: p (27, 63 MeV) + ^{232}Th, circles: p (10, 30, 60, 100 MeV) + ^{235}U, squares: p (100, 660 MeV) + ^{238}U. The points at E_p=660 MeV are displayed at E_p=160 MeV.

of ^{232}Th at 27 MeV 63 MeV. The blue points are with the soft symmetry potential. The experimental data are the open grey symbols (circles, squares and triangles) and they follow the same structure which has been adopted for the calculations.

The total fission cross section is presented in Fig. 5 in reference to the various proton energies for the proton induced fission of ^{232}Th, ^{235}U and ^{238}U.

Concerning the fission of thorium, we observe that increasing the excitation energy there is only a slight increase. However, the experimental data show a jump of approximately 30%.

In Fig. 6, we present the correlation between the excitation energy and the ratio of the fission cross section over the residue cross section. For the fission of ^{232}Th we observe an increase in this ratio towards higher excitation energy. Hence, at 63 MeV beam energy, our calculations show higher probability for fission, in reference to the energy 27 MeV. Moreover, for the fission of the ^{235}U and ^{238}U, the probability of getting fission decreases at excitation energies, starting from 30 MeV to 100 MeV and from 100 MeV to 660 MeV respectively. Furthermore, a sensitivity of the calculations concerning the symmetry potential choice is depicted. For the soft potential choice, the aforementioned ratio increases and this means that this choice leads to an increasing probability of getting fission, especially for the proton induced fission of ^{235}U at various proton energies.

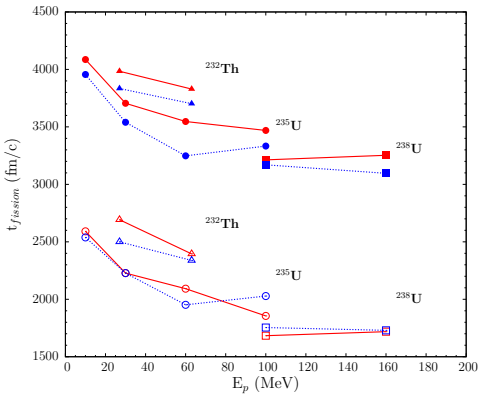

Fig. 7. (Color online) Calculated fission time with respect to incident proton energy. CoMD calculations with the standard symmetry potential are with (red) symbols connected with full (red) lilnes. Calculations with the soft symmetry potential are with (blue) symbols connected with dotted (blue) lines. The full symbols (upper half of the figure) are with the full ensemble of the fissioning nuclei, whereas the open symbols (lower half) are with the selection of the fissioning system not to emit any pre-scission protons (see text). The reactions are indicated as follows: triangles: p (27, 63 MeV) + ^{232}Th, circles: p (10, 30, 60, 100 MeV) + ^{235}U, squares: p (100, 660 MeV) + ^{238}U. The points at E_p=660 MeV are displayed at E_p=160 MeV.

It is very difficult to estimate the fission time from experimental data. Because of the fact that the CoMD is a dynamical microscopic code, we can naturally obtain the dynamical path of the process and therefore determine the fission time. In Fig. 7, the fission time is plotted versus the proton energy of the indicated reactions. We performed the calculations under the restrictions that the fissioning system be a) Z=91, for ^{232}Th b) Z=93, for ^{235}U and ^{238}U, which are represented by the open circles, squares and triangles (open symbols). Moreover, the closed symbols refer to the CoMD calculations where the full ensemble of the fissioning nuclei is taken into account. For this ensemble, we

noticed that the code emits on average two pre-scission protons. The general trend shows that the fission time decreases with the increase of the excitation energy. We observe that the open symbols are lower than the closed ones. The general trend shows that the fission time decreases when the proton energy increases. Additionally, the choice of Z for the fissioning system leads to a decrease of the fission time. When this choice is made, the total Coulomb energy is larger (since no pre-scission protons are emitted) and thus, the fissioning system is more fissionable.

Discussion and Conclusions

In the present work we employed the semi-classical microscopic code CoMD to describe mostly proton induced fission, in a variety of energies on ^{232}Th, ^{235}U and ^{238}U nuclei. We chose these nuclei because of the availability of recent literature data and because of their significance in current applications of fission. We found that the CoMD code in its present implementation is able to describe fission at higher energies where the shell effects are washed out. We mention that the effective nucleon-nucleon interaction employed in the code has no spin dependence and thus the resulting mean field has no spin-orbit contribution. We are exploring possibilities of adding such a dependence on the potential to give us the ability to adequately describe the characteristics of low energy fission.

We note that the total fission cross sections were rather well reproduced and the ratio of total fission cross sections over residue cross sections appears satisfactory. Interestingly, this ratio shows a sensitivity on the choice of the symmetry potential. Concerning the mean total energies and the neutron multiplicities, we mention that they are rather adequately reproduced [13]. Finally, information on the fission time scale is obtained from the present calculations. The obtained fission times show a dependence on the excitation energy of the fissioning nucleus, as well as on the choice of the symmetry potential.

In closing, we point out that the CoMD code gives results that are not dependent on the specific dynamics being explored and, thus, offers valuable predictive power for the different modes of fission without adjustable parameters. Consequently, the code can be used for the study of fission of either very neutron-rich or very neutron-deficient nuclei, which have not been studied experimentally to date. Furthermore, this possibility can be exploited to study the fission of very exotic nuclei related to the end point of the r-process, namely the process of fission recycling.

Acknowledgements

We wish to thank M. Veselsky and A. Bonasera for their continued contribution to the present project. We are thankful to M. Papa for his version of the CoMD code, and to Hua Zheng for his rewritten version of the CoMD. We

are also thankful to W. Loveland for his enlighting comments and suggestions on this work. Furthermore, we wish to acknowledge the motivation and recent discussions on experimental aspects of fission with Y.K. Kwon and K. Tshoo of the KOBRA team of RISP (Korea).

References

[1] J. Erler et al, Nature **486**, 509 (2011).

[2] A. Bonasera, F. Gulminelli, J. Molitoris, Phys. Rep. **243**, 1 (1994).

[3] J. Aichelin, Phys. Rep. **202**, 233 (1991).

[4] M. Papa et al., Phys. Rev. **C 64**, 024612 (2001).

[5] M. Papa et al, J. Comp. Phys. **208**, 403 (2005).

[6] P. Demetriou et al., Phys. Rev. **C 82**, 054606 (2010).

[7] M. C. Duijvestijn et al., Phys. Rev. **C 64**, 014607 (2001).

[8] A. Deppman et al., Phys. Rev. **C 88**, 064609 (2013).

[9] G.S. Karapetyan et al., Phys. Atom. Nucl. **C 72**, 911 (2009).

[10] A.R. Balabekyan et al., Phys. Atom. Nucl. **C 73**, 1814 (2010).

[11] A.V. Andreev et al., Phys. Rev. **C 88**, 047604 (2013).

[12] A.N. Andreyev et al., Phys. Rev. Lett. **105**, 252502 (2010)

[13] N. Vonta, G.A. Souliotis, M. Veselsky, A. Bonasera, Phys. Rev. C submitted (2015).

Neutron Spectroscopy with the Spherical Proportional Counter

E. Bougamont[1], A. Dastgheibi[1], J. Derre[1], G. Gerbier[1], I. Giomataris[1], M. Gros[1], I. Katsioulas[2], P. Magnier[1], X.F. Navick[1], T. Papaevangelou[1], I. Savvidis[2], G. Tsiledakis[1].

1. *IRFU, CEA Saclay, Gif s Yvette, France*
2. *Aristotle University of Thessaloniki, Greece*

Abstract. A novel large volume spherical proportional counter has been developed, for neutron measurements. Gas mixtures of N_2 with CH_4 and pure N_2 have been studied for thermal and fast neutron detection, providing a new way for the neutron spectroscopy. The neutrons are detected via the $^{14}N(n,p)^{14}C$ and $^{14}N(n,\alpha)B^{11}$ reactions. The α resolution of the detector has been measured using ^{222}Rn gas, in order to have the response of the total active volume of the detector. The three α peaks from ^{222}Rn decay and ^{222}Rn daughters decay have been measured with FWHM less then 2%, with gas mixture Ar 98% and CH_4 2% at a pressure of 200 mbar.

1. Introduction

The Spherical Proportional Counter is a novel concept with very promising features, among which is the possibility of easily instrumenting large target masses with good energy resolution and low energy threshold. The natural radial focusing of the spherical geometry allows collecting and amplifying the deposited charges by a simple and robust detector using a single electronic channel to read out a large gaseous volume [1,2,3]. The sensitivity of the detector obtained with the use of the Rn and Rn daughters decay for the alpha particles in energy range 5.3 MeV- 7.7MeV. The low energy calibration of the detector from 100eV up to several tenths of keV achieved with the use x-rays and UV lamp [4,5]. At the present work the spherical detector has been optimized for operation in pure N_2.

2. The detector

The detector consists of a copper sphere, 1.3 m in diameter and 6mm thick (figure 1). The spherical vessel is well pumped (up to 10^{-8} mbar) and then is filled with a gas mixture at a pressure from several hundreds of mbars up to 5 bars. Out gassing in the order of 10^{-9} mbars/s is necessary for the amplification stability, because the present of the O_2 in the drift volume changes the detector characteristics.

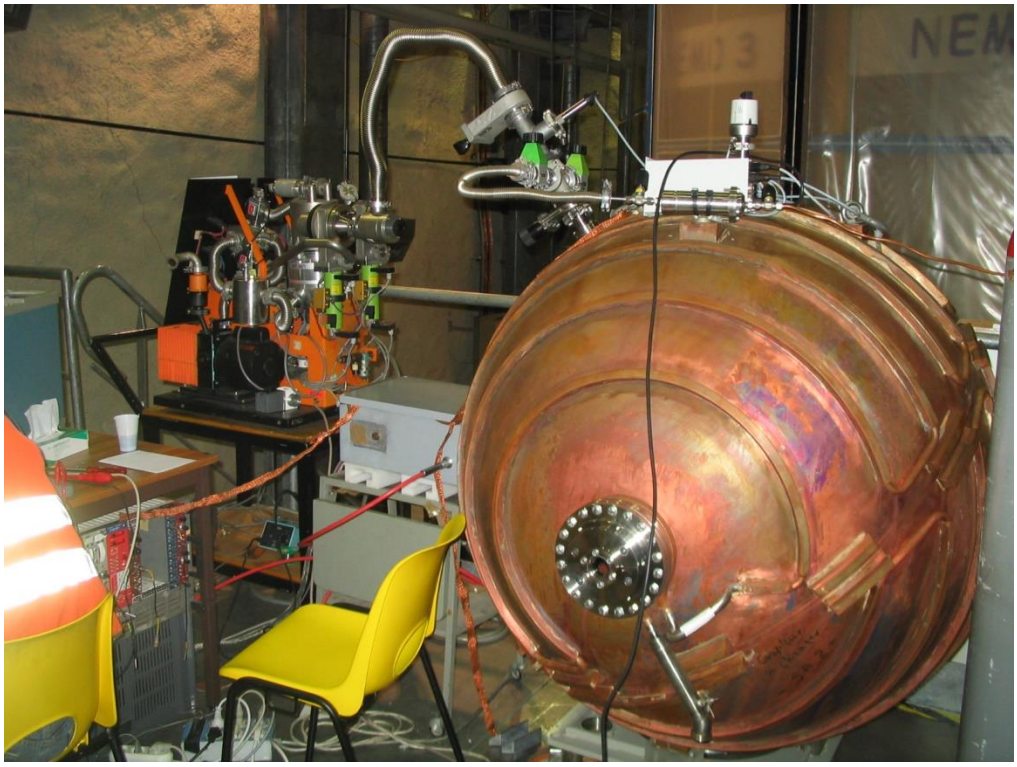

Figure 1. A photograph of the spherical vessel

A small stainless ball of 14 centimeters in diameter fixed in the center of the spherical vessel by a stainless steel rod, acts as an electrode with positive high voltage and as a proportional amplification counter. The detector was operated with positive bias applied to the anode (inner sphere) while the cathode (external sphere) remained at ground potential. A high voltage capacitor was decoupling the high voltage cable to protect the sensitive preamplifier.

Energetic charged particles, x-rays, or gamma rays or even neutrons entering the detector strip electrons from the gas atoms to produce positively charged ions and negatively charged electrons (figure 2). The electric field created across the electrodes drifts the electrons to the positive electrode. Near the inner anode sphere the electric field is high enough and electrons gain enough energy to ionize more gas atoms, a process that produces more electrons. Typical gases at atmospheric pressure required field strength on the order 10kV/cm to produce the avalanche of secondary electrons around the small anode ball. The avalanche is produced at a few mms distance from the anode and the positive ions drift towards the cathode . Since the avalanche takes place near the small ball and the electrons are attracted to it and the positive ions travel a much greater distance. Therefore the induced pulse to the preamplifier is mainly due the ion movement; electrons produced during avalanche process have a negligible contribution to the signal.

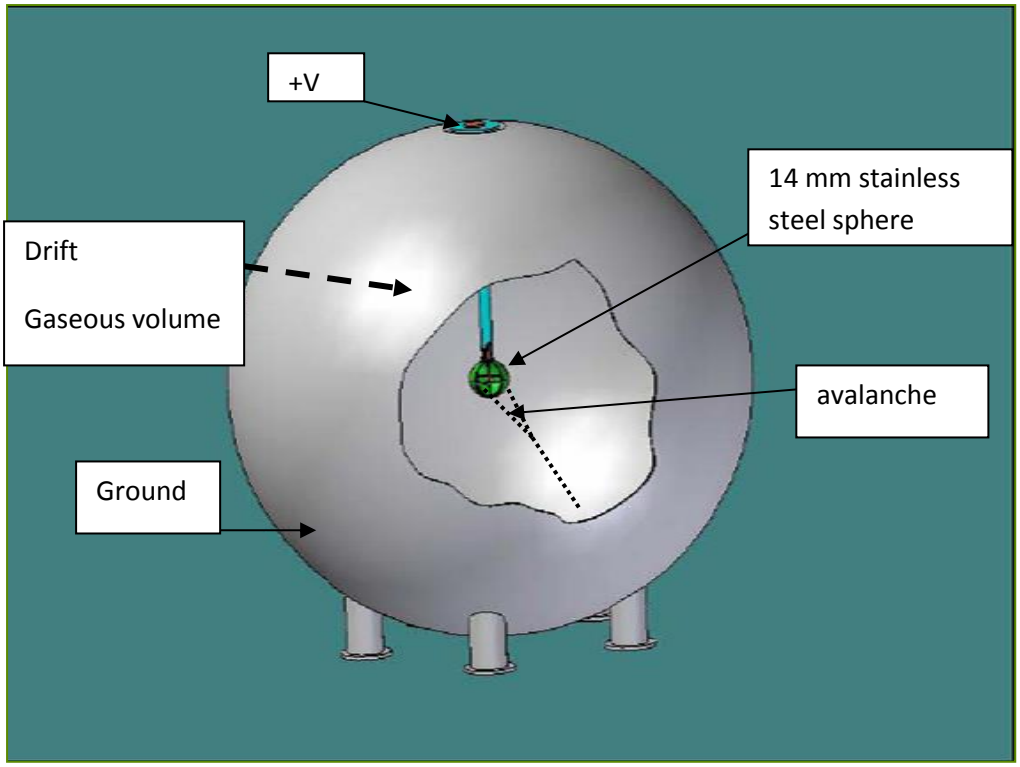

Figure 2. Sketch of the detector, showing the inner electrode and the avalanche formation from an electron, few mm far from the small ball. Positive ions moving backward are inducing a signal to the preamplifier.

3. The electric field

The electric field in the drift volume plays a very important role for the proportionality and the energy resolution of the detector. The ideal detector is a spherical capacitor with a perfect radially symmetric electric field. In a real implementation of the spherical TPC concept, the ideal spherical symmetry is broken by the rod that supports the central electrode and that necessarily connects it to the front-end electronics, placed outside, to amplify and read the signals. In figure 3 the equipotential lines are plot for this simplest geometry, showing how the presence of this rod affects the symmetry of the electric field. The concequence of this symmetry breaking is that the amplification depends on the direction and position of the interacting particle in the drift volume.

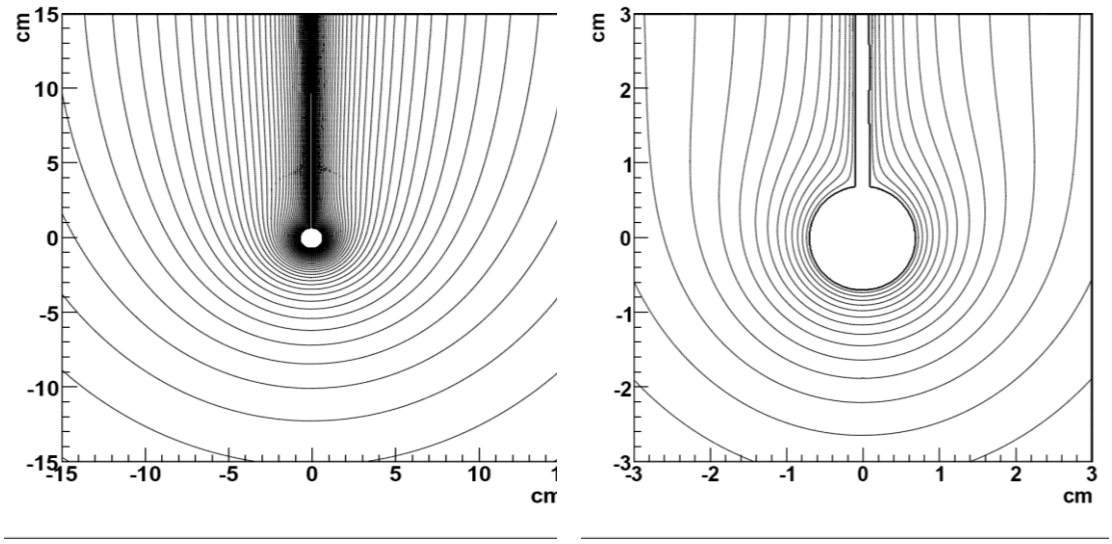

Figure 3. The equipotential lines around the 14 mm sphere without any correction.

To solve the problem of field distortion due to anode electrode, a cylinder was placed around the high voltage rod, 4 mm away from the spherical electrode and powered with an independent voltage V_2 (which can be zero, i.e., at ground potential). The equipotential lines for the described "corrected" configuration are shown in figure 4.

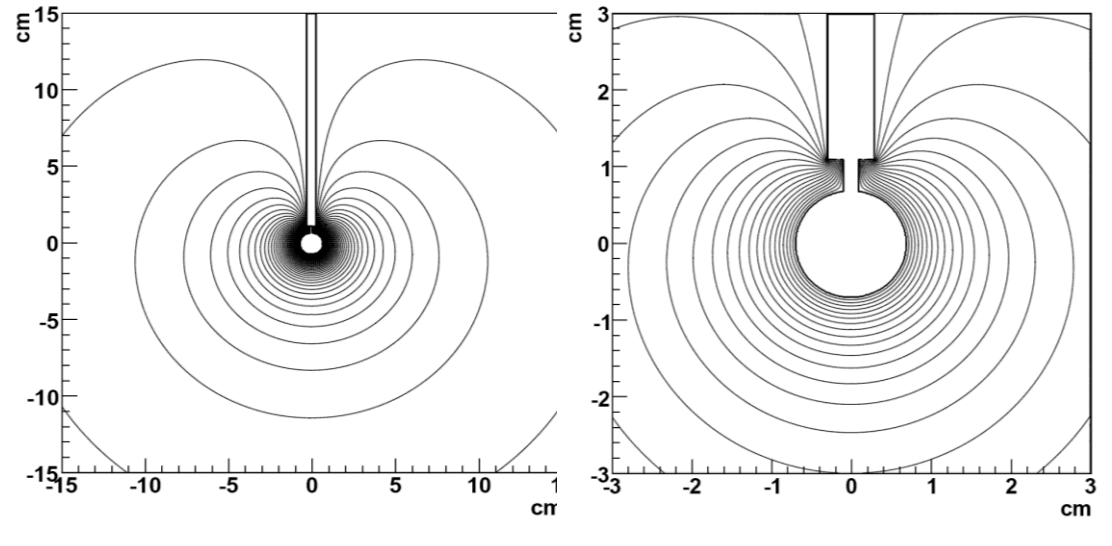

Figure 4. Electrostatic configuration for the readout electrode, with the "corrector" electrode consisting of a grounded cylinder surrounding the high voltage rod and placed 4 mm away from the spherical electrode.
Sphere diameter =14mm.

5. The energy resolution

The energy resolution of the detector has been tested using ^{222}Rn gas and detecting the alpha particles from ^{222}Rn and ^{222}Rn daughters. Since the ^{222}Rn gas cover homogenously all the drift volume of the detector, we have alpha emission in every direction and in all the positions of the detector. So, charges from the alpha tracks arrive at the central positive electrode from every point and the amplification can be caused everyware on the surface of the 14 mm sphere.

The gas mixture consist of Ar (98%) and CH4 (2%) at pressures, from 150 mbars up to 1 bar. The high voltage varies from 1.5 kV up to 5 kV depending on the gas pressure.

A charge preamplifier is connected to the central electrode and the signal is proportional to the charge particle energy.

In the figure 5 is shown the peaks observed from a ^{222}Rn radioactive source. From left to right we observe the ^{222}Rn peak at 5.5 MeV, the ^{218}Po and ^{214}Po at 6.0 MeV and 7.7 MeV respectively. The energy resolution was 2% FWHM at 200 mbar gas pressure and 2.8 kV High Voltage.

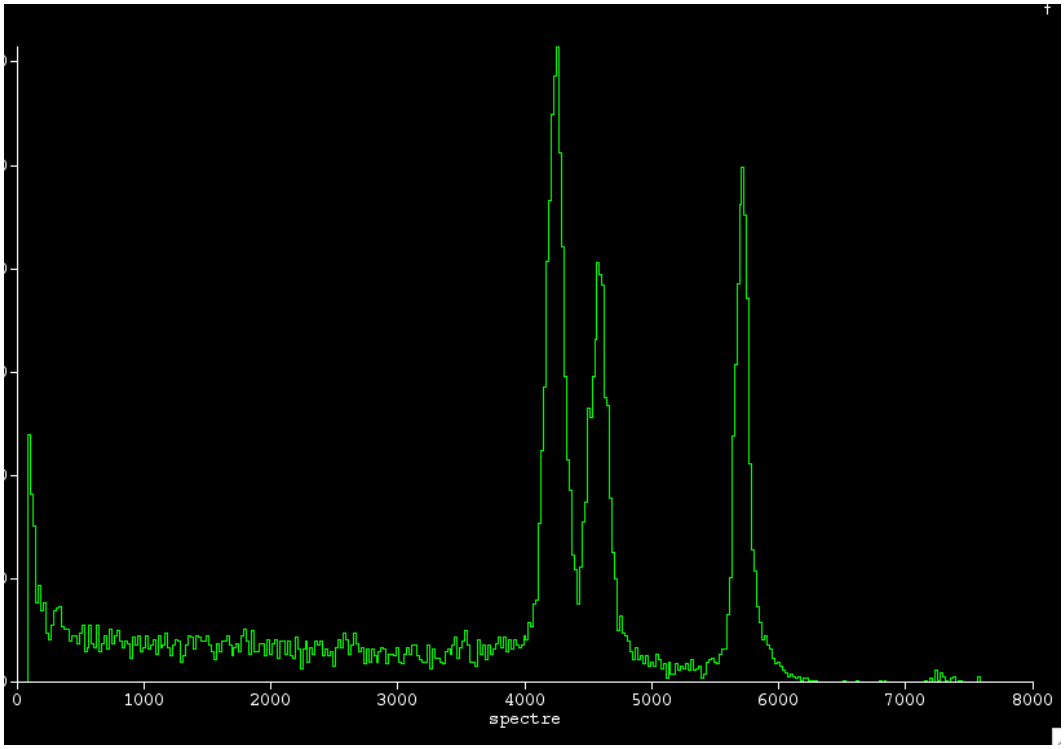

Figure 5. The peaks observed from a ^{222}Rn radioactive source. From left to right we observe the ^{222}Rn peak at 5.5 MeV, the ^{218}Po and ^{214}Po at 6.5 MeV and 7.7 MeV respectively. The energy resolution was 2% FWHM at 200 mbar gas pressure and 2.8 kV High Voltage.

6. The neutron detection

The detector is filled with gas mixtures of (N_2, CH_4) or with pure N_2 at pressures up to 500mbar, were the neutrons interact with the ^{14}N nucleus via the reaction

$$^{14}N + n \rightarrow {}^{14}C + p + 625.87\ keV$$

The Q energy of the reaction is shared between ^{14}C and p with E_C=41,72 keV and E_p=584.15keV in the case of the thermal neutrons. The cross section for the thermal neutrons is 1.83barns and for the fast neutrons is shown in figure 6. Because of the energy and the long range of the protons in the gas mixture, they play the main role for the signal characteristics such as the rise time and the width. Fast neutrons with energies higher than 1.7 MeV can be well detecting also via the $^{14}N(n,\alpha)B^{11}$ reaction up to E_n=20MeV.

$$^{14}N + n \rightarrow {}^{11}B + \alpha \qquad Q=-158\ keV$$

This reaction plays a dominating role in the fast neutron detection for E_n>2MeV, since the cross section of the $^{14}N(n,\alpha)B^{11}$ reaction is higher than that of the $^{14}N(n,p)C^{14}$ reaction.

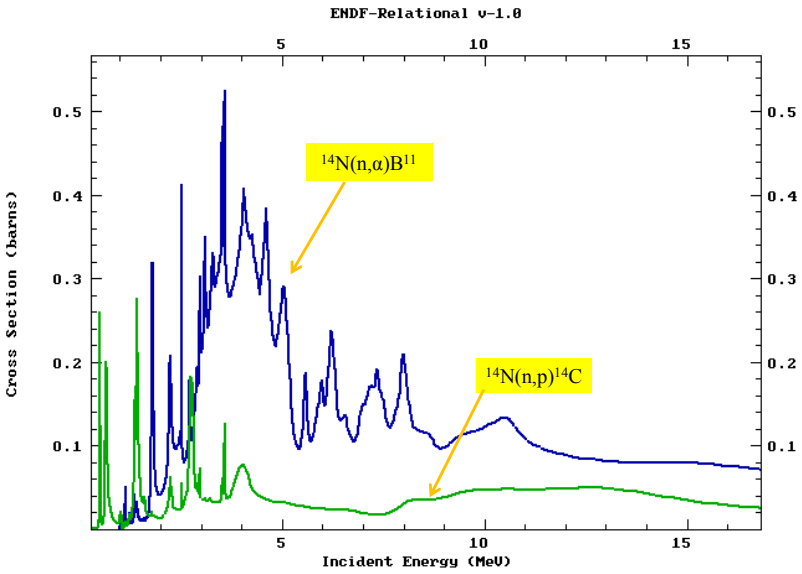

Figure 6. *The cross sections of the reactions $^{14}N(n,p)^{14}C$ and $^{14}N(n,\alpha)B^{11}$ up to 20 MeV neutrons*

7. Fast neutrons from Am-Be neutron sources

Long time measurements with ^{214}Am-Be neutron sources have been done, to study the fast neutron detection

In the figure 7 (left) are presented the experimental data after irradiation with ^{241}Am-Be neutron source using the 8mm metallic ball and a gas mixture of 140 mbars N_2 + 9 mbars Ar + 1 mbar CH_4. Since the neutrons ^{241}Am-Be source (figure 7, right) have higher energies compared to that of the ^{252}Cf source, the most of the events are coming from the (n,α) reactions. In the figure we can see the accumulation of the signals at lower energies because of the wall effect and the moderated neutrons in the surrounding materials.

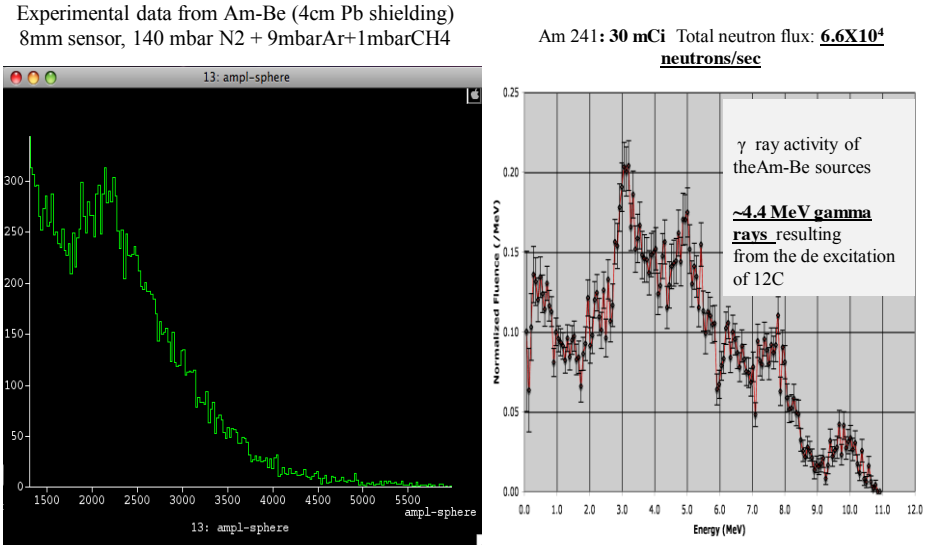

Figure 7. *Experimental data after irradiation with Am-Be neutron source. There is movement of the spectrum to the left coming from the moderated neutrons.*

In order to measure the neutron energy, both the produced charged particles from the (n,p) and (n,α) reactions must deposit all their energy in the drift volume. If the reaction takes place close to the vessel wall, it is possible one of the charged particles or both of them to hit the wall and to lose a part of their energy. This leads to wrong estimation of the neutron energy.

In the case that we use the detector as neutron spectrometer and not as a simple neutron counter, the wall effect plays an important role. The wall effect depends on the ranges of the produced particles in the drift volume and on the size of the detector.

7. Conclusions

The spherical proportional counter can be used successfully as a neutron detector via the $^{14}N(n,p)^{14}C$ and $^{14}N(n,\alpha)B^{11}$ reactions. Both gasses N_2 with CH_4 and the pure N_2 are working well. The large volume with the possibility to operate at high gas pressure is an important advantage of our detector compared to the typical cylindrical proportional counters.

8. References

[1] Giomataris I and Vergados J D 2004 *Nucl.Instrum.Meth.A* **530** 330-58
[2] Giomataris I et al 2006 *Nucl.Phys.Proc.Suppl.* **150** 208-13
[3] Aune S et al. 2005 *AIP Conf.Proc.* **785** 110-8
[4] I. Giomataris et al, 2008 JINST 3 P09007
[5] S.Andriamonje et al., Journal of Physics: Conference Series 179 (2009) 012003 doi:10.1088/1742-6596/179/1/012003

Optical potential for ^{7}Be+^{28}Si at near barrier energies

O. Sgouros[1], A.Pakou[1,*], D. Pierroutsakou[2], M. Mazzocco[3], L. Acosta[4], X. Aslanoglou[1], A. Boiano[2], C. Boiano[5], J. Grebosz[6], N. Keeley[7], M. La Commara[2,8], G. Marquinez-Duran[4], I. Martel[4], C. Parascandolo[3], K. Rusek[9], A. M. Sanchez-Benitez[10], C. Signorini[3], V. Soukeras[1], E. Stiliaris[11], E. Strano[3], I. Strojek[7], D. Torresi[3].

[1] *Department of Physics and HINP, The University of Ioannina, 45110 Ioannina, Greece*
[2] *INFN Sezione di Napoli, via Cinthia, I-80126, Napoli, Italy*
[3] *Departimento di Fisica and INFN - Sezione di Padova, via Marzolo 8, I-35131, Padova, Italy*
[4] *Departamento di Fisica Aplicada, Universidad de Huelva, E-21071, Huelva, Spain*
[5] *INFN Sezione di Milano, via Celoria 16, I-20133 Milano, Italy*
[6] *IFJ-PAN, Krakow, Poland*
[7] *National Center for Nuclear Research, A. Soltana 7, 05-400, Otwock Warsaw, Poland*
[8] *Dipartimento di Scienze Fisiche, Universita di Napoli, via Cinthia, I-80126, Napoli, Italy*
[9] *Heavy Ion Laboratory, University of Warsaw, Pasteura 5a, 02-093, Warsaw, Poland*
[10] *Centro de Fsica Nuclear da Universidade de Lisboa, 1649-003 Lisboa, Portugal*
[11] *Institute of Accelerating Systems and Applications and Department of Physics, University of Athens, Greece*

Abstract

The elastic scattering of ^{7}Be+^{28}Si was studied at several near barrier energies for probing the energy dependence of the optical potential. Our preliminary analysis at 17.2 MeV will be presented in this article and discussed, in terms of Continuum Coupled Channel Calculations (CDCC). This research is part of a long term plan concerning the energy dependence of the optical potential for weakly bound projectiles, at near barrier energies and for probing the potential threshold anomaly. The experiment took place at the EXOTIC facility - Laboratori Nationali di Legnaro (LNL), and refers to an angular distribution

*e-mail:apakou@cc.uoi.gr

measurement, using the detector array EXPADES (Exotic Particle Detection System). Results at 9 MeV (Rutherford region) were also anlysed and were used for estimating the solid angle. Our analysis for other energies is under process

Keywords: `weakly bound projectiles`, `optical potential`, `elastic scattering`, `threshold anomaly`

1. Introduction

The last decade, the energy dependence of the optical potential for weakly bound systems, at near and sub-barrier energies has attracted a strong interest. Standard theories deduced from tightly bound projectiles, referring to the potential threshold anomaly (TA) and the validity of the dispersion relation, have been studied and debated. It is well known that the optical potential for well bound systems presents a smooth energy dependence for both the real and imaginary part at the higher energies, while as the energy decreases and approaches the coulomb barrier the imaginary part sharply decreases and the real part presents a localized peak. This peak is connected with polarization potentials of different signs describing the various reaction channels and it is related with the imaginary part of the optical potential via dispersion relations.

In a long term plan in this and other laboratories, it has been shown that for weakly bound projectiles as ^{6}Li and ^{7}Li the conventional TA is not any more applicable [1, 2]. It was also observed that the energy dependence of the potential for the two projectiles is not similar. While for ^{6}Li the imaginary part of the optical potential presents an increasing trend as the energy decreases at the barrier and below it, and the real part develops smoothly, for ^{7}Li the smooth energy dependence is valid for both real and imaginary terms till very low sub-barrier energies. For both projectiles the sudden drop of the imaginary part appears at very low sub-barrier energies where the development of a localized peak for the real part is mostly improbable. Else, the dispersion relation does not hold and the energy dependence of the real part can progress smoothly till

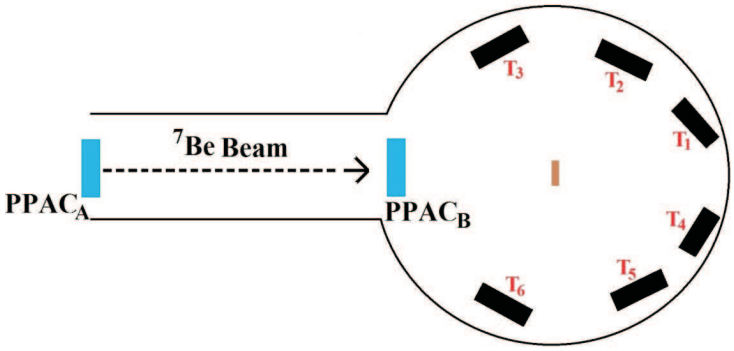

Figure 1: Schematic detector set up of the proposed measurement. Telescopes T1 and T4 are set at 27±15 deg, telescopes T2, T5 at 67±15 deg and telescopes T3,T6 at 110 ±15 deg, the last mainly for detecting the alpha production.

the lowest energy [3]. As the study of the energy dependence of the potential is strongly related with breakup and transfer processes, coupled to the elastic scattering and fusion, such studies are appealing for weakly bound drip line nuclei, where such reaction mechanisms are reinforced.

2. The experiment

^{7}Be is a proton rich weakly bound radioactive nucleus, mirror to the weakly bound but stable ^{7}Li nucleus. The breakup threshold for beryllium is 1.6 MeV, which is lower than the corresponding 2.45 MeV for ^{7}Li, but similar to 1.48 MeV for ^{6}Li. As the energy dependence of the optical potential and relevant reaction mechanisms for both lithium projectiles on a silicum target were comprehensively studied in the past, it will be interesting to fill up the systematics and make the appropriate comparisons with ^{7}Be. In principle scarce elastic scattering measurements exist in the literature with aluminum and carbon targets [7, 8]. Recently more detailed measurements were presented on nickel [10, 11] and aluminum [9]. However such measurements lack the sensitivity on the energy dependence of the potential due to the large assigned error bars or/and inappropriate technical details of the measurement as the large target thickness

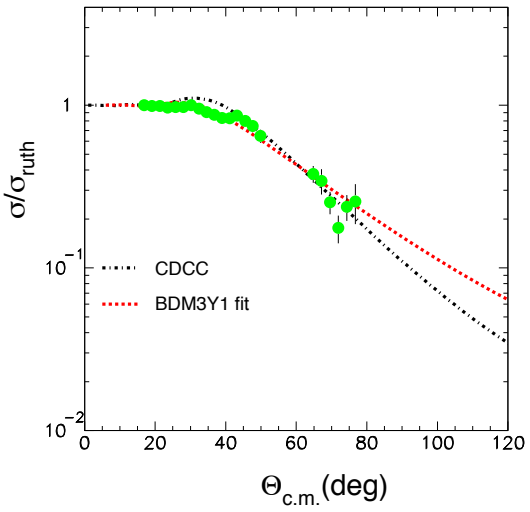

Figure 2: Elastic scattering data obtained at 17.2MeV are compared with a CDCC calculation.

in the last measurement. As the authors accept, their results are susceptible to the target thickness. It should be noted that in this work the adopted target thicknesses were from 2.1 to 5 mg/cm^2, which resulted to a beam energy difference from the beginning to the end of the target by 20 to 40%. More accurate data at various targets are necessary to describe th optical potential at near barrier energies. Moreover for a deep understanding of the threshold phenomenon, the involved reaction mechanisms have to be addressed and quantified. So far such studies are not available for ^{7}Be apart of a fusion measurement with a heavy projectile [12]. In this respect we have presented in this symposium, preliminary results of precise elastic scattering measurement at 17.2 MeV. The analysis of results at several other energies will be presented in the near future.

The ^{7}Be secondary beam was delivered from the EXOTIC facility [5] by means of the In Flight (IF) technique. A primary $^7Li^{3+}$ beam at$\sim$ 30MeV was produced by the LNL-XTU Tandem accelerator and impinged on the EXOTIC gas target, which consists of a 5-cm long gas cell doubly walled with 2.2 μm

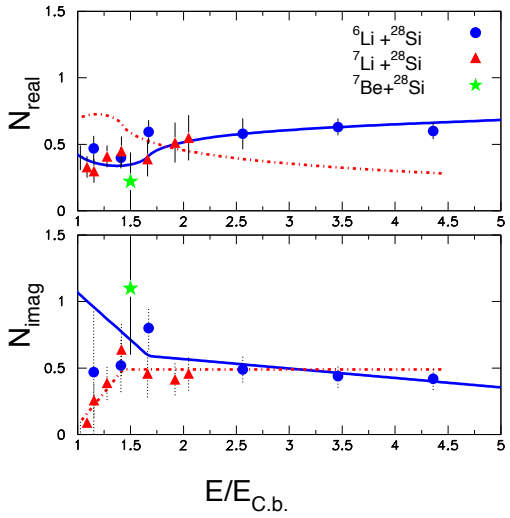

Figure 3: Previous data [1, 2]on the optical potential energy dependence for ^{6}Li and ^{7}Li on silicon are compared with the present datum for ^{7}Be+^{28}Si

thick Havar foils. The cell was filled with H_2 gas up to a pressure of about 1000 mbar at room temperature (300 K), which corresponds to an H target density of 0.4 mg/cm^2. The ^{7}Be secondary beam was separated from the contaminant ^{7}Li scattered beam and from ^{4}He nuclei produced via the reaction p(^{7}Li,^{4}He)^{4}He (Qval = +17.35 MeV) by means of a 30^0 bending magnet, a Wien Filter and adequate slit sets and collimation systems located at suitable positions along the beam-line. In this respect a secondary beam at 17.2 MeV was produced at a rate of $\sim$4x10^{4}pps. The energy at 9 MeV, used for the solid angle determination, was produced with an aluminum degrader. A secondary silicon target of thickness 0.4 mg/cm^2 was set in the middle of the chamber for the main measurement.

Downwards across the beam line and 88 cm before the secondary target a parallel plate avalanche counter (PPAC$_A$) and at 35 cm a second PPAC$_B$ was used as to improve and monitor the beam spatial profile before and during the measurement.

Moreover our experimental setup included the detector array EXPADES (EXotic PArticle Detection System) [6]. A schematic setup is shown in Figure 1 and includes 6 telescopes in symmetrical positions for increasing the statistics and rule out any beam diversion. For the energy presented here, the elastic scattered ejectiles were detected in the first stage of the telescope, where they stop. For the higher energies and the alpha production, particles were discriminated by a ΔE-E technique. The thickness of the ΔE DSSD silicon detectors is $\sim$55 μm while the DSSD E stage has thickness 300 μm. Both modules have active areas of 64 x 64 mm^2 with 32 strips per side, orthogonally oriented to define 2 x 2 mm^2 pixels. The telescopes were fixed at a distance of $\sim$11 cm far from the target position covering a total solid angle of 1.8sr. The electronics of the ΔE stage are such as to collect events every two strips, therefore the angular resolution is 2 degrees per angular position for setting the detectors at 11 cm distance from the target.

The detector signals are read by using standard electronic chains (recently developed and tested at Milano and Napoli) for the ionization chambers and the pads, while 32-channel ASIC chips manufactured by IDEAS-GM (Norway), (VA32HDR14.2 and TA32CG.3) are employed for the E_{res} stages. The chip VA is dedicated to the treatment of the linear part of the electronic signals coming from the detector strips, while the chip TA generates a logical trigger signal. The output signal of each chip VA is a serial stream of 32 analogue current signals containing the information of the charge collected by each detector strip and, ultimately, of the energy lost by an incident particle into the strip. The analysis of these signal streams is performed by means of a sampling ADC, especially developed by the EXOTIC collaboration. The output data are processed by a new acquisition system designed at LNL by the EXOTIC collaboration. The valuable advantage of this readout system, based on micro electronic devices, is that only one signal contains the energy loss information for all the strips of each detector side (namely 32 channels) and therefore a strongly reduced number of electronic chains is required for the readout of the entire apparatus.

3. Results and Discussion

In Fig. 2 we present our experimental results in comparison with CDCC calculations. The differential cross sections were obtained adopting the following relation

$$\sigma(\theta) = \frac{N(\theta)\sigma_9\Phi_9}{N_9(\theta)\Phi}, \tag{1}$$

where σ (θ) is the differential cross section at 17.2MeV, N(θ) is the elastic scattering counting rate for the 17.2MeV energy at θ, σ_9 is the differential cross section calculated via Rutherford scattering at 9MeV, Φ_9 is the beam flux during the run at an energy of 9MeV, $N_9(\theta)$ is the counting rate for the 9 MeV run at the same angle and Φ is the beam flux during the 17.2MeV run. the differential cross section of relation 1 was divided by the Rutherford scattering at the energy of 17.2 MeV and the ratio of Φ_9/Φ was adjusted such as at the most forward angles the ratio of cross sections to be 1. In that way the error assigned to our data is connected solely with the statistical error and other systematic uncertainties, but not errors due to flux, target thickness and solid angle. In the same figure we present CDCC calculations which are found in very good agreement with the experimental results. Also optical model calculations were performed taking into account a BDM3Y1 interaction for both the real and imaginary part and fitting to the data the normalization factors N_{real} and N_{imag}. These normalization factors are presented with the star in Figure 3, where previous data [1, 2] describe the energy dependence of ^{6}Li and ^{7}Li on a silicon target. Although in the present study we have only one datum, it is obvious that the trend of the optical potential for ^{7}Be+^{28}Si follows the one for ^{6}Li and not for ^{7}Li. However, more data at other energies are necessary to confirm this conclusions. The analysis of such data is under process.

Acknowledgments: The research leading to these results has received funding from the European Union Seventh Framework Programme FP7/2007-2013 under Grant Agreement No. 262010-ENSAR.

References

[1] A. Pakou et al. , Phys. Lett. **B 556**, 21(2003).

[2] A. Pakou et al. Phys. Rev. C **69**, 057602(2004).

[3] K. Zerva et al, Eur. Phys. Journal **48**, 102 (2012).

[4] A. Pakou et al., Phys. Rev. C 76, 054601 (2007).

[5] F. Farinon et al, Nucl. Instrum. Meth. **B 266**, 4097 (2008).

[6] E. Strano et al., Nucl. Instrum. Meth. Phys. Res. **B 317**, 657 (2013).

[7] K. Kalita et al., Phys. Rev. **C 73**, 024609(2006).

[8] J. C. Zamora et al., Phys. Rev. **C 84**, 034611(2009).

[9] V. Morcelle et al., Phys. Rev. C 89, 044611(2014).

[10] E. F. Anguilera et al., Phys. Rev. **C 79**, 021601(2009).

[11] A. Gomez Camacho et al., Nucl. Phys. **A 833**, 156 (2010).

[12] R. Raabe et al., Phys. Rev. **C 74**, 044606 (2006).

The LIPMAGNEX experiment: Study of ^{6}Li + p in inverse kinematics

V. Soukeras[1], A. Pakou[1,*], F. Cappuzzello[2,3], L. Acosta[4], C. Agodi[2], N. Alamanos[5], M. Bondi[2,3], D. Carbone[2], M. Cavallaro[2], A. Cunsolo[2], M. De Napoli[6], A. Di Pietro[2], J. P. Fernández-García[2], P. Figuera[2], M. Fisichella[2], A. Foti[3,6], N. Keeley[7], G. Marquinez-Duran[4], I. Martel[4], M. Mazzocco[8], D. Nicolosi[2,3], D. Pierroutsakou[9], K. Rusek[10], O. Sgouros[1], E. Stiliaris[11], E. Strano[8], D. Torresi[8].

[1] *Department of Physics and HINP, The University of Ioannina, 45110 Ioannina, Greece*

[2] *INFN Laboratory Nazionali del Sud, via S. Sofia 62, 95125, Catania, Italy*

[3] *Dipartimento di Fisica e Astronomia, Universita di Catania, via S. Sofia 64, 95125, Catania, Italy*

[4] *Departamento di Fisica Aplicada, Universidad de Huelva, E-21071, Huelva, Spain*

[5] *CEA-Saclay, DAPNIA-SPhN, 91191, Gif-sur-Yvette, France*

[6] *INFN Sezione di Catania, via S. Sofia 64, 95125, Catania, Italy*

[7] *National Center for Nuclear Research, A. Soltana 7, 05-400, Otwock Warsaw, Poland*

[8] *Departimento di Fisica and INFN - Sezione di Padova, via Marzolo 8, I-35131, Padova, Italy*

[9] *INFN Sezione di Napoli, via Cinthia, I-80126, Napoli, Italy*

[10] *Heavy Ion Laboratory, University of Warsaw, Pasteura 5a, 02-093, Warsaw, Poland*

[11] *Institute of Accelerating Systems and Applications and Department of Physics, University of Athens, Greece*

Abstract

Elastic scattering measurements have been performed for the ^{6}Li + p system in inverse kinematics at the energies of 16, 20, 25 and 29 MeV. The heavy ejectile was detected by the large acceptance MAGNEX spectrometer at the Laboratori Nazionali del Sud (LNS) in Catania, Italy. Preliminary results will be presented and discussed for the highest energy.

Keywords: `elastic scattering`, `coupling channel calculations`, `compound versus direct`

*e-mail:apakou@cc.uoi.gr

1. Introduction

In a long term plan, we have undertaken in this laboratory systematic work [1, 2, 3, 4, 5, 6, 7, 8, 9], concerning the optical potential or/and the structure of nuclei via A+p elastic scattering and reactions (A: weakly bound stable or radioactive light nucleus). All these studies but the [9], were performed at energies well above $E_{proj.}$=10MeV/A. In [9] we have performed measurements with the radioactive nucleus ^{17}F at E$\sim$ 4MeV/A putting on stake the validity of the microscopic JLM potential. This potential was derived by Jeukenne, Lejeune and Mahaux [10] and applied for stable nuclei by Mellema et al. [12], Hansen et al. [13] and Petler et al. [14] for medium and heavy mass stable nuclei and for energies above 10MeV/A, with slight adjustments only on the imaginary part. In this respect, herewith, the elastic scattering and reactions were studied for ^{6}Li+p in inverse kinematics at near barrier energies with possible relevant interest on astrophysical problems. While for the ^{17}F study measurements were performed off resonance, for ^{6}Li we have gone a step forward, performing the measurement on resonance, and exploring the case of compound versus direct couplings to continuum.

The reactions of nucleons and light nuclei with ^{6}Li are of great practical and theoretical importance, with serious consequences on astrophysical problems. The determination of low-energy cross sections, which belong to a deep sub-barrier region is a difficult task both from the theoretical and experimental point of view and the possible approach relies on extrapolations. The latter is based on the exact form of the potential barrier, the potential penetrability and the extrapolation of S-factors to zero energy.

The ^{6}Li nucleus exhibits a pronounced cluster structure with a very small binding energy in the α-d channel and a low density of its excited states up to excitation energy of 16 MeV. Under these conditions, the choice of a standard optical potential is inapplicable. Therefore, in principle, elastic scattering measurements and induced reaction measurements as well as total reaction cross

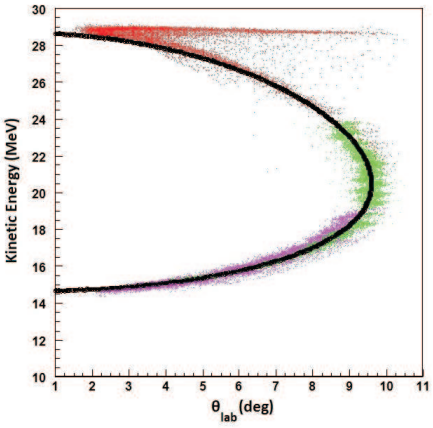

Figure 1: A reconstructed ^{6}Li+p spectrum. The two kinematical solutions of the reaction, were obtained in 3 different runs with 3 sets of magnetic fields. The plot shows the superposition of these runs, designated with different colors. The black solid line represents the theoretical prediction which seems to describe perfectly well the data, giving further support to the accurate spectrum reconstruction.

sections at low energies for a detailed CRC approach could be very usefull.

In the LIPMAGNEX experiment we have proposed the study of ^{6}Li+p, in a full angular distribution measurement to probe both the elastic scattering in a precise way and also the direct (breakup) and compound reactions. This give us the opportunity to explore coupling effects on the compound as well as to direct contributions in a more detailed way. We have planned our experiment in the MAGNEX facility [15, 18, 19], which is a powerful tool for detecting both heavy and light ejectiles with a very good angular and energy resolution. As it will be shown later in another article the MAGNEX spectrometer was inevitably a very appropriate solution for the breakup measurement.

In the present article we present a preliminary analysis of the first part of this study, referring to the elastic scattering at the highest energy of 29MeV. A detailed compilation of elastic scattering measurements for p+^{6}Li can be found in [25]. Measurements in a wide energy range (E$_p$=1.8 to 12MeV) and a rather wide angular range θ_{lab}=30^0 to 160^0 are found in [26] while polarisation and

phase shift measurements in [27] for E_p=0.5 to 5.6MeV. The difficult experimental problem of these measurements to determine the thickness of a lithium target, results in relative measurements and absolute only via normalisation to previous ones introducing large errors. Furtheron, due to single stage silicon detectors used, elastic events are not separated from reaction events, the last ones creating a continuum background which has to be subtracted from the total rate. Finally all these measurements are mainly focused on the ^{7}Be structure and not on the potential but the Haller et al. [26], where an optical potential is used to fit the data allowing the various parameters to strongly depend on energy. The polarisation measurements fail to give a clear analysis due to several parameters which have to be determined. Between these parameters we note the unknown total reaction cross section needed to fit absorption. Theoretical approaches to probe the potential, in a folding and CC context are found in [28, 29, 30], but they deal with data at rather high energies above E_p=25 MeV. Interest present two recent articles [22, 23] with CDCC calculations (Continum Discretized Coupled Channel) and calculations with a microscopic M3Y potential respectively from rather low to higher energies ($\sim$5 to 25MeV/A). The first calculations show unexpectedly that couplings to continumm without considering any compound contribution can describe adequately well previous experimental results.

Within our experimental approach we focus on a precise, clear from the above described uncertainties, elastic scattering measurement, predesessor to measurements on MAGNEX with radioactive projectiles in inverse kinematics. This measurement will be the first step for obtaining the optical potential and subsequently for describing the various reaction processes.

2. The Experiment: Results and Discussion

The experiment was performed at (LNS - INFN) Istituto Nazionale di Fisica Nucleare Laboratori Nazionali del Sud in Catania, Italy. Beams of $^6Li^{3+}$ were accelerated at the energies 16, 20, 25 and 29MeV and impinged on a 240 μg/cm^2 CH_2 target. Measurements were repeated with a ^{12}C target of similar thickness,

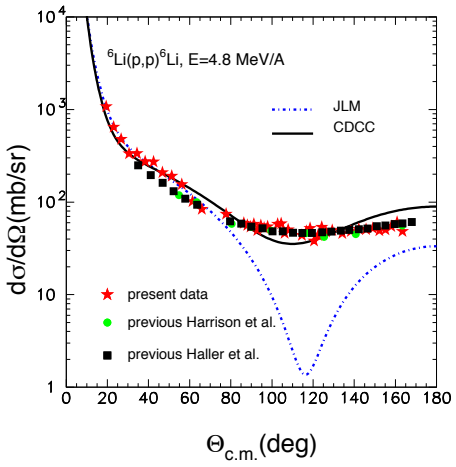

Figure 2: Present elastic scattering data for ^{6}Li+p at 28MeV are compared with previous values as well as with JLM and CDCC calculations.

for estimating the carbon background. The elastically scattered lithium ions were momentum analyzed by the MAGNEX spectrometer [15, 18, 19], set at θ_{opt}=4^0, working in the total horizontal angular acceptance and detected by its focal plane detector [17]. The vertical acceptance of MAGNEX was reduced for protecting the focal plane detectors from the elastic high counting rate. Our data reduction technique, based on a differential algebraic method [20] and the performances of the whole system are described in Refs [16, 21]. The two kinematical solutions of the ejectiles were measured by the application of three different magnetic fields. A typical reconstructed spectrum at projectile energy of 29 MeV, is displayed in Figure 1. In this Figure, the reconstructed kinematical spectrum was obtained with the superposition of the 3 different sets, which are designated with different colors. Overlapping regions between sets I, II and III ensured the consistency between the different sets. The beam charge was collected by a Faraday cup, set at the entrance of MAGNEX and its absolute value was reconfirmed via the measurement at the very forward angles, where the elastic scattering is Rutherford. For an angular step of $\sim 0.5^0$,

the counts were integrated and the solid angle, defined by 4 slits located at 250mm from the target, was calculated taking into account the contour of the reconstructed (θ_i, ϕ_i) locus [36]. The solid angle uncertainty is estimated to be $\sim$2%. The differential cross sections, obtained at the projectile energy of 29 MeV are compared in Figure 2 with previous measurements as well as with JLM and CDCC calculations. For the CDCC calculation we follow the same technique as in [37], where we present calculations for the same system but at a much higher energy, 155MeV/A. A cluster α + d model of ^{6}Li was adopted, with all the parameters of the model including discretization and truncation described in detail in [38]. The central potential in the ^{6}Li + p entrance channel as well as all the coupling potentials used in the calculations were derived from empirical p - α and d - p potentials by means of a single - folding method. For that the data sets of Hinterberger *et al.* [39] for d + p elastic scattering at E_d = 52 MeV and by Plummer *et al.* [40] for p + α elastic scattering at E_p = 26.1 MeV were used. It should be noted however that the depth of the imaginary part of the input d + p potential was multiplied for the 155MeV data by a normalization factor N_i=1.7, simulating the strong contribution of the transfer channel. In the present case however for this low projectile energy this normalization was set equal to N_i=0.1 according to the systematic study of nucleon scattering from ^{6}Li with the CDCC method by Matsumoto, Guo [22, 24]. In these studies the authors have revealed the strong dependence of the input optical potentials on the energy of the neutron/proton beam.

It is obvious that for this weakly bound projectile, the description of the experimental data can not be done simply adopting the microscopic JLM potential as in the ^{17}F case [9]. Couplings in the continuum are strong and reproduce in principle the trend of the data, but still they leave space to compound contributions. Calculations taking into account the compound couplings, are under progress and will be presented in our next publication. Also the analysis of the breakup channel data is under progress and it could reveal the validity of the CDCC calculations.

Acknowledgments: The research leading to these results has received fund-

ing from the European Union Seventh Framework Programme FP7/2007- 2013 under Grant Agreement No. 262010-ENSAR.

References

[1] N. Alamanos et al., Nucl. Phys. A660,406(1999).

[2] A. Pakou et al., Nucl. PHys. A691,661(2001).

[3] N. Alamanos et al., J. Phys. G 24, 541(1998).

[4] A. de Vismes et al., Phys. Lett. B505, 15 (2001).

[5] A. Lagoyiannis et al., Phys. Lett. B518, 27(2001).

[6] V. Lapoux et al., Nucl. Phys. A722, 49c(2003).

[7] F. Skaza et al., Phys. Lett. B619,82 (2005).

[8] A. Gillibert et al., Nucl. Phys. A787, 423c (2007).

[9] N. Patronis et al., Phys. Rev. C85, 024609 (2012).

[10] J. P. Jeukenne, A. Lejeune, C. Mahaux, Phys. Rev. C 16, 80 (1977).

[11] F. Petrovich at al., Nucl. Phys. A 563, 387 (1993).

[12] S. Mellema, R. W. Finley, F. S. Dietrich, F. Petrovich, Phys. Rev. C 28, 2267 (1983).

[13] L. F. Hansen et al., Phys. Rev. C 31, 111 (1985).

[14] J. S. Petler, M. S. Islam, R. W. Finley, F. S. Dietrich, Phys. Rev. C 32, 673 (1985).

[15] A. Cunsolo et al., Eur. Phys. J. Special Topics 150 (2007) 343.

[16] F. Cappuzzello et al., NIM A 621 (2010) 419.

[17] M. Cavallaro et al., Eur. Phys. J. A 48 (2012) 59.

[18] A. Cunsolo et al., NIM A 484, 56 (2002).

[19] A. Cunsolo et al., NIM A 481, 48 (2002).

[20] F. Cappuzzello et al., NIM A 638 (2011) 74.

[21] M. Cavallaro et al., NIM A 648 (2011) 46.

[22] Guo et al., Phys. Rev. C87, 024610 (2013).

[23] M.Y.H. Farag et al., Phys. Rev. C88, 064602 (2013).

[24] T. Matsumoto *et al.*, Phys. Rev. C **83**, 064611 (2011).

[25] M. Skill et al., Nucl. Phys. **A 581**, 93 (1995).

[26] W. D. Harisson and A. B. Writehead, Phys. Rev **132** (1963) 2607; M. Haller et al., Nucl. Physics **A 496**(1989)189.

[27] C. Petitjean, L. Brown, R. G. Seyler, Nucl. Phys. **A 129**(1969)209; Haller et al., Nucl. Physics **A 496**(1989)205.

[28] K. H. Bray et al., Nucl. Phys. **A 189**(1992)35.

[29] B. A. Mughrabi, Z. El Itaoui, P. J. Ellis, Y.C. Tang; Phys. Rev **C 29**(1984)29.

[30] F. Petrovich et al., Nucl. Phys. **A 563** (1993) 387.

[31] J. Cruz et al., Journal of Phys. **G 35** (2007) ; A. Tumino et al., Nucl. Phys. **A 734**(2004)639; Chia-Shou Lin et al., Nucl. Phys. **A 275** (1977) 93; A. J. Elwyn et al., Phys. Rev. **C 20** (1979) 1984; K. Schenk, M. Morike, G. Staudt Phys. Lett. **52B** (1974)36; G. P. Johnston and D. G. Sargood, Nucl. Phys. **A 224** (1974)349; U. Fasoli, D. Toniolo and G. Zago, Phys. lett. **B 8**(1964) 127.

[32] V. Valkovik, C. Joseph, S. T. Emerson and G. C. Phillips, Nucl. Phys. **A106**(1968)138; J. L. Durand, J. Arvieux, C. Perrin and G. Perrin, Phys. Lett, **53B** (1974) 57.

[33] M. Arvigeanu, W. von Oertzen, U. Fischer, V. M. Arvigeanu; Nucl. Physics **A759**(2005)327.

[34] A. N. Ostrowski et al., Phys. Rev **C 63**(2001)024605.

[35] R. Lipperheide, Nucl. Phys. **A 469** (1987) 190.

[36] M. Cavallaro et al., NIM A 637, 77 (2011).

[37] K. Rusek, K.W. Kemper, R. Woslki, Phys. Rev. C **64**, 044602 (2001).

[38] K. Rusek, P.V. Green, P.L. Kerr, K.W. Kemper, Phys. Rev. C **56**, 1895 (1997).

[39] F. Hinterberger, G. Mairle, U. Schmidt-Rohr, G.J. Wagner, Nucl. Phys. **A111**, 265 (1968).

[40] D.J. Plummer, K. Ramavataram, T.A. Hodges, D.G. Montague, A. Zucker, N.K. Ganguly, Nucl. Phys. **A174**, 193 (1971).

[41] Hairui Gpo *et al.*, Phys. Rev. C **87**, 024610 (2013).

Enhanced proton-neutron interactions and emergent collectivity in nuclei

S. Karampagia and Dennis Bonatsos[1]

Institute of Nuclear and Particle Physics,
National Centre for Scientific Research Demokritos,
15310 Aghia Paraskevi, Attiki, Greece

Abstract

Enhanced proton-neutron interactions occur in heavy nuclei along a trajectory of approximately equal numbers of valence protons and neutrons. This is also closely aligned with the trajectory of the saturation of quadrupole deformation. The origin of these enhanced p-n interactions is discussed in terms of spatial overlaps of proton and neutron wave functions that are orbit-dependent. It is suggested for the first time that nuclear collectivity is driven by synchronized filling of protons and neutrons with orbitals having parallel spins, identical orbital and total angular momenta projections, belonging to adjacent major shells and differing by one quantum of excitation along the z-axis. These results may lead to a new approach to symmetry-based theoretical calculations for heavy nuclei.

Keywords: `nuclear collectivity`, `proton-neutron interaction`

1. Empirical p-n Interactions

A measure of the average p-n interaction of the last nucleons can be extracted from a double difference of binding energies, called δV_{pn} [1]. In Ref. [2] it was shown that δV_{pn} has large singularities for light $Z{=}N$ nuclei linked [3] to maximal spatial-spin overlaps of proton and neutron wave functions.

[1]e-mails: skaram@inp.demokritos.gr, bonat@inp.demokritos.gr

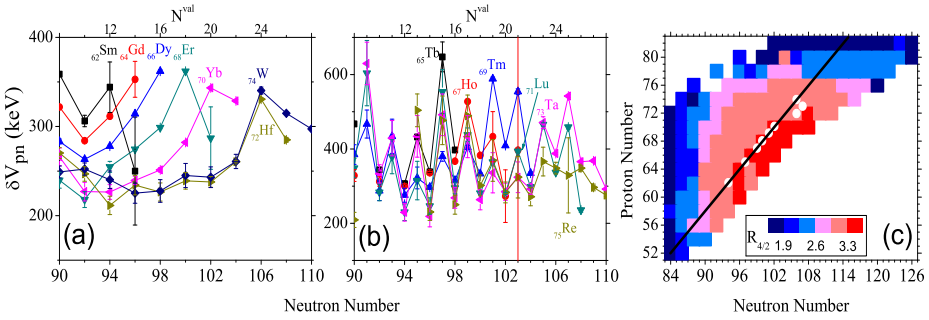

Figure 1: (Taken from Ref. [5].) Empirical δV_{pn} values for even-Z nuclei (Based on Ref. [4]) (a). Empirical δV_{pn} values for odd-Z nuclei (b). Color coded contour plot of empirical $R_{4/2}$ values in the Z= 50-82, N= 82-126 shells (c). The line drawn represents the line of Z_{val}=N_{val}. The white circles are the nuclides for each Z where the largest δV_{pn} value is observed.

δV_{pn} values in heavy nuclei show similar, though highly muted, peaks [4], as shown in Fig. 1(a), when the number of *valence* neutrons equals the number of *valence* protons. Furthermore, the last-filled proton and neutron Nilsson [6] orbitals are often related by $\Delta K[\Delta N,\Delta n_z,\Delta\Lambda]$=0[110], where K and Λ are the projections of the total and orbital angular momenta on the z-axis (K=$\Lambda\pm$1/2), respectively. If both the oscillator quantum number N (N=n_x+n_y+n_z) and the number of quanta in the z-direction (the deformation axis), n_z, increase by one, then n_x+n_y is constant: the two wave functions differ by a single quantum in the z-direction and are therefore highly overlapping.

The same effect is seen more clearly in odd-odd nuclei, where the last protons and last neutrons occupy specific single orbits. The panel (b) of Fig. 1 shows δV_{pn} for odd-Z nuclei with both even and odd-N. Not only do these results also show spikes, at $Z_{val} \simeq N_{val}$, but now the peaks are sharper and greatly enhanced in magnitude (about 4 times larger than for even-even nuclei).

Figure 1(c) shows the locus of maximum δV_{pn} values in an Z-N plot of $R_{4/2}\equiv$ E(4_1^+)/E(2_1^+), which varies from <2 near closed shells to ∼3.33 for well-deformed

axial rotors. The results for even-even and odd-odd nuclei closely match both the $Z_{val} \simeq N_{val}$ line and the onset of deformation occuring for $R_{4/2}$> 3.3. This highlights the link to the evolution and saturation of collectivity.

2. A Simple Model for the p-n Interactions

We directly calculated spatial overlaps of proton and neutron Nilsson wave functions. Nilsson wave functions in the form [6] $\chi_{N\Omega} = \sum_{l\Lambda} a^{\Omega}_{l\Lambda} |Nl\Lambda\Sigma\rangle$ were used, where Ω, Λ, Σ are the projections of the total particle angular momentum j, the orbital angular momentum l and the spin s on the z-axis, while the coefficients $a^{\Omega}_{l\Lambda}$ were calculated by solving the Nilsson Hamiltonian with the standard parameter values, κ= 0.0637 and μ= 0.42 for neutrons and 0.0637 and 0.6 for protons, respectively. For axially symmetric nuclei, which we deal with here, K, the projection of the total angular momentum on the z-axis, and Ω are the same. Overlaps $\int (\chi^*_{N_1\Omega_1}\chi_{N_1\Omega_1})(\chi^*_{N_2\Omega_2}\chi_{N_2\Omega_2})dV$ were calculated using spherical coordinates. Though the deformation dependence is weak, we used three values, ϵ= 0.05, 0.22 and 0.3, allocating nuclei to these categories according to $R_{4/2}$ (see Fig. 1(right)), and extending these choices to unknown nuclei using the P-factor [7].

Figure 2 shows the behavior of the overlaps against correlated differences in K and n_z as well as against differences in each of the Nilsson quantum numbers. In panel (a) the overlaps are highest when ΔK and Δn_z are small, including the case of present interest 0[110]. The overlaps generally fall off for larger ΔK and Δn_z values.

Similar conclusions are drawn in panels (b)-(f). Each point is an average over all the overlaps for that value of the difference in the relevant Nilsson quantum number. In each case, the overlaps fall off steeply as the particular quantum number differs by larger and larger amounts in the two orbits, peaking at a quantum number difference of zero or one.

Figure 3 shows empirical values of δV_{pn} (a) and our calculated overlaps (b and c). Overall the agreement is quite good given the simplicity and parameter

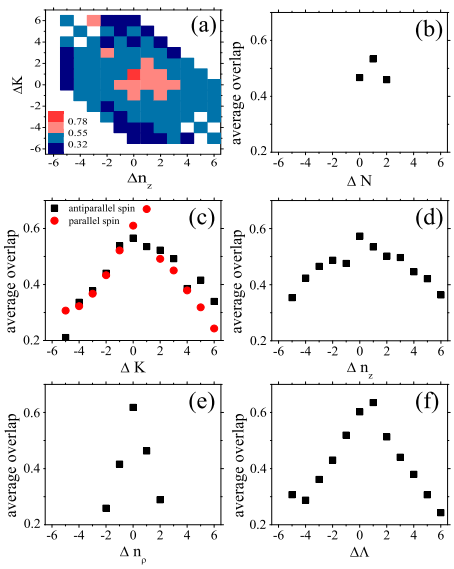

Figure 2: (Taken from Ref. [5].) Calculated average spatial overlaps (for a deformation ϵ= 0.22) for proton and neutron orbitals in the Z= 50-82, N= 82-126 region against the differences (neutron orbit minus proton orbit) in their K and n_z values in a color code (a). Other panels show average overlaps as a function of differences [ΔN (b), ΔK (c), Δn_z (d), Δn_ρ (e), $\Delta\Lambda$ (f)] in individual Nilsson quantum numbers.

free nature of our approach, and is comparable to that from Density Functional Theory (DFT) calculations [8]. The results generally show small values far from the diagonal, a spread out region of large values early in the shells, and large values near the Z_{val}=N_{val} line that shift slightly to the right of the Z_{val}=N_{val} line towards the end of the shell.

Of course, calculated values are not limited to known nuclei. Figure 3(c) shows overlaps for the full shells. Interestingly, large overlaps now also appear (as in DFT calculations [8]) in neutron-rich nuclei in the region $Z\sim$ 52-64 and $N\sim$ 92-108. Here pairs of orbitals, such as 5/2[413] with 5/2[512] and 1/2[420] with 1/2[521], coupled to S= 0, are filling (near ^{168}Gd and ^{162}Nd, respectively), that do not satisfy 0[110], which implies S= 1. Measurement of masses in these regions, which may be available in the future at FAIR, FRIB, and RIKEN, would offer important tests of the current ideas.

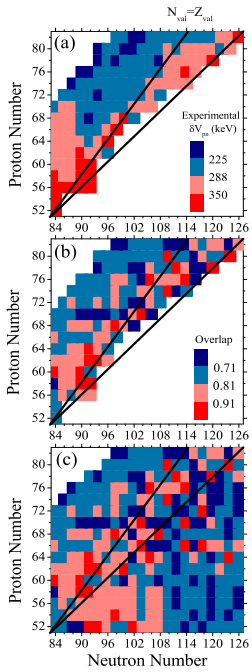

Figure 3: (Taken from Ref. [5].) Color coded empirical δV_{pn} values for the Z= 50-82 and N= 82-126 shells (a). Large values have redder colors. Similar as (a) but for calculated overlaps for nuclei where empirical values of δV_{pn} are known (b). Calculated overlaps for the full major shells (excluding nuclei beyond the proton dripline) (c). The upper (lower) black lines represent Z_{val}=N_{val} (equal fractional filling).

3. Implications for the Development of Collectivity and Deformation

The idea of p-n Nilsson orbital pairs related by 0[110] has a much deeper consequence related to the overall emergence of collectivity in nuclei. In Fig. 4 we show standard proton (a) and neutron (b) Nilsson diagrams for this mass region. We first note that every one of the 16 Nilsson proton orbitals for the entire shell, including the unique parity orbitals, has a 0[110] neutron partner. This in itself is perhaps not surprising since the neutron shell has one additional quantum. However, a closer look shows a general pattern, not heretofore recognized, namely, that, these 0[110] pairs fill almost *synchronously* as the proton and neutron shells fill.

Since the patterns of up-and down- sloping orbits and orbit crossings are similar in the two shells, this synchronous filling of 0[110] combinations approximately persists even as the deformation increases. This synchronous filling sequence correlates with, and gives a microscopic basis to, the empirical phenomenon of enhanced collectivity along the Z_{val}=N_{val} line.

It is only past mid-shell that neutron orbitals occur (6 of 22) that do not have a 0[110] proton partner. Interestingly, each of these has n_z= 0, that is, oblate orbitals that do not contribute to prolate deformation. The interspersing of these rogue n_z= 0 orbitals late in the shell interrupts the Z_{val}=N_{val} correlation with maximal δV_{pn}, leading to shifts in peaks in δV_{pn} to N_{val}=Z_{val}+2 noted e.g. in the Hf-W and Lu-Ta regions).

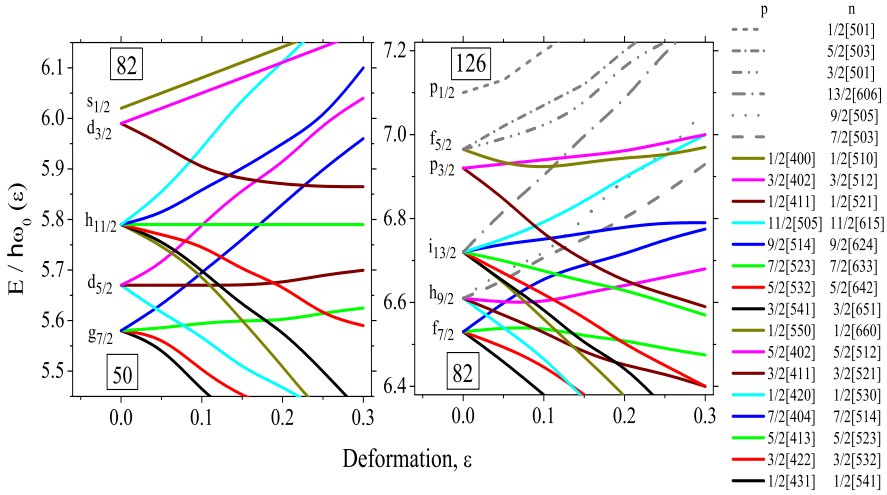

Figure 4: (Taken from Ref. [5].) Nilsson diagrams for the proton (a) Z= 50-82 and neutron (b) N= 82-126 shells. The sequential filling of $\Delta K[\Delta N,\Delta n_z,\Delta\Lambda]$=0[110] pairs is closely followed for most deformations in the actual Nilsson diagram as seen by the corresponding color coding of respective proton and neutron orbitals. Neutron orbitals without 0[110] proton partners (these have n_z= 0) are shown as black lines in the neutron Nilsson diagram.

4. A possible new Pseudo-Shell approach to Heavy Nuclei

The 0[110] correlation is repeatedly encountered from the *sd* shell to the actinides. This generality may suggest a new coupling scheme, similar in spirit to the idea of pseudo-SU(3) [9, 10], but different in content. The 50-82 major shell is formed by the orbits of the *sdg* oscillator shell, with the exception that the $1g_{9/2}$ orbit has escaped into the 28-50 major shell, and is replaced by the $1h_{11/2}$ orbit, from the pfh oscillator shell. As a result, the $sdg_{7/2}h_{11/2}$ 50-82 shell (with the single orbital 11/2[505] left out) can be considered as an approximate *sdg* shell by replacing the $1h_{11/2}$ orbitals by their 0[110] counterpart $1g_{9/2}$ orbitals. Whereas, in pseudo-SU(3), the entire unique parity orbit is excised, here only the single, highest K, Nilsson orbital is excluded. The new scheme could simplify symmetry-based shell model calculations. Instead of two pseudo-SU(3) shells (with SU(3) subalgebras) plus two shell model single-j shells (not possessing SU(3) subalgebras), one has just two approximate shells with SU(3) subalgebras (plus two high-lying high-K single orbitals, which can often be ignored), thus deriving from the shell model an approximate SU(3) symmetry for heavy nuclei, at least for $Z_{val} \simeq N_{val}$.

To proceed further, one has to choose a Hamiltonian containing, in addition to the usual quadrupole-quadrupole and angular momentum terms, SU(3) symmetry preserving third-order and/or fourth-order terms [10, 11]. Work in this direction is in progress. Finally, the 0[110] proton-neutron pairs considered in the present work have $S = 1$. The presence of isoscalar $S = 1$ proton-neutron pairs in competition with isovector $S = 0$ nucleon pairs has long been considered in medium mass nuclei with $Z \simeq N$ [12, 13]. The present work suggests that similar studies for heavy nuclei with $Z_{val} \simeq N_{val}$ should be performed.

Acknowledgments: No support from any Greek or European Union funding agency is acknowledged.

[1] J.D. Garrett and Z.-Y. Zhang, Int. Conf. on Contemporary Topics in Nuclear Structure Physics, Cocoyoc, Mexico, June, 1988, and J.-Y. Zhang, R.F. Casten, and D.S. Brenner, Phys. Lett. B **227** (1989) 1.

[2] D.S. Brenner, C. Wesselborg, R.F. Casten, D.D. Warner and J.-Y. Zhang, Phys. Lett. **243 B** (1990) 1.

[3] P. Van Isacker, D.D. Warner and D.S. Brenner, Phys. Rev. Lett. **74** (1995) 4607.

[4] R.B. Cakirli, K. Blaum, and R.F. Casten Phys. Rev. C **82** (2010) 061304(R).

[5] D. Bonatsos, S. Karampagia, R.B. Cakirli, R.F. Casten, K. Blaum, and L. Amon Susam, Phys. Rev. C **88** (2013) 054309.

[6] S.G. Nilsson, Mat. Fys. Medd. K. Dan. Vidensk. Selsk. **29** (1955) no. 16.

[7] R.F. Casten, D.S. Brenner and P.E. Haustein, Phys. Rev. Lett. **58** (1987) 658.

[8] M. Stoitsov, R.B. Cakirli, R.F. Casten, W. Nazarewicz, W. Satula, Phy. Rev. Lett. **98** (2007) 132502.

[9] R.D. Ratna Raju, J.P. Draayer, and K.T. Hecht, Nucl. Phys. A **202** (1973) 433.

[10] J.P. Draayer and K.J. Weeks, Ann. Phys. (NY) **156** (1984) 41.

[11] G. Vanden Berghe, H. E. De Meyer, and P. Van Isacker, Phys. Rev. C **32** (1985) 1049.

[12] P. Federman and S. Pittel, Phys. Rev. C **20** (1979) 820.

[13] F. Šimkovic, Ch. C. Moustakidis, L. Pacearescu, and A. Faessler, Phys. Rev. C **68** (2003) 054319.

Transition from octupole deformation to octupole vibration in light actinides

Dennis Bonatsos, Andriana Martinou, S. Karampagia, and D. Petrellis[1]

Institute of Nuclear and Particle Physics, National Center for Scientific Research "Demokritos", GR-15310 Aghia Paraskevi, Attiki, Greece

N. Minkov[2]

Institute of Nuclear Research and Nuclear Energy, Bulgarian Academy of Sciences, 72 Tzarigrad Road, 1784 Sofia, Bulgaria

Abstract

The analytic quadrupole octupole axially symmetric model (AQOA) is a collective nuclear model which takes into account both quadrupole and octupole surface deformations, using an infinite well potential. It had successfully predicted that ^{226}Ra and ^{226}Th lie at the border between octupole rotation and octupole vibration in light actinides. Through the use of a Davidson potential within an AQOA-D framework, analytic expressions for energy spectra and B(E1), B(E2), B(E3) transition rates are derived. The spectra of $^{222-226}$Ra and ^{224,226}Th are described in terms of the two parameters ϕ_0 (expressing the relative amount of octupole vs. quadrupole deformation) and β_0 (the position of the minimum of the Davidson potential), while the recently determined B(EL) transition rates of ^{224}Ra, presenting stable octupole deformation, are successfully reproduced.

Keywords: `octupole deformation`, `octupole vibration`, `Ra`, `Th`, `AQOA`

1. Introduction

Octupole deformation corresponds to a reflection asymmetric (pearlike) shape[1, 2, 3]. This type of deformation occurs mostly in light actinides [4, 5, 6, 7] and

[1]e-mail: bonat@inp.demokritos.gr, amartinou@inp.demokritos.gr, skaram@inp.demokritos.gr, petrellis@inp.demokritos.gr.

[2]e-mail: nminkov@inrne.bas.bg

in some light rare earths [8, 9, 10]. Within the AQOA model [11] the nucleus exhibits both quadrupole and octupole deformations. The hallmark of octupole deformation is a negative parity band with levels $L^\pi = 1^-, 3^-, 5^-, \ldots$, lying close to the ground state band with $L^\pi = 0^+, 2^+, 4^+, \ldots$, and forming with it a single band. On the contrary, in the case of octupole vibrations a negative parity band lying systematically higher than the ground state band is observed. The displacement of the negative parity energy levels relative to the positive parity levels is usually depicted as a staggering effect.

The recent experimental verification of stable octupole deformation in ^{224}Ra [12] stirred interest in octupole deformation in the light actinides and its theoretical interpretation. The AQOA model can be made applicable to deformed nuclei near to the transition point by replacing the infinite well potential by the Davidson potential [13] of the form $\beta^2 + \beta_0^4/\beta^2$, which contains an additional free parameter, the position β_0 of the minimum of the potential well. The flexibility acquired through the replacement of the infinite well potential by the Davidson potential has been demonstrated and exploited in the case of quadrupole deformation in [14]. The analytic quadrupole octupole axially symmetric model with a Davidson potential, to be called the AQOA-D model, is the subject of the present work. In addition to the spectra of $^{222-226}$Ra [6, 7] and ^{224,226}Th [15, 16], the recently measured [12] electric transition probabilities of ^{224}Ra provide an excellent test ground for the model.

2. Formulation

In the AQOA model [11], the actinides lying on the border between the regions of octupole deformation and octupole vibrations have been described, making the following assumptions.

a) The axes of the quadrupole and octupole deformations are taken to coincide. In other words, axial symmetry is assumed, while the γ degree of freedom is ignored.

b) Levels with $K \neq 0$ (where K is the projection of the angular momentum on

the body-fixed z' axis) are ignored, since they are lying infinitely high in energy [17].

The Hamiltonian of the AQOA model reads [17, 18]

$$H = -\sum_{\lambda=2,3} \frac{\hbar^2}{2B_\lambda} \frac{1}{\beta_\lambda^3} \frac{\partial}{\partial\beta_\lambda} \beta_\lambda^3 \frac{\partial}{\partial\beta_\lambda} + \frac{\hbar^2 \hat{L}^2}{6(B_2\beta_2^2 + 2B_3\beta_3^2)} + V(\beta_2, \beta_3), \tag{1}$$

where β_2 and β_3 are the quadrupole and octupole deformations, B_2, B_3 are the mass parameters, and $\hat{L}$ is the angular momentum operator in the intrinsic frame, taken along the principal axes of inertia.

The Schrödinger equation can be simplified by introducing [17, 18]

$$\tilde{\beta}_2 = \beta_2 \sqrt{\frac{B_2}{B}}, \quad \tilde{\beta}_3 = \beta_3 \sqrt{\frac{B_3}{B}}, \quad B = \frac{B_2 + B_3}{2}, \tag{2}$$

reduced energies $\epsilon = (2B/\hbar^2)E$ and reduced potentials $v = (2B/\hbar^2)V$, as well as polar coordinates (with $0 \leq \tilde{\beta} < \infty$ and $-\pi/2 \leq \phi \leq \pi/2$) [17, 18]

$$\tilde{\beta}_2 = \tilde{\beta}\cos\phi, \quad \tilde{\beta}_3 = \tilde{\beta}\sin\phi, \quad \tilde{\beta} = \sqrt{\tilde{\beta}_2^2 + \tilde{\beta}_3^2}. \tag{3}$$

In addition, separation of variables can be achieved by assuming the potential to be of the form $v(\tilde{\beta}, \phi) = u(\tilde{\beta}) + w(\tilde{\phi}^{\pm})$, where $w(\tilde{\phi}^{\pm})$ is supposed to be of the form of two very steep harmonic oscillators centered at the values $\pm\phi_0$

$$w(\tilde{\phi}^{\pm}) = \frac{1}{2}c(\phi \mp \phi_0)^2 = \frac{1}{2}c(\tilde{\phi}^{\pm})^2, \qquad \tilde{\phi}^{\pm} = \phi \mp \phi_0. \tag{4}$$

On the above the following comments apply:

a) $\phi = 0$ corresponds to quadrupole deformation alone, while $\phi = \pm\pi/2$ corresponds to octupole deformation alone.

b) Because of the two steep oscillators involved, ϕ remains close to $\pm\phi_0$ and, therefore, the relative amount of quadrupole and octupole deformation remains constant.

3. Energy spectra

Separation of variables in the Schrödinger equation leads for the $\tilde{\beta}$-part to an equation which is exactly soluble [19, 20] in the case of the Davidson potential

[13]

$$u(\tilde{\beta}) = \tilde{\beta}^2 + \frac{\tilde{\beta}_0^4}{\tilde{\beta}^2}. \tag{5}$$

The $\tilde{\beta}$-part eigenfunctions are Laguerre polynomials, while the relevant energy eigenvalues are given by

$$E_{n,L} = 2n + a_L + 1 = 2n + 1 + \sqrt{\frac{L(L+1)}{3(1+\sin^2\phi_0)} + \frac{3}{\sin^2 2\phi_0} + \beta_0^4}. \tag{6}$$

The ϕ-part energy eigenvalues are

$$\epsilon_\phi = \sqrt{\frac{2c}{\langle\tilde{\beta}^2\rangle}}\left(n_\phi + \frac{1}{2}\right), \qquad n_\phi = 0, 1, 2, \ldots \tag{7}$$

where n_ϕ is the number of quanta in the ϕ degree of freedom, while the eigenfunctions are Hermite polynomials H_{n_ϕ}

$$\chi_{n_\phi}(\tilde{\phi}^\pm) = N_{n_\phi} H_{n_\phi}(b\tilde{\phi}^\pm) e^{-b^2(\tilde{\phi}^\pm)^2/2}, \qquad b = \left(\frac{c\langle\tilde{\beta}^2\rangle}{2}\right)^{1/4}. \tag{8}$$

The total energy in the present model is then

$$E(n, L, \phi_0, n_\phi) = E_0 + AE_{n,L} + Bn_\phi. \tag{9}$$

In what follows only bands with $n_\phi = 0$ will be considered.

4. Staggering effect

The displacement of the negative relative to the positive parity bands can be measured by the quantity

$$\Delta E(L) = E(L) - \frac{E(L-1) + E(L+1)}{2}. \tag{10}$$

A large staggering effect corresponds to octupole vibration, while small values of the above measure signify octupole deformation. Theoretical calculations within the AQOA model in the Ra and Th isotopes have predicted that the critical nuclei between the two regions are ^{226} Ra and ^{226}Th [11]. In agreement to this prediction, recent experimental results [12] suggested that ^{224}Ra possesses a stable octupole deformation.

Table 1: Matrix elements of electric transitions in ^{224}Ra. The experimental data, in units of e fm, e fm^2, e fm^3 for E1, E2, E3 respectively, have been taken from Ref. [12]. Details of the theoretical calculation can be found in [21].

m.e.	exp.	th.
$\langle 0^+ \| \| E2 \| \| 2^+ \rangle$	199±3	196
$\langle 2^+ \| \| E2 \| \| 4^+ \rangle$	315±6	323
$\langle 4^+ \| \| E2 \| \| 6^+ \rangle$	405±15	426
$\langle 6^+ \| \| E2 \| \| 8^+ \rangle$	500±60	525
$\langle 1^- \| \| E2 \| \| 3^- \rangle$	230±11	236
$\langle 3^- \| \| E2 \| \| 5^- \rangle$	410±60	334
$\langle 0^+ \| \| E2 \| \| 2^+_\gamma \rangle$	23±4	36
$\langle 0^+ \| \| E3 \| \| 3^- \rangle$	940±30	1006
$\langle 2^+ \| \| E3 \| \| 1^- \rangle$	1370±140	1137
$\langle 2^+ \| \| E3 \| \| 3^- \rangle$	<4000	1176
$\langle 2^+ \| \| E3 \| \| 5^- \rangle$	1410±190	1594
$\langle 0^+ \| \| E1 \| \| 1^- \rangle$	<0.018	0.013
$\langle 2^+ \| \| E1 \| \| 1^- \rangle$	<0.03	0.018
$\langle 2^+ \| \| E1 \| \| 3^- \rangle$	0.026±0.005	0.023
$\langle 4^+ \| \| E1 \| \| 5^- \rangle$	0.030±0.010	0.032
$\langle 6^+ \| \| E1 \| \| 7^- \rangle$	<0.10	0.042

5. Interband transitions

Analytic expressions for $B(E1)$, $B(E2)$, and $B(E3)$ transition rates within the AQOA-D model have been determined in [21]. Then the minimum set of data needed includes

a) A few energy levels of both positive and negative parity, from which the parameters ϕ_0 and β_0 can be determined.

b) At least one $E2$ transition between positive parity states and one $E2$ transition between negative parity states, from which the parameter b can be determined.

c) At least one $E3$ transition, from which, in combination with the $E2$ transitions of b), the parameter ratio B_2/B_3 can be determined.

From these pieces of data

a) The spectrum (leaving out the γ bands) is determined up to an overall scale factor.

b) All relevant $E2$ and $E3$ transitions are determined up to an overall scale factor.

c) All relevant $E1$ transitions are determined up to another overall scale factor.

Successful fits for the spectra of $^{222-226}$Ra and ^{224,226}Th have been obtained in [21]. Furthermore, matrix elements of the electric transitions in ^{224}Ra obtained by both theory [21] and experiment [12] are given in Table 1, with very good agreement observed. Octupole deformation corresponds to large $E3$ matrix elements. Normally these transitions between positive and negative parity levels are supposed to have small values.

6. Conclusions

The analytic quadrupole octupole axially symmetric model with an infinite well potential (AQOA-IW) had successfully predicted the border between the regions of octupole deformation and octupole vibrations in the light actinides, identifying ^{226}Ra and ^{226}Th as border nuclei [11], with heavier isotopes corresponding to octupole vibrations and lighter isotopes exhibiting octupole deformation. The AQOA-IW model involved only one free parameter, ϕ_0, expressing the relative presence of quadrupole vs. octupole deformation, while a parameter-free version has also been developed later [22].

In the present work, the infinite well potential is substituted by a Davidson potential, resulting in the AQOA-D model, which is able to deviate from the border line into the region of octupole deformation. This is achieved through the extra parameter β_0, the position of the minimum of the Davidson potential, which is increasing with increasing $R_{4/2}$ ratios, as it is known from its use in the

description of quadrupole deformed nuclei [14]. Within the AQOA-D model, analytic expressions for energy spectra and $B(E1)$, $B(E2)$, $B(E3)$ transition rates and energy spectra are derived. Very good agreement with the recent experimental results for transition rates in ^{224}Ra [12] has been obtained.

It is of interest to apply the present model in the actinides close to ^{240}Pu, in which a second order shape phase transition from octupole-nondeformed to octupole-deformed shapes has been recently found [23], while octupole bands have been described [24] using supersymmetric quantum mechanics. The light rare earths, in which octupole bands have been considered recently both by the Bizzeti and Bizzeti-Sona approach [25] and within density functional theory [26], are also of special interest. A successful application of the AQOA-IW model to ^{148}Nd has already been given in Ref. [27].

Acknowledgments: No support from any Greek or European Union funding agency is acknowledged.

[1] S. G. Rohoziński, Rep. Prog. Phys. **51** (1988) 541.

[2] I. Ahmad and P. A. Butler, Annu. Rev. Nucl. Part. Sci. **43** (1993) 71.

[3] P. A. Butler and W. Nazarewicz, Rev. Mod. Phys. **68** (1996) 349.

[4] P. Schüler *et al.*, Phys. Lett. B **174** (1986) 241.

[5] I. Wiedenhöver *et al.*, Phys. Rev. Lett. **83** (1999) 2143.

[6] J. F. C. Cocks *et al.*, Phys. Rev. Lett. **78** (1997) 2920.

[7] J. F. C. Cocks *et al.*, Nucl. Phys. A **645** (1999) 61.

[8] W. R. Phillips, I. Ahmad, H. Emling, R. Holzmann, R. V. F. Janssens, T. L. Khoo, and M. W. Drigert, Phys. Rev. Lett. **57** (1986) 3257.

[9] W. R. Phillips, R. V. F. Janssens, I. Ahmad, H. Emling, R. Holzmann, T. L. Khoo, and M. W. Drigert, Phys. Lett. B **212** (1988) 402.

[10] P. D. Cottle, Phys. Rev. C **41** (1990) 517.

[11] D. Bonatsos, D. Lenis, N. Minkov, D. Petrellis, and P. Yotov, Phys. Rev. C **71** (2005) 064309.

[12] L. P. Gaffney, *et al.*, Nature (London) **497**(2013) 199.

[13] P. M. Davidson, Proc. R. Soc. London Ser. A **135** (1932) 459.

[14] D. Bonatsos, E. A. McCutchan, N. Minkov, R. F. Casten, P. Yotov, D. Lenis, D. Petrellis, I. Yigitoglu, Phys. Rev. C **76** (2007) 064312.

[15] A. Artna-Cohen, Nucl. Data Sheets **80** (1997) 227.

[16] Y. A. Akovali, Nucl. Data Sheets **77** (1996) 433.

[17] A. Ya. Dzyublik and V. Yu. Denisov, Yad. Fiz. **56** (1993) 30 [Phys. At. Nucl. **56** (1993) 303].

[18] V. Yu. Denisov and A. Ya. Dzyublik, Nucl. Phys. A **589** (1995) 17.

[19] J. P. Elliott, J. A. Evans, and P. Park, Phys. Lett. B **169** (1986) 309.

[20] D. J. Rowe and C. Bahri, J. Phys. A **31** (1998) 4947.

[21] D. Bonatsos, A. Martinou, N. Minkov, S. Karampagia, and D. Petrellis, to be published.

[22] D. Lenis and D. Bonatsos, Phys. Lett. B **633** (2006) 474.

[23] R. V. Jolos, P. von Brentano, and J. Jolie, Phys. Rev. C **86** (2012) 024319.

[24] R. V. Jolos, P. von Brentano, and R. F. Casten, Phys. Rev. C **88** (2013) 034306.

[25] P. G. Bizzeti and A. M. Bizzeti-Sona, Phys. Rev. C **81** (2010) 034320.

[26] R. Rodríguez-Guzmán, L. M. Robledo, and P. Sarriguren, Phys. Rev. C **86** (2012) 034336.

[27] M. Sugawara and H. Kusakari, Phys. Rev. C **35** (2007) 067302.

Exclusive muon capture rates

P.G. Giannaka[1], T.S. Kosmas[2]

Department of Theoretical Physics, University of Ioannina
GR-45110 Ioannina, Greece

Abstract

In this work, starting from state-by-state calculations of exclusive rates of the ordinary muon capture (OMC), we evaluated total rates for the nuclear isotopes ^{28}Si and ^{56}Fe. One of our main goals is to provide a reliable description of the charged-current transitions matrix elements entering the description of other similar semileptonic nuclear processes like the electron capture on nuclei, single $\beta^{\pm}$-decays and charged-current neutrino-nucleus reactions which play important role in currently interesting laboratory and astrophysical applications like the neutrino-nucleosynthesis and neutrino-detection through lepton-nucleus interaction probes.

Keywords: `semi-leptonic charged-curent reactions`, `ordinary muon capture`, `neutrino nucleosynthesis`

1. Introduction

In this work, we study the OMC represented by the reaction [1]

$$\mu_b^- + (A, Z) \rightarrow (A, Z-1)^* + \nu_\mu, \tag{1}$$

where (A, Z) denotes the initial atomic nucleus while $(A, Z-1)^*$ stands for an excited state of the daughter nuclear isotope. Since muon-capture in nuclei presents many advantages for the study of both nuclear structure and the fun-

[1]e-mail:pgiannak@cc.uoi.gr
[2]e-mail:hkosmas@uoi.gr

damental electro-weak interactions [2], the reaction (1) has been the subject of extensive experimental and theoretical investigations started early on 50's [3, 4].

Recently, the interest of studying μ^--capture has been revived [5, 6] due to its prominent role in testing the nuclear models employed in several physical applications in neutrino physics and astrophysics [7, 8]. Specifically, μ^--capture is a very useful test for various nuclear methods used to investigate semi-leptonic weak charged-current reactions as the electron capture in the interior of stars (critical in the collapse of supernovae) [7, 8, 9], the neutrino nucleus scattering (important in the detection of astrophysical neutrinos) [7] and other reactions [2]. This is due to the fact that, the muon-capture involves a large momentum transfer and, hence, it can provide valuable information about effects which do not appear in processes like the beta-decay modes.

2. Formalism

The OMC, reaction (1), proceeds via an effective charged-current weak-interaction Hamiltonian which is written as product of a leptonic, j_μ^{lept}, and a hadronic current, $\hat{\mathcal{J}}^\mu$, as [9, 10, 11, 12]

$$\hat{\mathcal{H}}_w = \frac{G}{\sqrt{2}} j_\mu^{lept} \hat{\mathcal{J}}^\mu \tag{2}$$

where $G = G_F cos\theta_c$ with G_F and θ_c being the well known weak interaction coupling constant and the Cabbibo angle, respectively. From the nuclear theory point of view, the main focus is on the calculations of the total capture rates of the reaction (1) which are based on the evaluation of exclusive nuclear transition matrix elements of the form

$$\langle f|\widehat{H_w}|i\rangle = \frac{G}{\sqrt{2}}\, \ell^\mu \int d^3x\, e^{-i\mathbf{qx}} \langle f|\widehat{\mathcal{J}_\mu}|i\rangle. \tag{3}$$

where $|i\rangle$ and $|f\rangle$ denote the initial (ground) and the final nuclear states, respectively. The quantity $\ell^\mu e^{-i\mathbf{qx}}$ stands for the leptonic matrix element written in coordinate space with $\mathbf{q}$ being the 3-momentum transfer. The magnitude of $\overrightarrow{q}$ is defined from the kinematics of the process and is approximately given by

$$q \equiv q_f = m_\mu - \epsilon_b + E_i - E_f \tag{4}$$

where m_μ is the muon rest mass, ϵ_b is the muon-binding energy in the muonic atom, E_i denotes the energy of the initial state of the parent nucleus and E_f the final energy of the corresponding daughter nucleus [6, 13].

In the unified description of all semi-leptonic electro-weak processes in nuclei developed by Donnelly and Walecka [10], the computation of each partial transition rate of the muon capture is written in terms of the eight different nuclear matrix elements (between the initial $|J_i\rangle$ and the final $|J_f\rangle$ states) as

$$\Lambda_{i\to f} = \frac{2G^2 q_f^2}{2J_i+1} R_f \Big[\big| \langle J_f \| \Phi_{1s} (\widehat{\mathcal{M}}_J - \widehat{\mathcal{L}}_J) \| J_i \rangle \big|^2 + \big| \langle J_f \| \Phi_{1s} (\widehat{\mathcal{T}}_J^{el} - \widehat{\mathcal{T}}_J^{magn}) \| J_i \rangle \big|^2 \Big] \quad (5)$$

where Φ_{1s} represents the muon wave function in the 1s muonic orbit. The operators in Eq. (5) refer to as Coulomb $\widehat{\mathcal{M}}_J$, longitudinal $\widehat{\mathcal{L}}_J$, transverse electric $\widehat{\mathcal{T}}_J^{el}$ and transverse magnetic $\widehat{\mathcal{T}}_J^{magn}$ multipole operators and contain polar-vector and axial-vector parts and the factor R_f in Eq. (5) takes into consideration the nuclear recoil.

3. Description of the nuclear method

For reliable predictions of partial muon-capture rates, a consistent description of the structure of the ground state $|J_i\rangle$ of the parent nucleus as well as of the multipole excitations $|J_f\rangle$ of the daughter nucleus are required. In the present work, the state-by-state muon capture rates are evaluated using Eq. (5) with the transition matrix elements between the states $|J_i\rangle$ and $|J_f\rangle$ determined with the use of the BCS and pn-QRPA equations, respectively. As it is well known, in a rather good approximation, the nucleus can be considered as a system of Z protons and N neutrons moving independently inside the nuclear volume and attracted by the nuclear center through a central strong nuclear force. This central attraction is well described by a mean field which, in our case, is assumed to be a Woods-Saxon potential with a Coulomb correction and a spin-orbit parts [9]. For a reliable nuclear Hamiltonian, in addition to the mean field, the two-nucleon correlations, known as residual two-body interaction, are necessary to be included. Towards this aim, we employed the

Bonn C-D one-boson exchange potential, but, since the initially evaluated bare nucleon-nucleon matrix-elements of the latter potential refer to all nuclides with mass number A, for a specific isotope (A, Z) studied, a renormalization of these two-body matrix elements was carried out with the use of four multiplicative parameters: The first two, known as pairing parameters $g_{pair}^{p,n}$, for protons (p) and neutrons (n), renormalize the monopole (pairing) interaction which is the part of the correlations involved at the BCS level for the description of the considered independent quasi-particles. The third, g_{pp}, tunes the particle-particle channel and the fourth, g_{ph}, renormalizes the particle-hole interaction of the Bonn C-D potential [9].

The ground state of the studied nucleus is obtained in the context of the BCS method. The solution of the relevant BCS equations gives the probability amplitudes V and U for each single particle level to be occupied or unoccupied, respectively and the single quasi-particle energies. Subsequently, we construct the excited states of the studied isotope by solving the QRPA equations. Their solution is an eigenvalue problem, which gives the X and Y amplitudes for forward and backward scattering as well as the QRPA excitation energies [9, 11, 12, 14, 15].

4. Results and Discussion

In our calculational procedure we followed three steps. At first we perform detailed calculations on exclusive OMC rates, we continue with the calculations of partial OMC rates and finally we evaluate total muon-capture rates for ^{28}Si and ^{56}Fe nuclear isotopes. These calculations have been performed twice: Once with the use of the free nucleon coupling constants $g_A = 1.262$ and the other with the use of the value $g_A = 1.135$ [6], to take into acount the rather small quenching effect indicated for medium-weight nuclei [5, 6].

4.1. State by State calculations of exclusive transition Rates in μ-capture

At first, we evaluated the exclusive μ^--capture rates $\Lambda_{i\to f}$ of Eq (5) for all multipolarities with $J^\pi \leq 5^\pm$. In Eq. (5) transitions between the ground

state $|i\rangle \equiv |0^+_{gs}\rangle$ of a spherical target nucleus and an excited state $|J^\pi_f\rangle \equiv |f\rangle$ of the resulting odd-odd nucleus are considered. Assuming, that the muon wave function, Φ_{1s}, in the region of the nuclear target is nearly constant, the integrals entering Eq. (5) can be performed by taking out of them an average value $\langle\Phi_{1s}\rangle$. Hence, the exclusive muon capture rates $\Lambda_{J^\pi_f}$ can be rewritten as:

$$\Lambda_{gs\to J^\pi_f} = 2G^2\langle\Phi_{1s}\rangle^2 R_f q_f^2 \left[\left|\langle J^\pi_f\|(\widehat{\mathcal{M}}_J - \widehat{\mathcal{L}}_J)\|0^+_{gs}\rangle\right|^2 + \left|\langle J^\pi_f\|(\widehat{\mathcal{T}}^{el}_J - \widehat{\mathcal{T}}^{magn}_J)\|0^+_{gs}\rangle\right|^2\right] \quad (6)$$

For each excitation of the daughter nucleus, our code provides us with the separate contributions induced by the components of the muon-capture operator. Relying on this possibility, we examined the multipole decomposition of the QRPA response in the muon capture reaction for the studied nuclei. In Fig. 1 we illustrate the contribution of each individual transition. We also show the contribution of the polar-vector as well as the axial-vector parts originated from the corresponding components of the weak interaction Hamiltonian. Evidently, most of the muon capture strength goes to 1^-, 1^+ and 2^- low-lying multipole excitations.

Totally for $J^\pi \leq 5^\pm$ in the model space chosen for each isotope, we have 286 states for the ^{28}Si and 488 states for the ^{56}Fe in the corresponding daughter nucleus. The variation of the exclusive rates throughout the entire excitation spectrum of the daughter nucleus in the case of the above target isotopes are demonstrated in Fig. 1. For all reactions, the rates present some characteristic clearly pronounced peaks at various excitation energies ω and specifically for transitions $J^\pi = 1^+$, 1^- but also for $J^\pi = 0^+$, 0^- and 2^- transitions.

More specifically, in the daughter ^{28}Al isotope the maximum peak corresponds to the 1^+_7 QRPA transition at $\omega = 7.712\,MeV$ (see Fig. 1(c)). Other two characteristic peaks are at $\omega = 18.135\,MeV$ and at $\omega = 18.261\,MeV$ which correspond to the 0^-_9 and 1^-_{26} transitions respectively. For the daughter isotope ^{56}Mn, we see that the maximum peak appears at $\omega = 8.278\,MeV$ and corresponds to the 1^+_{10} transition. Another important transition is that of 1^-_{38} at $\omega = 18.716\,MeV$. We note that the figures of this section, have been de-

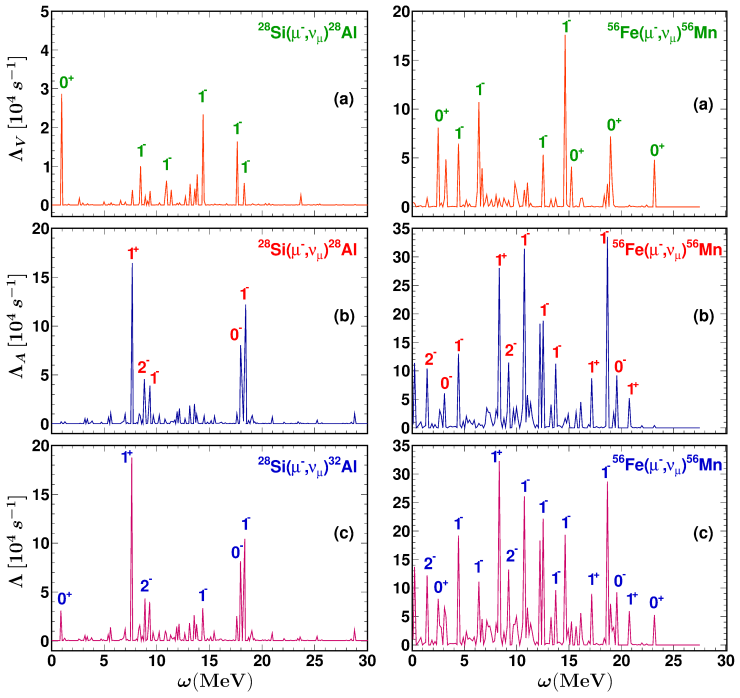

Figure 1: Individual contribution of the Polar-Vector Λ_V (pannel(a)) and Axial-Vector Λ_A(pannel (b)) to the total muon-capture rate as a function of the excitation energy ω for the ^{28}Si and ^{56}Fe nuclei.

signed by using the ROOT program of Cern with binning width 0.112 and 0.15, respectively, for ^{28}Si and ^{56}Fe nuclei.

4.2. Total Muon-Capture-Rates

In the last stage of our present work, we computed the total rates of muon-capture on the chosen set of nuclei. These rates are obtained by summing over all partial multipole transition rates in two steps. At first, we sum up the contribution of each final state of a specific multipolarity, and then, we sum over the multipole responses (up to $J^\pi = 4^\pm$) as

$$\Lambda_{tot} = \sum_{J^\pi} \sum_{f} \Lambda_{J^\pi_f} \tag{7}$$

The results are tabulated in Table 1, where for the sake of comparisson we also include the experimental total rates as well as the theoretical ones of Refs. [5]

and [6]. Moreover, in Table 1 we show the individual contribution in the total muon capture rate of the polar-vector (Λ^{V}_{tot}), the axial-vector (Λ^{A}_{tot}), and the overlap (Λ^{VA}_{tot}) parts.

Table 1: Individual contribution of Polar-vector, Axial-vector and Overlap part to the total muon-capture rate. Comparison between the total muon capture rates obtained by using the pn-QRPA with the quenched value of $g_A = 1.135$ for medium-weight nucleus ^{56}Fe and the free nucleon coupling constant $g_A = 1.262$ for the light nucleus ^{28}Si with the available experimental data and with the theoretical rates of Ref [5], Ref [6].

Total Muon-capture rates $\Lambda_{tot}(\times 10^6)s^{-1}$							
	Present pn-QRPA Calculations				Experiment	Other theoretical Methods	
Nucleus	Λ^{V}_{tot}	Λ^{A}_{tot}	Λ^{VA}_{tot}	Λ_{tot}	Λ^{exp}_{tot}	Λ^{theor}_{tot} [5]	Λ^{theor}_{tot} [6]
^{28}Si	0.150	0.751	-0.009	0.892	0.871	0.823	0.789
^{56}Fe	1.075	3.179	-0.129	4.125	4.411	4.457	4.723

As can be seen, our results are in very good agreement with the experimental total muon-capture rates. For all studied nuclei the deviations from the corresponding experimental rates are smaller than 7% when using the quenched g_A. So, for the reliability of our results it is necessary to take into account the quenching effect.

5. Summary and Conclusion

In the present work, we performed detailed calculations for all multipole transition matrix elements entering the exclusive muon-capture rates for the isotopes ^{28}Si and ^{56}Fe. Results for the exclusive rates through extensive state-by-state calculations and subsequently for the total muon capture rates for the above isotopes were computed. The muon-capture studies on these nuclei demonstrate that the used pn-QRPA method may provide an accurate description of the

charged current semileptonic weak interaction processes. As the inclusive muon capture rates and the cross section of the antineutrino-induced charged current reactions are closely related, we can adopt this method to study other types of charge-changing weak interaction processes as, electron-capture, beta-decay modes, etc.

Acknowledgments: This research has been co-financed by the European Union (European Social Fund-ESF) and Greek national funds through the Operational Program "Education and Lifelong Learning" of the National Strategic Reference Framework (NSRF) - Research Funding Program: Heracleitus II. Investing in knowledge society through the European Social Fund.

[1] E. Kolbe, K. Langanke and P. Vogel, *Nucl. Phys. A* **613** (1997) 382.

[2] T.S. Kosmas, *Nucl. Phys. A* **683** (2001) 443.

[3] N.C. Mukhopadhyay, *Phys. Rep.* **50** (1977) 1.

[4] D.F. Measday, *Phys. Rep.* **354** (2001) 243.

[5] N.T. Zinner, K. Langanke and P. Vogel, *Phys. Rev. C* **74** (2006) 024326.

[6] T. Marketin, N. Paar, T. Niksic and D. Vretenar, *Phys. Rev. C* **79** (2009) 054323.

[7] K. Langanke, G. Martinez-Pinedo, *Rev. Mod. Phys.* **75** (2003) 819.

[8] D.J. Dean, K. Langanke, et al. *Phys. Rev. C* **58** (1998) 536.

[9] P.G. Giannaka, T.S. Kosmas, Adv. High Energy Phys. 2014 (2014) 398796.

[10] T.W. Donnelly and R.D. Peccei, Phys. Rep. **50** (1979) 1.

[11] V.C. Chasioti, T.S. Kosmas, *Nucl. Phys. A* **829** (2009) 234.

[12] P.G. Giannaka, T.S. Kosmas *J.Phys.Conf.Ser.* **410** (2013) 012124.

[13] N.C. Mukhopadhyay, H.C. Chiang, et al. *Phys. Lett. B* **434** (1998) 7.

[14] V. Tsakstara and T.S. Kosmas, *Phys. Rev. C* **83** (2011) 054612.

[15] K.G. Balasi, E. Ydrefors, and T.S. Kosmas, *Nucl. Phys. A* **868** (2011) 82.

Energy Recover from PileUp Events in Silicon Detectors

E. Stiliaris

National & Kapodistrian University of Athens, Department of Physics, 15771 Athens, Greece
Institute of Accelerating Systems & Applications, 10024 Athens, Greece
and the Hellenic Institute of Nuclear Physics (HINP)

A. Pakou

The University of Ioannina, 45110 Ioannina, Greece and the Hellenic Institute of Nuclear Physics (HINP)

D. Pierroutsakou and the Members of the EXOTIC Group Collaboration

INFN, Sezione di Napoli and Padova, Italy

Abstract

An experimental technique is described in the present work capable to identify pileup events and to reconstruct the hidden energy information. The procedure is based on the pulse shape analysis of digitized signals with the help of a high frequency, fast and sensitive flash ADC. The CAEN module V1729A, operating at a maximum sampling rate of 2 GHz has been successfully used in a recent experiment performed at the INFN-LNL EXOTIC facility, Padova, with an incident ^{8}B beam near barrier energies (E_L=25-40 MeV) on a three stage Si telescope. The nature of the unstable beam nucleus, which decays in ^{8}Be and consequently in two alphas, necessitates the usage of appropriate pileup rejection techniques. The proposed offline algorithmic approach has efficiently identified all the recorded pileup events and in most cases has successfully reconstructed the energy information of the overlapping signals. Details of the applied technique with energy reconstruction examples for normal and pileup events are discussed in the present work.

Keywords: `Fast Digitization`, Flash ADC, `Pulse Shape Analysis`, `PileUp Event Reconstruction`

[1]e-mail:stiliaris@phys.uoa.gr

1. Introduction

Digital pulse processing has replaced nowadays the traditional shaping and timing circuitry with mathematical routines operating on digitized waveform signals. Pulse Shape Analysis techniques allow the implementation of sophisticated algorithms with substantially more information to be extracted from a measured pulse than is possible with a traditional analog system. These techniques have been recently also applied for the identification of pileup events in Nuclear Spectroscopy with silicon detectors [1]. The main goal of the present study is to explore the possibilities of applying Pulse Shape Analysis techniques not only for the identification but also for the energy and time reconstruction of pileup events. A method is developed for the extraction of the energy information of time overlapping signals in a three stage Si-telescope used in nuclear reactions with unstable radioactive beams.

2. Experimental Setup and Data Acquisition System

In a recently performed measurement of the ^{8}B+^{28}Si total reaction cross section at energies near the Coulomb barrier (E_L=25-40 MeV) [2], an incident ^{8}B beam was produced at the EXOTIC facility [3], at LNL (Laboratori Nationali di Legnaro) INFN/Padova, Italy. The ^{8}B beam needed for this experiment was delivered as a secondary beam product by means of the reaction ^{3}He(^{6}Li,^{8}B)n of a primary ^{6}Li^{3+} beam on a ^{3}He gas target. Although the secondary ^{8}B beam was purity optimized, ^{7}Be, ^{6}Li and ^{3}He contaminants were present in the extracted beam as non-filtered byproducts of transfer and elastic processes of the primary beam.

The extracted beam was directed through two Parallel Plate Avalanche Counters ($PPAC_A$ and $PPAC_B$) before hitting a three stage Si telescope placed at zero degrees inside the scattering chamber (Figure 1). This telescope comprises of three Si layers (S1, S2, S3) with ΔE_1=45μm, ΔE_2=45μm and E_3=2000μm and acts simultaneously as active target and detector.

Position information inside the PPACs, as well as Time of Flight (TOF) signals between both PPACs and target, were recorded. These signals are primarily used to discriminate the different species of the incident beam and to calculate the spot size at

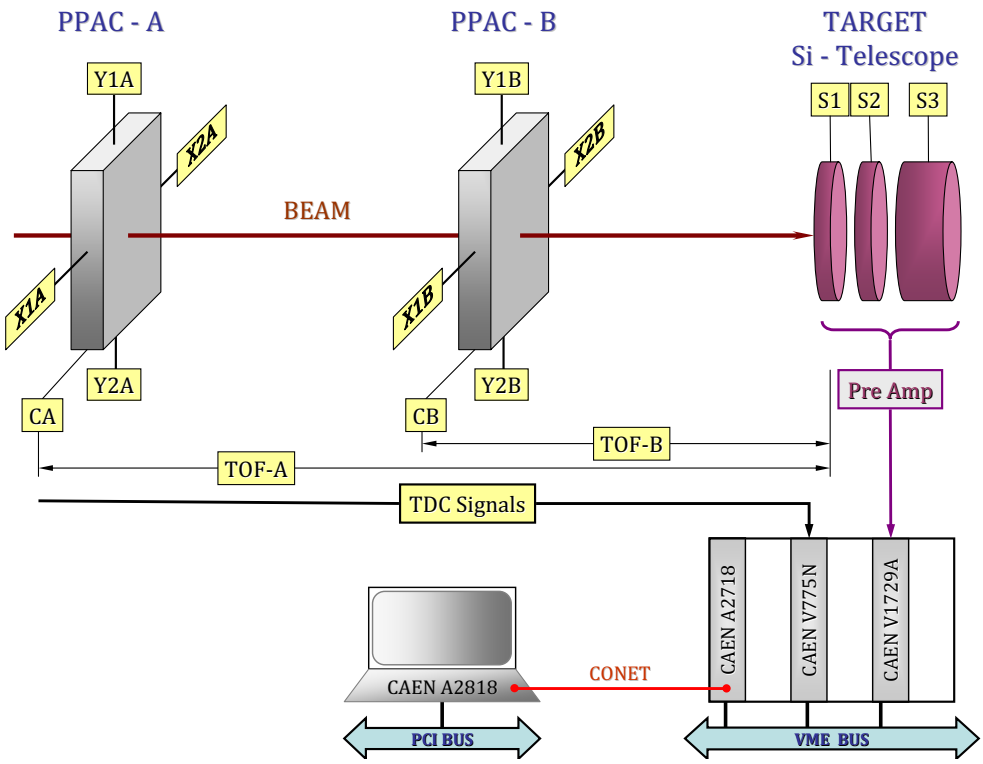

Figure 1: The DAQ-subsystem developed for the ^{8}B+^{28}Si experiment. It was integrated on a separate VME crate using the CAEN A2818/V2718 PCI$\Longleftrightarrow$VME controller kit with the CONET optical fiber link. All timing signals are digitized in the CAEN V775N board, while the Si telescope signals, after pre-amplification, are waveform recorded within the flash ADC V1729A module.

target distances. The energy information is separately read out for each stage of the Si telescope using home-made preamplifiers. The event trigger of the main Data Acquisition system required a coincidence of the type PPAC$_A\otimes$PPAC$_B\otimes$(S1$\vee$S2$\vee$S3).

In this experiment, the nature of the unstable ^{8}B beam nucleus, which beta-decays (T$_{1/2}$=750 ms) into ^{8}Be and consequently in two alphas, necessitates the usage of appropriate pileup rejection techniques. Various conventional pileup rejection techniques based also on home-made electronics were proposed [2] and they have been successfully applied during this experiment. In an alternative approach, a decision has been made to record the Si-detector signals via a waveform digitizer. This option potentially gives a promising solution not only to the identification of possible pileup events, but also to

the successful reconstruction of the underlying energy information.

For this purpose, the CAEN flash ADC module V1729A [4] was used and the recorded waveforms were offline analyzed to resolve time overlapping signals. In this context, an additional DAQ-subsystem based on VME electronics, which run parallel to the main system and synchronized with the master DAQ-trigger signal has been developed (Figure 1).

This DAQ-subsystem has been integrated and tested on a separate VME crate using the CAEN V2718 master module which is controlled by a standard PC equipped with the PCI controller card A2818 via an optical fiber link. The V2718 board can operate as VME System Controller acting in our case as VME bus Requester. The low level control routines and the main core of a simple event builder interface are realized in a Linux environment. The CONET (Chainable Optical NETwork) link guarantees a transfer data rate of at least 70 MByte/s.

3. Pulse Shape Analysis

The main purpose of this work was the development of an offline analysis algorithm which could reliably evaluate all the recorded events and perform the following two distinct tasks:

- Safely identify a PileUp event
- In the presence of a PileUp event possibly extract the energy and time information

Based on the time characteristics of the transition signal for each Si detector and the signal quality improvement after the noise removal, a search algorithm for pileup events has been developed on the basis of applying Pulse Shape Analysis (PSA) techniques.

The algorithm is mainly based on the time differentiation of the obtained waveforms. A simple time differentiation applied to the recorded waveform yields to a peak structure. For a normal non-pileup event, as shown in the upper part of Figure 2, this peak structure reveals certain characteristics, having the form of a gaussian shaped line with an unchanging width for a given type of a silicon detector. The energy information E can be easily extracted by performing a linear fit at both ends of the time window (baselines)

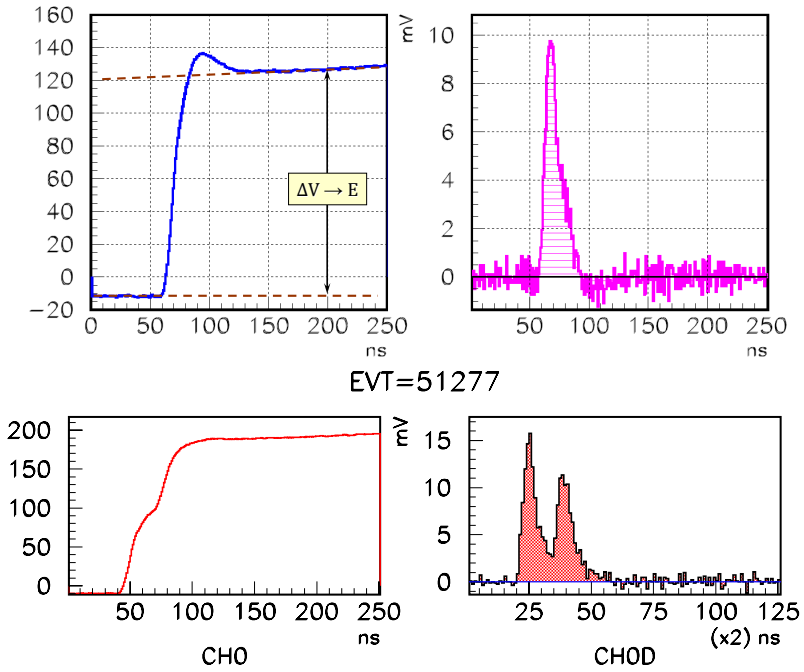

Figure 2: Pulse Shape Analysis: Energy calculation from a single, non-PileUp event (upper part) and a typical PileUp event (lower part) based on the time differentiation of the obtained waveform. The well separable area of the double-peak structure in the PileUp case allows the exact energy determination for each of the overlapping signals (Run: b8-run2-1 Evt: 51277).

of the signal and obtaining the mean values S_1 and S_2 respectively:

$$E = \Delta V = S_2 - S_1 \tag{1}$$

Equivalently, for the time differentiated waveform (derivative), the energy information can be calculated by summing up all accumulated signal changes:

$$E = \int \frac{dS}{dt} dt \tag{2}$$

In the case of a pileup occurrence, the signal time differentiation leads to a double-peak structure, as shown in the lower part of the Figure 2. According to the previous equations, in case the double-peak structure is well separated, the energy information can be again extracted by integrating each of the peak structures. Alternatively, a two-gauss line fit can be performed to the differentiated signal and the resulting area and peak location can be used to calculate the energy and time information [5].

4. Energy Correction from PileUp Events

Based on the previously described Pulse Shape Analysis techniques, an automatic search procedure has been developed, which detects pileup events and if possible, reconstructs the energy information of the overlapping signals. A gaussian line fit procedure has been implemented in this algorithmic approach. The occurrence of a pileup event is signalized by the existence of a double-peak structure in the time differentiated waveform. In the case of a non-pileup event, the energy is normally reconstructed following

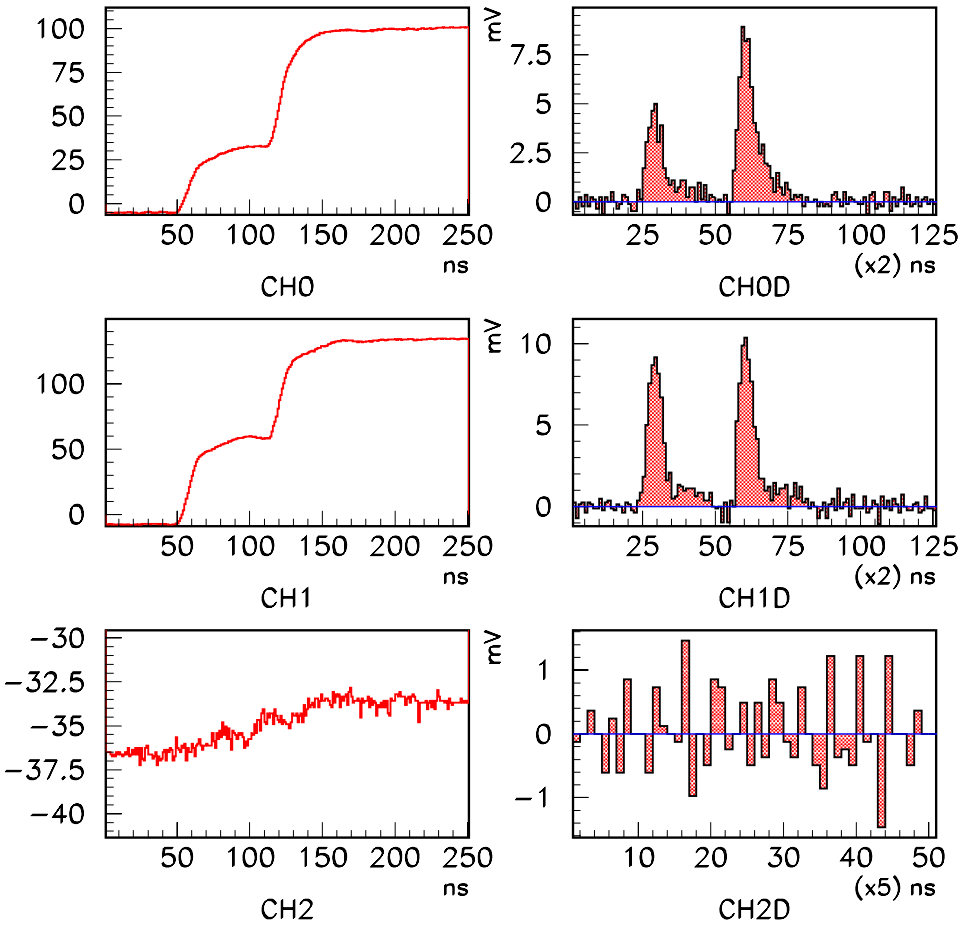

Figure 3: An identified PileUp event (Run: b8-run1-2 Evt: 103613) with a resolvable energy trace in both S1 and S2 detector stages.

the baseline fit procedure (Equation 1). The extraction of the energy information for a

pileup event and for a well separate two-peak structure is achieved by integrating the peak areas of the time differentiated signal (Equation 2). Only in the case of a strong time overlap the resulting parameters of the gauss-line fit procedure are used to determine the corresponding areas.

The performance of the developed algorithm with respect to its ability to successfully extract the pileup energy information for each particle is measured to be ∼95% for all analyzed events in the current experiment. Basic limiting factors are the time difference between the two particles in a pileup occurrence and their relative amplitudes. A 4 ns time limit in the particle separation for the first stages of the Si telescope used here is estimated.

Obtained results for the total number of identified pileup events have been compared and verified on a statistical basis with the various electronic rejection techniques applied in this experiment and recorded with the main DAQ system. Both data analysis processes show a reasonable agreement in the statistics of the obtained pileup events for the different beam energies.

5. Summary

A automatic search technique has been developed for the identification and the energy reconstruction of pileup events in a Si telescope. The procedure is based on Pulse Shape Analysis techniques and utilizes the waveform information by time differentiating the digitized pulse signals. It has been successfully applied in a recent experiment studying the ^{8}B+^{28}Si reaction at beam energies near the Coulomb barrier, where, due to the nature of the unstable beam nucleus, a relative high rate of pileup events is expected. The algorithm has identified all pileup events and with an efficiency of ∼80% successfully reconstructed the overlapping energy and time information. The validity of the developed algorithm for obtaining the energy information from the recorded waveform signals has been checked and verified with conventional methods; isotope identification plots and energy spectra are well reproduced for all measured energies.

References

[1] S.N. Liddick, I.G. Darby and R.K. Grzywacz: Algorithms for Pulse Shape Analysis using Silicon Detectors, Nuclear Instruments and Methods **A 669** (2012) 70–78.

[2] A. Pakou *et al.*: ^{8}B+^{28}Si Total Reaction Cross Sections at Near Barrier Energies, Proposal to the PAC Committee, INFN-LNL Padova, February 2011.
A. Pakou *et al.*: Fusion Cross Sections of ^{8}B+^{28}Si at Near Barrier Energies, Phys. Rev. C **87** (2013) 014619.

[3] F. Farinon *et al.*: Commissioning of the EXOTIC Beam Line, Nuclear Instruments and Methods **B 266** (2008) 4097–4102.

[4] CAEN Module V1729A, A 4-Channel / 14-bit Sampling ADC, Technical Information Manual, Rev. 3, 26 February 2010, http://www.caen.it/csite/CaenProd.jsp?parent=11&idmod=593.

[5] E. Stiliaris *et al.*: Energy Reconstruction from PileUp Events, IEEE NSS/MIC Record **N14-113** (2012) 1092–1097.

REC3D: An Accumulative Reconstruction Algorithm based on Volume Intersectional Information for PET

M. Zioga, A. Nikopoulou, M. Mikeli, A.-N. Rapsomanikis and E. Stiliaris

National & Kapodistrian University of Athens, Department of Physics, 15771 Athens, Greece
Institute of Accelerating Systems & Applications, 10024 Athens, Greece
and the Hellenic Institute of Nuclear Physics (HINP)

Abstract

A new PET image reconstruction algorithm from raw data, based on analytical geometry relations and without *a priori* image information, is presented in the current study. The REC3D algorithm transforms the difficult mathematical problem of the PET image reconstruction in a simple geometrical one. The developed technique utilizes the accumulated ray density distribution in a predefined voxelized volume with appropriate dimensions which covers a given field of interest. The density distribution is the accumulation product of a geometrically weighted intersection of the annihilation line, as it is defined by the detected position of the two anti-diametrically emitted annihilation photons, with all the affected voxels. The final 3D tomographic image is created by properly interpreting the voxel slices of the predefined volume. The algorithm is computationally optimized using an acceleration method, which scans only the affected voxels along the Line of Interest (LoR) in a continuous way. Following this technique for each pair of the detected annihilation photons, the computational time is reduced significantly. The efficiency of this method is evaluated with several phantoms simulated inside the GEANT4/GATE environment and the reconstruction results are compared with other widely used analytical and iterative algorithms.

Keywords: `PET`, `Image Reconstruction`, `GEANT4/GATE`

[1]e-mail:mzioga@phys.uoa.gr

1. Introduction

The Positron Emission Tomography (PET) imaging technique is used in diagnosis and biomedical research. It has proved to be particularly useful for studying brain and heart functions and certain biochemical processes involving these organs (e.g., glucose metabolism and oxygen uptake). A chemical compound in PET, which is called radiotracer, labeled with a short-lived positron-emitting radionuclide of Carbon, Oxygen, Nitrogen or Fluorine is injected into the patients body. PET scanners collect data from the radiotracer distribution. Iterative PET image reconstruction algorithms can achieve superior image quality when compared with conventional analytic reconstruction methods, which usually assume very simple models and present streak artifacts [1],[2]. However, iterative algorithms require optimization techniques and computational times for fully 3D reconstruction which can limit the practical use of these algorithms. Consequently, in recent years many techniques have been proposed to reduce the complexity and number of iterations required for effective convergence [3],[4].

The motivation behind the present work is the development of a new PET reconstruction algorithm. The REC3D uses raw data information and unlike other commonly used algorithms does not require an *a priori* image assumption or a tremendous number of data; REC3D is also not bound or restricted by any PET scanner geometry. This novel algorithm transforms the difficult mathematical reconstruction problem to a pure geometrical one. The developed technique utilizes the accumulated density distribution in a predefined voxelized volume with the appropriate dimensions which covers the field of interest.

2. The REC3D Reconstruction Algorithm

All PET scanners can provide raw data for the position of two anti-diametrically and simultaneously detected photons. With this information, the interior of the detector Field of View (FoV) is a big volume divided in N_x, N_y, N_z cubic voxels along the X, Y and Z axis respectively. The Line of Interest (LoR) of every event will intersect some of these cubic voxels. The reconstruction problem basically becomes an intersection procedure of a given line with a voxel. This problem can be further simplified by the definition that

every voxel consists of six planes. Immediately the geometrical problem is converted to an even simpler one, the intersection of a line with a plane.

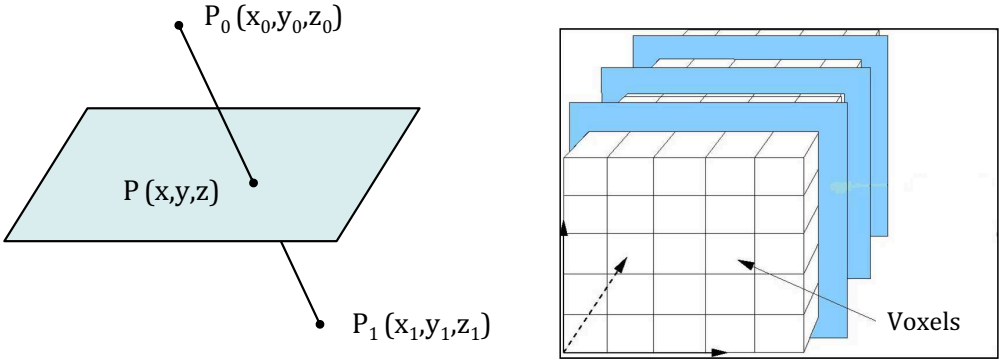

Figure 1: Intersection of the annihilation line with a plane and the definition of the volume of interest

The annihilation line is primarily defined by the two opposite 511 keV photons, detected at the points $P_0(x_0, y_0, z_0)$ and $P_1(x_1, y_1, z_1)$ respectively. The line intersects a given plane at the point P(x,y,z), which is given by the analytical equation:

$$\frac{x - x_0}{x_1 - x_0} = \frac{y - y_0}{y_1 - y_0} = \frac{z - z_0}{z_1 - z_0} \tag{1}$$

For a given plane vertical to one of the system axis X, Y, Z, one of the fractions is arithmetically defined and therefore the full coordinates of the intersection point P(x,y,z) are calculable. For example, for the vertical plane to axis Z at the point $\mathcal{Z}$, its intersection point with the line P_1P_2 is given by:

$$P = \left[\frac{\mathcal{Z} - z_0}{z_1 - z_0}(x_1 - x_0) + x_0 \ , \ \frac{\mathcal{Z} - z_0}{z_1 - z_0}(y_1 - y_0) + y_0 \ , \ \mathcal{Z}\right] \tag{2}$$

The accumulative weight factor, which is used to assign the luminosity distribution in each voxel is the Euclidean distance of the line inside the voxel. The line passes through the voxel from two points $mathcalC_1(u_1, v_1, w_1)$ and $mathcalC_2(u_2, v_2, w_2)$. The Euclidean distance $\mathcal{D}is$ is calculated:

$$\mathcal{D}is = |\mathcal{C}_1 - \mathcal{C}_2| = \sqrt{(u_1 - u_2)^2 + (v_1 - v_2)^2 + (w_1 - w_2)^2} \tag{3}$$

The REC3D algorithm utilizes this technique to scan the whole volume, voxel by voxel, creating the final 3D image.

2.1. Accelerated REC3D

The REC3D algorithm shows the great advantage of minimizing the computation time compared to the other commercially used algorithms. In order to make this advantage even greater an acceleration technique is used. Instead of scanning the whole voxelized volume in order to save computation time and having $\mathcal{D}is$ already known, we take a step further and calculate the first derivatives. This calculation will present a predicted path for the LoR inside the volume. Following the direction of the LoR only the voxels that contribute to the image are scanned.

$$DivX = \frac{C_{1x} - C_{2x}}{\mathcal{D}is} \tag{4}$$

$$DivY = \frac{C_{1y} - C_{2y}}{\mathcal{D}is} \tag{5}$$

$$DivZ = \frac{C_{1z} - Z_{2z}}{\mathcal{D}is} \tag{6}$$

In order to ensure high accuracy a specific step to the calculation of the derivative is introduced. Starting from the intersection points C_{1x}, C_{1y}, C_{1z} and with the given voxel dimensions $X_{step}, Y_{step}, Z_{step}$ an increasing active voxel search along the LoR is computed with the QQ_i points:

$$QQ_{ix} = C_{1x} + i \cdot 0.001 \cdot X_{step} \cdot DivX \tag{7}$$

$$QQ_{iy} = C_{1y} + i \cdot 0.001 \cdot Y_{step} \cdot DivY \tag{8}$$

$$QQ_{iz} = C_{1z} + i \cdot 0.001 \cdot Z_{step} \cdot DivZ \tag{9}$$

The REC3D, as previously remarked, scans the whole volume inside the field of view following the intersection procedure for N^3 computational steps. On the other hand, the total number of steps needed in the accelerated method is reduced to $\sqrt{(N_x)^2 + (N_y)^2 + (N_z)^2}$. The comparison of the two methods gives a factor of

$$\frac{N^3}{N\sqrt{3}} = \frac{N^2}{\sqrt{3}} \tag{10}$$

for the speed improvement of the accelerated method.

3. Simulation in GEANT4/GATE Environment

GATE, the Geant4 Application for Tomographic Emission [5], combines the advantages of the general-purpose Geant4 simulation code and of specific software tool implementations dedicated to emission tomography. GATE takes advantage of the well-validated physics models, of the geometry description, and of the visualization and 3D rendering tools offered by Geant4 but has a distinctive characteristic the modeling of time-dependent processes. The PET detector simulated in this study is a small-Animal

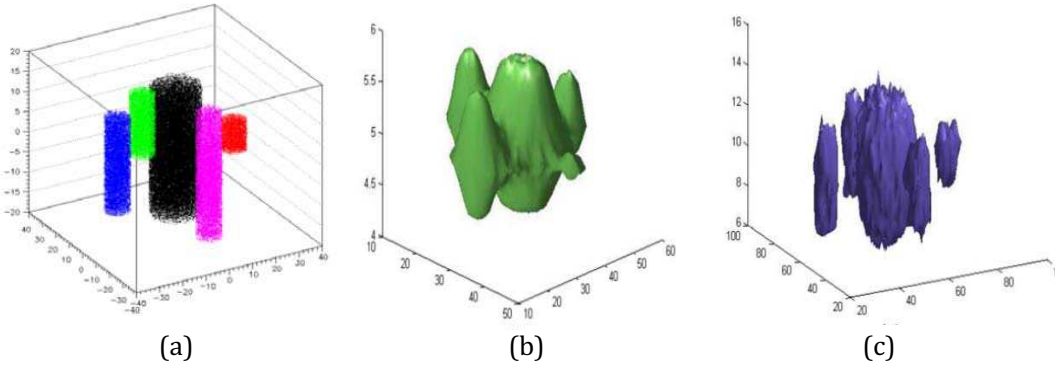

Figure 2: Cylindrical phantom geometry used in the simulation study.

PET scanner called Sherbrooke 16 ring detector [6]. The Sherbrooke Animal PET scanner is a 16-ring camera composed of 256 detectors per ring. It is based on the EG&G C30994 detector module consisting of two BGO scintillators, each coupled individually to a silicon "reachthrough" APD. The detectors are enclosed in an hermetic package of dimensions 3.8 mm x 13.2 mm x 30 mm which determines the channel packing density (4channels/cm^2). The detector modules are physically and logically grouped into cassettes which also incorporate the front-end electronics. Cassettes include 8 modules flayer forming a 2x8 detector array and they can be assembled into "blocks" of several layers. The dimensions and shape of the cassettes are such that they can be used in the construction of various diameter rings without modification. The port diameter is 135 mm, which is suitable for small laboratory animals such as rats, rabbits or the brain of small monkeys. Since each layer of modules consists of two adjacent rings of detectors, three image planes (two direct, one cross) are defined within a 10.5 mm thick transaxial

slice [6].

The phantom used in this study is a asymmetrical phantom that consists of five cylindrical sources of various heights and diameters. In order to be freed from the artifacts created by positron emitting sources, due to the positron mean free path, here two gamma back-to-back sources are used. The cylinders are placed in a cross like formation inside the detector as shown in Figure 2. In more detail the phantom characteristics are shown in Table 1.

Source	Radius	Height	(x,y) Placement	Element	Activity
0	10mm	8cm	(+0.0,+0.0) [cm]	^{18}F	8.0 kBq
1	5mm	2cm	(+2.5,+0.0) [cm]	^{18}F	0.5 kBq
2	5mm	4cm	(+0.0,+2.5) [cm]	^{18}F	1.0 kBq
3	5mm	6cm	(-2.5,+0.0) [cm]	^{18}F	1.5 kBq
4	5mm	8cm	(+0.0,-2.5) [cm]	^{18}F	2.0 kBq

Table 1: Geometry and activity of the 5-cylinder phantom used in the GEANT4/GATE simulation.

4. Results and Discussion

The REC3D results where compered with widely used reconstruction software for PET image reconstruction (Figure 3). For the reconstruction image produced by REC3D

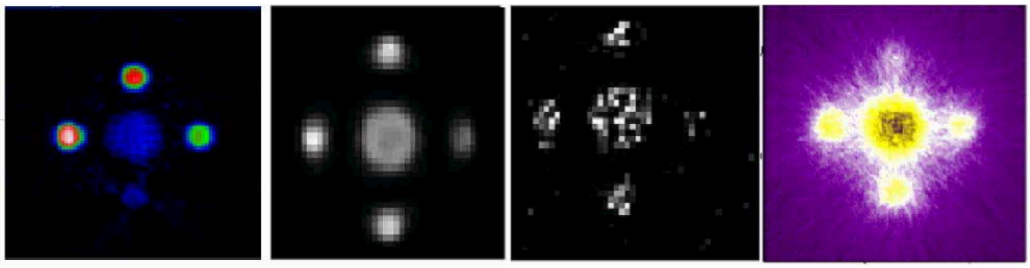

Figure 3: From Left to Right: FBP2D, MLEM, OSEM, REC3D

only 4 981 events where used and its quality is satisfying and superior from the other images. The OSEM algorithm uses 1 404 140 single events and MLEM 1 404 140 as well. The image reconstruction outcome using the FBP2D algorithm needs 4 940 290 events.

The large number of the required events for the other methods is translated to more computation time, which demands more acquisition time and more patient discomfort.

In conclusion it can be noted that REC3D can reconstruct accurately images with fewer data and less computational time. The algorithm can be potentially used in any scanner architecture, regardless the detector's geometrical characteristics. Contrary to the other iterative methods, the REC3D technique is not limited by any data quality restrictions or any kind of data filtering.

References

[1] Charles L. Epstein: *Introduction to the Mathematics of Medical Imaging*, Society for Industrial & Applied Mathematics, 2nd edition (2007) ISBN: 978-0898716429.

[2] Thorsten M. Buzug: *Computed Tomography*, Springer Verlag (2008) ISBN: 978-3540394075.

[3] D.L. Bailey, D.W. Townsend, P.E. Valk, M.M. Maisey (Editors): *Positron Emission Tomography*, Springer Verlag (2003) ISBN: 978-1852337988.

[4] S. Vandenberghe *et al.*: *Iterative Reconstruction Algorithms in Nuclear Medicine*, Computerized Medical Imaging and Graphics **25** (2001) 105–111.

[5] S. Jan *et al.*: *GATE: A Simulation Toolkit for PET and SPECT*, Phys. Med. Biol. **49** (2004) 4543-4561 and OpenGATE Collaboration http://www.opengatecollaboration.org

[6] R. Lecomte *et al.*: *Design and Engineering Aspects of a High Resolution Positron Tomograph for Small Animal Imaging* IEEE Transactions on Nuclear Science **41** (1994) 1446-1552.

Time Resolved Optical Tomographic Imaging: A Simulation Study

A.-N. Rapsomanikis, A. Eleftheriou, M. Mikeli, M. Zioga and E. Stiliaris

National & Kapodistrian University of Athens, Department of Physics, 15771 Athens, Greece
Institute of Accelerating Systems & Applications, 10024 Athens, Greece
and the Hellenic Institute of Nuclear Physics (HINP)

Abstract

Time Resolved Optical Tomographic (TROT) modality is a promising, non invasive, free of extra dosimetric load, yet challenging, diagnostic method in modern Medical Imaging. It could be potentially employed to provide the necessary anatomical information of an area under examination so much as an autonomous, but also as a supportive system to existing techniques such as the Single Photon Emission Computed Tomography (SPECT) and Positron Emission Tomography (PET). The current work focuses on the feasibility of a TROT system by means of a Monte-Carlo study, utilizing light transport software packages for modeling appropriate optical phantoms and the analysis of the obtained spatial-time signals. Due to the highly diffusive nature of the near infrared radiation through tissue environment, commonly related to this type of imaging, proper resolving limits in the form of time-cuts must be applied on the detected rays in order to separate the diffused from the non-scattered photons. The non-scattered time resolved photons, due to the non-divergent nature of their propagation, can provide the accurate planar information which was further analyzed to reconstruct the tomographic images and from them the final 3D image of the optical phantom. Obtained transport simulation results are presented in the current study and the quality of the tomographically reconstructed images with respect to the spatial-time efficiency of the system is further discussed.

Keywords: `Optical Tomography`, `Raytrace Simulation`, `Time of Flight`, `Tomographic Image Reconstruction`

[1]e-mail:anrapso@phys.uoa.gr

1. Introduction

The majority of the commonly used medical imaging modalities nowadays utilizes ionizing radiation which offers satisfactory results regarding the detection of tissue and bone abnormalities on planar but also on a tomographic level. However, most of them provide limited anatomical information of the surrounding area as single units. A more serious drawback is the translation of the ionizing radiation to dose, deposed in the patient with the exception of MRI and Ultrasound Imaging, where the existing clinical devices also present many weaknesses regarding mobility, narrow space and high cost. For all the above reasons, a new non-invasive imaging technique, free of extra dosimetric load and with a good spatial resolution, is proposed here. This is realized with the detection of the few, non-scattered optical photons in the transport of a laser pulsed beam through a diffused medium and with the time selection of the straightforward propagated photons. Ultimate goal of the present work is the operation and feasibility study of a Time Resolving Optical Tomographic (TROT) modality by means of a Monte-Carlo simulation, where the location and the time of flight of each individual photon are simultaneously recorded.

2. Light Transport Through Tissue Environment

The understanding of the time-resolved imaging procedure demands the exact knowledge of the light behaviour inside organic environments. The main disadvantage of an

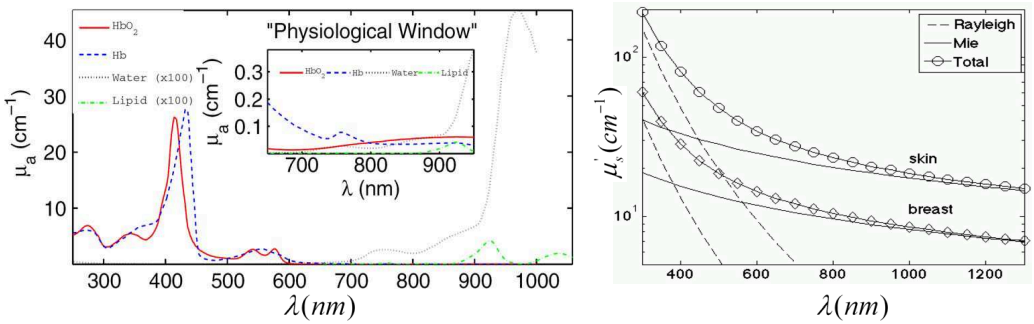

Figure 1: *Left:* Absorption spectra (μ_a is the absorption coefficient) for main tissue elements [1]. *Right:* Scattering spectra (μ_s' is the reduced scattering coefficient) for two different tissue environments [2].

optical imaging system is the highly diffusive nature of the optical rays in any biological tissue and their dominant Rayleigh and Mie scattering processes. While absorption is present for certain wavelengths of the optical and infrared region of the spectrum, an area of frequencies in near-infrared, the so called *"Physiological Window"* [3], makes it minimal and allows a proper region of wavelengths to apply at any optical imaging modality (Fig. 1, upper part). Additionally, as it is shown in the lower part of Fig. 1 this particular "window" also leads to a reduction of the two main scattering mechanisms.

3. Principle of the Time Resolved Imaging

As explained previously, in order to perform an appropriate time-resolved imaging, near-infrared radiation must be utilized as the "probing" light in the form of a narrow time-pulse width, normally in the range fs to ps. The actual duration of the pulse depends on the physical dimensions of the medium under investigation. It is also obvious that the initiated light must be collimated before been able to propagate through a tissue environment. The detected pulse is spread in time due to the physical processes which take place in the organic matter (primarily scattering) and it consists of three main components, shown in Fig. 2:

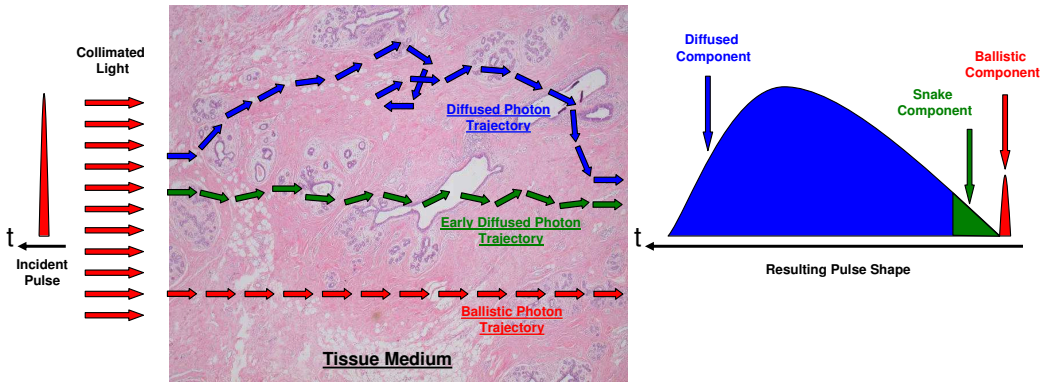

Figure 2: Principle of the Time Resolved Optical Imaging (TROT). With different colors are indicated the three main components. Red: The *Ballistic* component consisting of unscattered photons. Green: The *Snake* component consisting of early arriving diffused photons. Blue: The *Diffused* component consisting of highly scattered photons.

- The *Ballistic* light, composed of early arriving photons (*"image bearing"*). These photons remain unscattered by the environment and they are only an infinitely small fraction of the initiated light.
- The *Snake* component, which incorporates the early arriving diffused photons.
- The *Diffused* component, which dominates the process and mostly consists of highly scattered events.

Hence, if only the ballistic component is to be collected, the anatomical information of the area is revealed. This can be achieved by different time gating techniques, the most important of which are the streak camera and the Kerr-Fourier gate method.

4. TROT Simulation

A Monte-Carlo simulation of a TROT system was performed by means of the DETECT2000 software package [4], a Monte-Carlo simulator developed for studying the

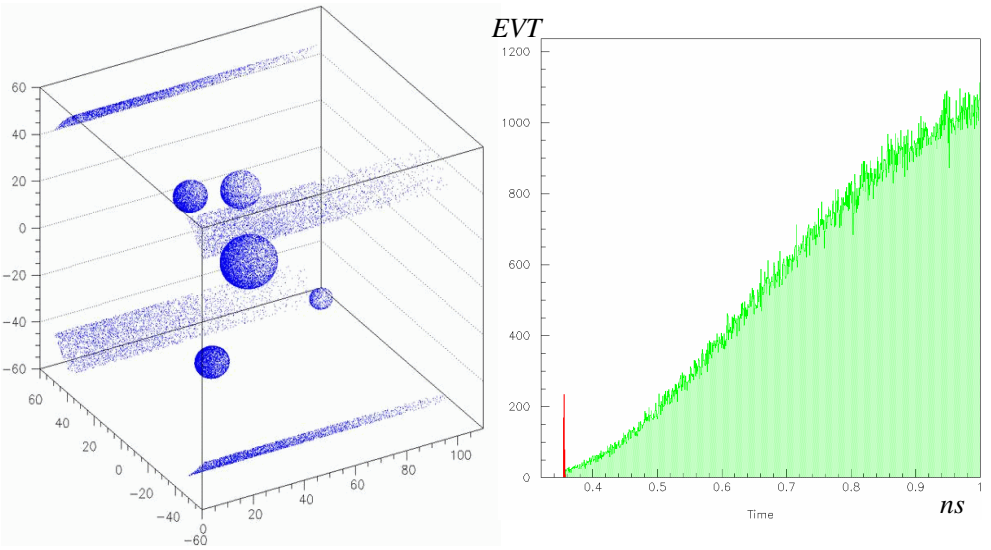

Figure 3: *Left:* The optical phantom consists of five absorbing off-axis spheres of different diameter, in a scattering "blood" cylinder (n=1.33). Each blue point represents an event, where the light is absorbed. The surface of the cylinder, as well as of the spheres, are totaly absorbing. *Right:* The Time of Flight information of the detected photons. With red color is indicated the ballistic component and with green color the diffused light. Time is measured in ns.

propagation of light inside matter. A geometrical optical phantom was designed, consisting of five absorbing spheres of different diameters, placed off-axis in a 100 mm scattering cylinder with n=1.33 refractive index (blood), as shown in the left part of Fig. 3. Then, a narrow photon pulse in the form of a delta function ($\Delta t \sim 0$) from a two-dimensional, plane source covering the phantom's dimensions was initiated through the cylinder and directed towards the detective surface lying on the other cylinder basis.

Since working under the assumption that the near-infrared radiation is utilized, no medium absorption is taken into account. However, the scattering process is being simulated by the software. Consequently, when the photons reach the detection surface after multiple scattering off the "blood" medium they are recorded for further analysis. Each stored photon contains the exact detection location (x,y,z coordinates) and the Time of Flight information (Fig. 3 right). The important for the imaging process Ballistic component is therefore collected by enabling time filtering to the data.

5. Data Acquisition & Analysis

5.1. Time Filtering

Having recorded the Time of Flight of each accumulated event, the planar unfiltered image of the phantom can be *"cleared-out"* revealing all the anatomical information after performing the proper time filtering on each registered ray (Fig. 4).

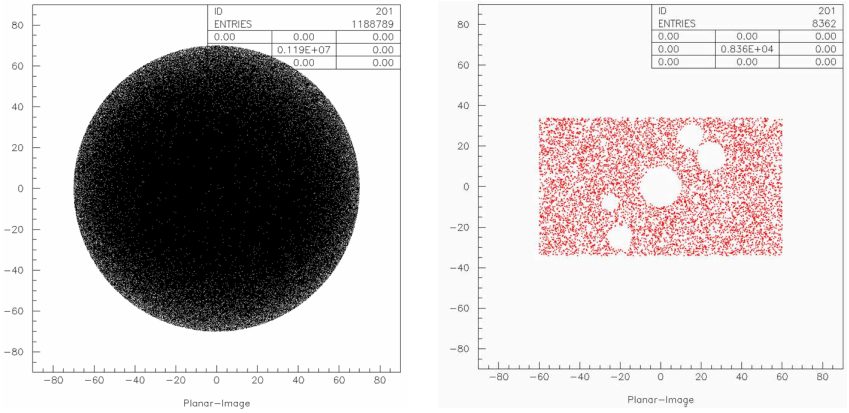

Figure 4: *Left:* The original detected image before performing any time-cut. *Right:* The time resolved image containing the anatomical information of the area under investigation, comprising sole by ballistic photons.

It is clear that the photon statistics drops exponentially with strengthening the time-cuts, until only the depleted ballistic light remains. This creates problems for simulating media with short scattering lengths (average length that each photon travels before scattering) similar to biological tissues. The main obstacle is that the amount of time needed to perform a simulation increases logarithmically and the number of the ballistic events decreases to the point of becoming unmanageable due to their small statistics. However this is something which becomes inessential in a real experiment, since even a pulsed femtosecond LASER can produce packages of billions of photons in a short time period, which can be then properly collected by the previously suggested methods.

5.2. Imaging Capability

The performance of the planar imaging was estimated for a certain sphere profile by taking its projection on the XY-plane. Accumulated photon statistics along one axis of this plane is shown in the upper part of Fig. 5. The efficiency of this method was

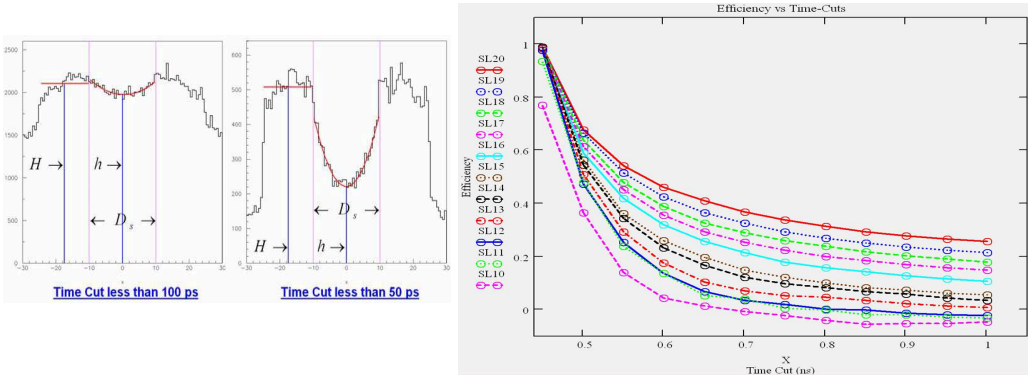

Figure 5: *Left:* Measuring the planar imaging efficiency. H is the average number of events for the X projection of the sphere before any time-cut, h is the average number of events for the X projection at the middle of the sphere after a certain time cut. D_s is the sphere's diameter. *Right:* Optical image efficiency versus time-cuts for different scattering lengths SL (measured in mm).

calculated by the following equation

$$\varepsilon = \frac{H - h}{h}$$

which is a measure for the relative contrast detected for a total absorbing medium. The quantities H and h represent the accumulated photon statistics for the highest illumi-

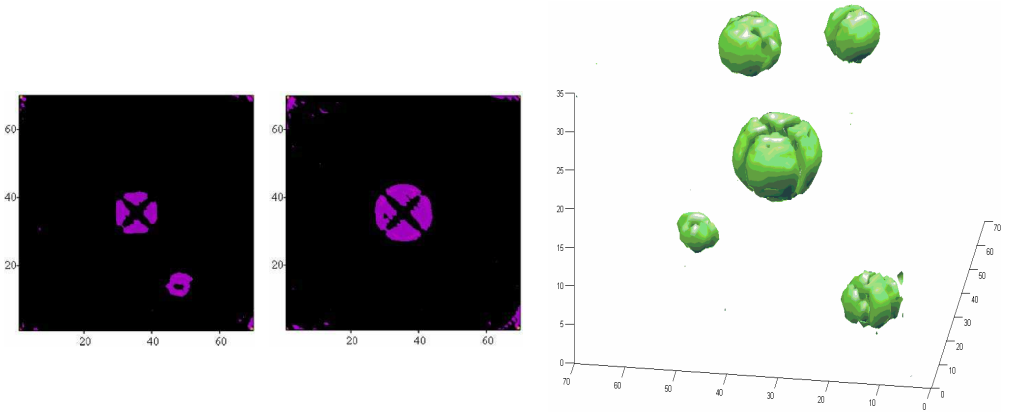

Figure 6: *Left:* Reconstructed tomograms of two different axial levels of the phantom. *Right:* The iso-surfaced 3D reconstruction image of the original phantom, produced by stacking all sliced tomograms

nated and non-illuminated area respectively on the planar image. Different time-cuts were taken into account for a range of various Scattering Lengths (SL). The corresponding results are shown in the lower part of Fig. 5.

5.3. 2D and 3D Reconstruction of the Optical Phantom

A totaly of 24 planar images of the phantom with an angular step of 15^o was simulated, covering the full angle range (0^o-360^o). The obtained results were time-filtered up to the optimal depiction. Then, each projections was axially sliced several times and further analyzed to reconstruct the tomographic images (Fig. 6 left) using iterative reconstruction algorithms developed in our laboratory, which are mainly based on accelerated Algebraic Reconstruction Techniques (ART) [5]. Finally, all the tomograms were iso-surface plotted creating the 3D image of the simulated phantom (Fig. 6 right).

6. Conclusions and Future Plans

In this feasibility study an optical system was simulated with the DETECT2000 program taking into account the scattering processes. Projection images which can be efficiently cleared-out by reducing the "noise" crated by the divergent photons were recovered. Although this filtering process was performed at the expense of the accumulated photon statistics, especially to the ballistic component, the photon statistics was sufficient to successfully reconstruct the input 3D geometrical phantom. The obtained small

photon statistics in the simulation can be bypassed in the actual experiment by utilizing very narrow LASER pulses.

Future plans include the evaluation of the TROT principle of operation with a fast photomultiplier tube or with a Kerr-Fourier gate apparatus. The final goal is to optimally design and implement an Optical Tomographic System combined with the existing γ-Camera prototype developed in our laboratory [6]. This Dual-Modality SPECT/TROT system will be tested and comparatively characterized by utilizing a number of proper complexity phantoms.

References

[1] T. Durduran, R. Choe, W.B. Baker and A.G. Yodh: *"Diffuse Optics for Tissue Monitoring and Tomography"*, Rep. Prog. Phys. **73** (2010) 076701.

[2] S.L. Jacques: *"Optical Properties of Biological Tissues: A Review"*, Phys. Med. Biol. **58** (2013) R37–R61.

[3] F.F. Jöbsis: *"Noninvasive Infrared Monitoring of Cerebral and Myocardial Sufficiency and Circulatory Parameters"*, Science **198** (1977) 1264–1267.

[4] C. Moisan, F. Cayouet and G. McDonald: *"DETECT2000: A Program for Modeling Optical Properties of Scintillators"*, Version 5, Laval University, Quebec, Canada (2000).

[5] S. Angeli and E. Stiliaris: *"An Accelerated Algebraic Reconstruction Technique based on the Newton-Raphson Scheme"*, IEEE Nuclear Science Symposium Conference Record **M09-323** (2009) 3382-3387.

[6] D. Thanasas *et al.*: *"A Correction Method of the Spatial Distortion in Planar Images from γ-Camera System"*, Journal of Instrumentation **4** (2009) P06012.

Interaction of actinides with natural microporous materials: A short presentation of a few recent activities of the Radiochemistry group of the Aristotle University of Thessaloniki

P. Misaelides and F. Noli
Department of Chemistry, Aristotle University of Thessaloniki, 54124 Thessaloniki, Greece

1. The actinides

In the group of the actinides belong the elements with atomic number Z=89 -103 (Fig. 1). All these elements do not possess stable isotopes. Their electronic structure of actinides is not completely known but the gradual filling of their 5f electronic orbitals is characteristic and influences their properties. The 5f electrons of the actinides play a more significant role in their chemical bonding than the 4f electrons of the lanthanides.

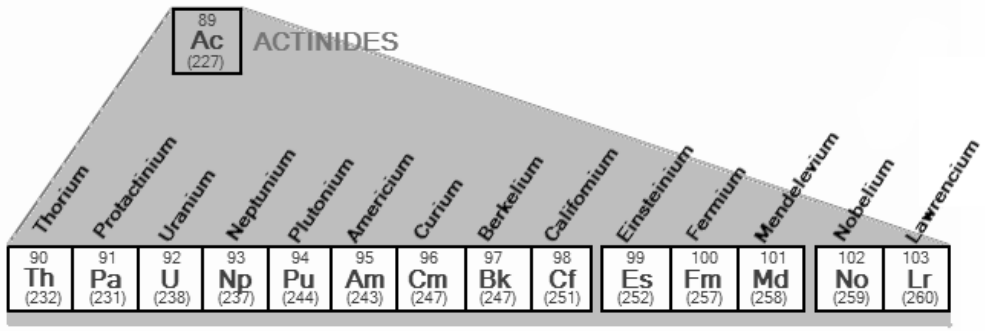

Fig. 1: The actinide elements.

The actinide elements exhibit many oxidation states and show a complex environmental chemistry showing certain analogies with this of the lanthanide elements [1, 2].

In the III and IV oxidation states, the actinides form hydrated actinyl-ions (An^{3+} and An^{4+}) in solutions. In contrast, the highly charged ions in the V and VI states are unstable in aqueous solution and hydrolyze instantly to form linear *trans*-dioxo cations, AnO_2^+ and AnO_2^{2+}.

The actinide ions also show the tendency to form complexes. The hydroxy- and the carbonato-complexes of the actinides are the most common ones because of the overall presence of hydroxyl- and carbonate-ions in the environment [3]. The complexes of the pentavalent actinides are the weakest and the solubility controlling solids. They are the very soluble and therefore the most able to migrate in the environment. Figure 2 shows, as an example, a fraction diagram of the U(VI) aqueous species in solutions of varying pH in equilibrium with CO_2 ($\log P_{CO2}$ = -3.5) for total $(UO_2)^{+2}$ concentration 10.0 mM.

The presence of actinides in the environment is not only due to natural reasons but also to human activities closely related with the production and use of fertilizers, the nuclear and conventional energy production, as well as the development and testing of nuclear weapons [6]. The actinides are

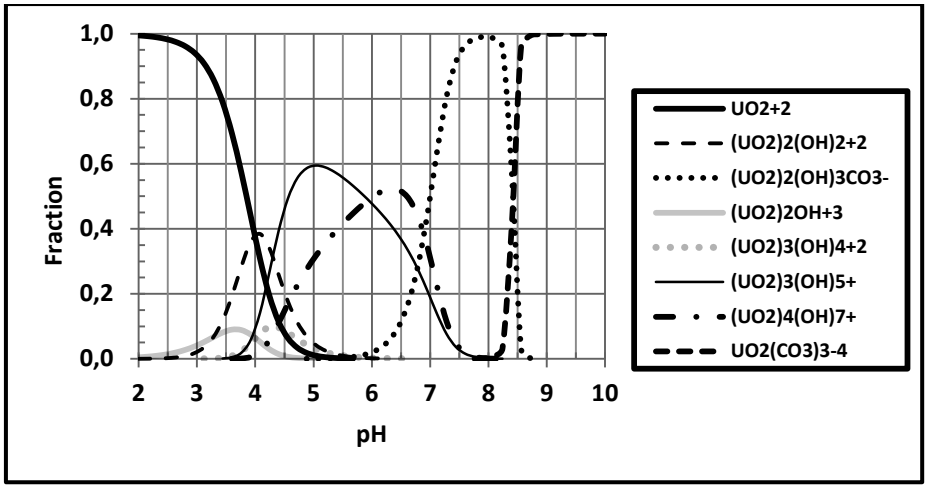

Fig. 2: Fraction diagram of U(VI)-species in aqueous solutions of varying pH in equilibrium with atmospheric CO_2 ($logP_{CO2}$ = -3.5) for total $(UO_2)^{+2}$ concentration 10.0 mM. Only aqueous species are shown in the diagram (The calculations were performed with the computer code MEDUSA using data from the OECD-NEA Thermochemical Database for T = 25 ^oC [4, 5]).

strongly radiotoxic and their involvement in various geochemical and biogeochemical cycles can endanger the human health. Therefore, the investigation of their environmental chemistry and behavior are subjects of extreme scientific and technical interest. The most environmentally important actinides are those directly related with the nuclear energy production (Th, U, Np, Pu, Am, Cm).

The transport of actinides in the biosphere mainly takes place through aquatic pathways and their mobility strongly depends on the geologic environment (site-specific minerals), the temperature and pressure profiles, the pH of the local waters, the redox potential (Eh) and concentration of inorganic (e.g. carbonates) or organic (e.g. humic acids) ligands. The interaction of their dissolved species with sorptive geological materials (e.g. natural zeolites, clay minerals, micas, metal-oxides/ hydroxides/oxyhydroxides) highly influences their migration behavior [2, 7]. Unfortunately, only few studies concerning the geochemical behavior of actinides can be performed in-situ and therefore laboratory experiments are necessary to elucidate their environmental behavior. Laboratory experiments are also necessary in order to evaluate the effectiveness of these materials to act as actinides decontamination agents, as backfill and sealing materials in nuclear repositories and as permeable reactive barriers for cleaning of waters [8, 9]. The chemical processes taking place include sorption through different mechanisms (e.g. adsorption/ surface sorption, absorption/ion exchange, surface precipitation), complexation (mainly with carbonate anions) as well as formation of colloidal- and pseudo-colloidal systems [2].

2. The interaction of actinides with natural microporous materials.

Natural microporous materials include several types of minerals such as zeolites, clay minerals, micas, metal-oxides/hydroxides/oxyhydroxides present in various geological environments and soil formations.

The zeolites are crystalline natural or synthetic alumino-silicates with structure consisting of ordered $[SiO_4]$ and $[AlO_4]$ tetrahedra linked by corner-oxygen sharing. Due to the presence of Al-containing tetrahedra, the zeolites exhibit a negatively charged framework, which is counter-balanced by exchangeable cations. Figure 3 graphically presents the framework, the openings and a

microphotograph of clinoptilolite ($(Na_4,K_4)(Al_8Si_{40}O_{96}).24H_2O$), which is one of the most common zeolites appearing in many parts of the world. The presence of these exchangeable cations also explains its enhanced sorption properties of the zeolites [10, 11]. Some other common natural zeolites finding extensive applications are the heulandite ($Ca_3(Al_8Si_{28}O_{72}).24H_2O$), the chabazite ($(Na_2,Ca)_6(Al_{12}Si_{24}O_{72}).40H_2O$) and phillipsite ($(Na,K)_{10}(Al_{10}Si_{22}O_{64}).20H_2O$) [12,13].

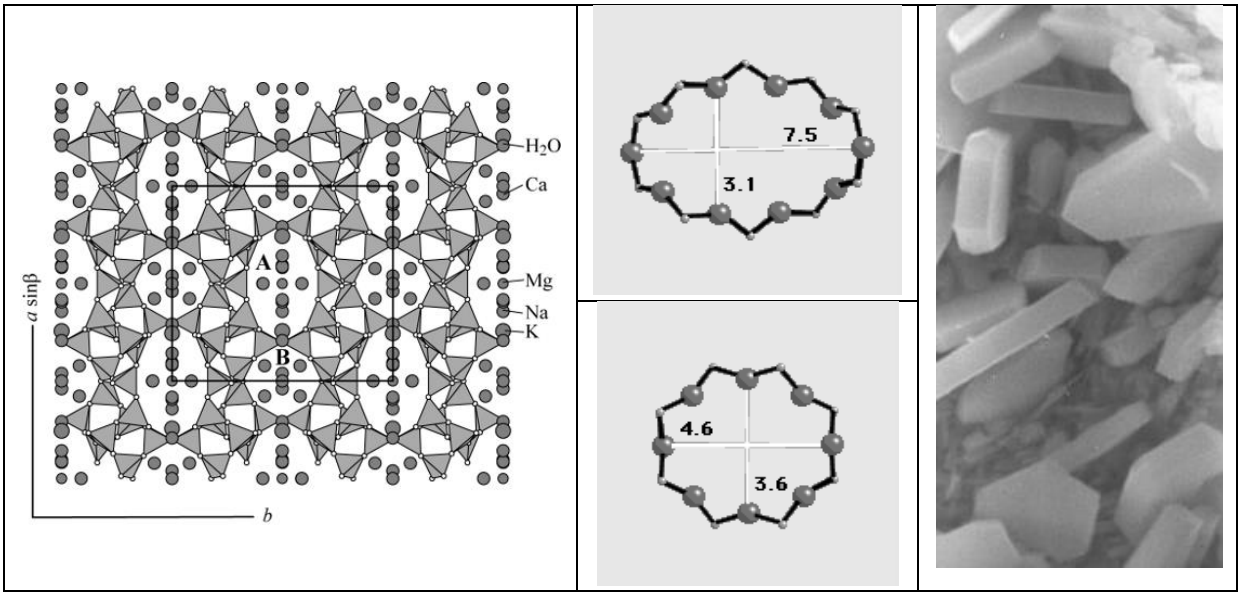

Fig. 3: HEU-type zeolite (clinoptilolite): Graphic presentation of its framework (left), channel dimensions (middle), microscopic crystal appearance (right).

The natural zeolites gained early attention and were utilized for decontamination and nuclear waste treatment purposes. They exhibit high cation sorption capacity and selectivity, enhanced thermal and hydraulic properties and relatively high availability in the nature. The intense investigation of the natural zeolite properties started in the middle of the previous century, when materials with enhanced sorption capacity were necessary for the nuclear waste management. A number of patents on the application of clinoptilolite to the immobilization of radioactive cesium isotopes already appeared around 1960 and there is still enhanced interest in this field [8, 9, 14]. Regions rich in natural zeolites were also proposed as potential nuclear waste repositories [15].

Especially interesting class of materials for the environmental applications is also the surfactant-modified zeolites. These materials, which combine the enhanced cation sorption properties of natural zeolites with the ability to remove anionic species, non-polar organic species and pathogens from aqueous streams, are also considered for applications as decontamination agents for soils and water basins, backfill and sealing materials in waste repositories and as permeable reactive barriers for the cleaning of waters [16]. The most frequently used modifying agents are quaternary amines (e.g. hexadecyl-trimehylammonium (HDTMA), octadecyl-trimethylammonium (ODTMA), N-cetylpyridinium), which form on the zeolite surface a bilayer-like structure altering its surface charge from negative to positive. The positive surface charge provides sites for sorption of anions, whereas the organic-rich surface-layer a partitioning medium for sorption of non-polar organic compounds (Fig. 4).

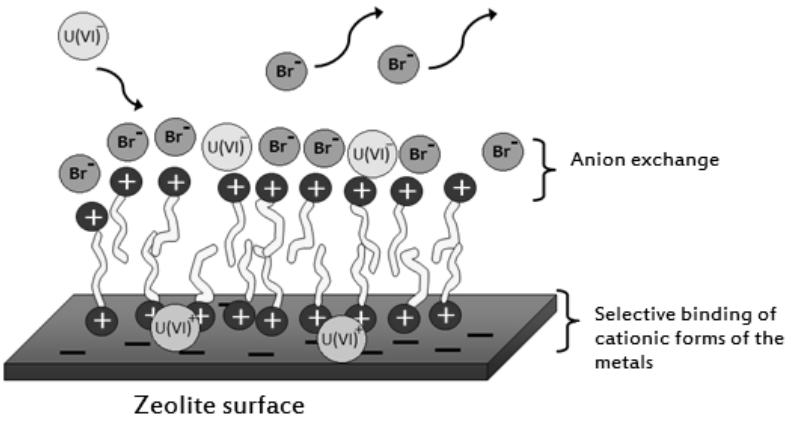

Fig. 4: Schematic presentation of the sorption of hexa-valent uranium cationic- and anionic species by a surfactant-modified zeolite (e.g., by a HDTMABr modified zeolite).

On the other side, the clay minerals are crystalline natural alumino-phylosilicates with structure also consisting of ordered [SiO_4] and [AlO_4] tetrahedra linked by corner-oxygen sharing. Due to presence of Al-containing tetrahedra, the clay minerals also exhibit a negatively charged framework, which is counter-balanced by exchangeable cations (e.g. Na, K, Ca, Mg) (Fig. 5). These exchangeable cations explain the enhanced sorption properties of the clays. The small grain size of the clays does not especially favor their direct use in separation columns regardless of their high cation exchange capacity. However, the raw and swelled clays find, as the zeolites, applications as backfill and sealing materials in underground repositories retarding of the migration of actinides and fission products in the environment as well as to the decontamination of soils and water basins [17, 18].

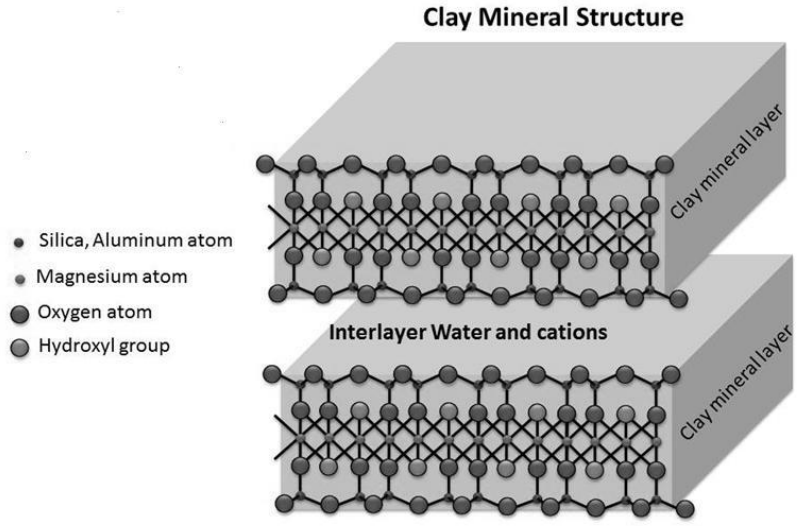

Fig. 5: Schematic presentation of a clay mineral structure.

As expected, the clay minerals can remove only cationic species from solutions but the modification of their surface by quaternary amines can also provide them with the ability to sorb anions.

The micas are a group of sheet silicates (phyllosilicate minerals) including several closely related minerals (e.g. biotite, muscovite, phlogopite, lepidolite) with almost perfect basal cleavage. All of them are monoclinic with a tendency towards pseudo-hexagonal crystals, and have similar chemical composition ($X_2Y_{4-6}Z_8O_{20}(OH,F)_4$, where X: mainly K, Na or Ca, Y: Al, Mg, Fe and Z: Si or Al).

The number of studies concerning the interaction of actinides with metal-oxides/-hydroxides/-oxyhydroxides is rather limited and mainly restricted to Fe- and Mn- containing phases.

2.1 Interaction of actinides with natural zeolites

The literature concerning the interaction of actinides with natural zeolites is not extremely extensive and mainly focuses on the study of elements important to the nuclear waste management (e.g. U, Th, Np, Pu, Am) (Fig. 6). The majority of the works concerns zeolites of the heulandite/clinoptilolite framework type (HEU-type zeolites) because they are the most abundant on the Earth's crust [19]. Crystals of HEU-type zeolites also constitute, along with clays, locations proposed for geological nuclear waste disposal (e.g., Yucca Mountain, Nevada, USA). Especially limited is also the number of works concerning the interaction of actinides with modified zeolites.

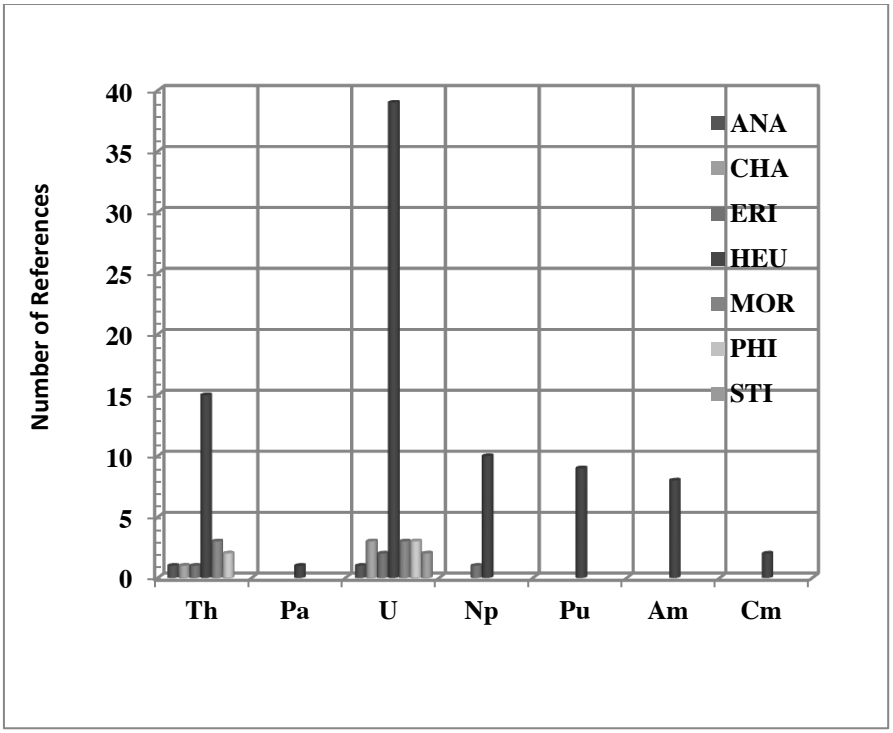

Fig. 6: Number of literature references concerning interactions of the individual natural zeolites with the low-Z actinides (ANA: analcime, CHA: chabazite, ERI: erionite, HEU: heulandite/ clinoptilolite, MOR: mordenite, PHI: phillipsite and STI: stilbite). – Status June 2014.

The investigation of the interactions of raw- and modified natural zeolites (heulandite, clinoptilolite, chabazite, phillipsite, scolecite) under different conditions with low-Z actinides and heavy metals has been one the main activities of the Radiochemical Laboratory of the Chemistry

Department of the Aristotle University in the last twenty years.The techniques applied for this purpose included chemical- and radiochemical methods, optical and electron microscopy and surface (e.g. XPS), and ion beam analysis (mainly RBS and PIXE).

2.1.1 The case of uranium interaction with natural zeolites

Uranium is the most important actinide for the nuclear industry whereas thorium can gain importance in the future. Transmutation and decay of the U-fuels in nuclear reactors generate large amounts of neptunium-, plutonium-, americium- and curium-containing wastes. In the case of direct disposal of the consumed fuels to a repository, the uranium, the rest actinides and the fission products remain together until an eventual failure of both cladding and containment allows their gradual leaching by the groundwater. In the case of fuel reprocessing, the most of uranium and plutonium are separated whereas the long lived fission products and the minor actinides are left in the waste. The mixture is then solidified and disposed in the same way as the intact fuel.

The hexavalent uranium (U(VI)) in acidic solutions (pH < 4) is mainly present in the form of uranyl ion (UO_2^{2+}). The hydrolysis of (UO_2^{+2}) leads to formation of mono- and polynuclear products of the general formula $[(UO_2)_x(OH)_y]^{(2x-y)+}$ (s. Fig.2). The hydrolysis, which starts, depending on the U(VI) concentration, even at pH values below 4, becomes more intense with increasing pH, where also neutral species (e.g. $UO_2(OH)_2^0$) or precipitates ($UO_3.2H_2O$) can be formed. In alkaline aqueous solutions U(VI) forms a number of negatively-charged hydrolysis species (e.g. $[UO_2(OH)_3]^-$ and $[UO_2(OH)_4]^{-2}$), which tend to increase its solubility, availability and mobility. In the presence of CO_2 or CO_3^{-2}-ions uranyl carbonato- (e.g. $UO_2(CO_3)_2^{-2}$, $UO_2(CO_3)_3^{-4}$) and uranyl hydroxy-carbonato (e.g. $(UO_2)_2(CO_3)(OH)_3^{-1}$) complexes are formed [20 - 22]. These complexes are also frequently present in natural waters.

The uranium interaction with zeolites is a complex phenomenon arising from both the aqueous chemistry of the element and the properties of the zeolitic material (e.g. mineralogical and chemical composition, particle size). Among the important factors controlling the uranium uptake are the pH, determining its species available in solution and influencing the surface charge of the sorbent crystals, as well as, its concentration.

The uranium removal from aqueous solutions by philippsite:

The uranium removal from aqueous solutions by philippsite[1] was one of recent studies performed at the Radiochemical Laboratory of Chemistry Department of the Aristotle University [23]. For the experimental work an Italian phillipsite-containing tuff[2] (in both raw and HDTMA-modified form[3]) was contacted for 24 hours with uranium aqueous solutions of various concentrations under different conditions (pH, presence of 0.1 $NaNO_3$ as background electrolyte, temperature). The determination of

[1] Phillipsite (PHI), a secondary mineral of the general chemical formula $(Ca,Na_2,K_2)_3Al_6Si_{10}O_{32}.12H_2O$) frequently occurring in volcanic regions, is crystallized in the monoclinic system. Its framework structure contains 8-membered channels with openings 3.8 x 3.8, 3.0 x 4.3 and 3.2 x 3.3 Å [12,13]. This zeolite can also be found in tuffs associated with other tectosilicate minerals (e.g. zeolites, feldspars, feldspathoids, SiO_2-phases).

[2] Supplied by Italiana Zeoliti S.R.L. under the commercial name PHIL-75 (Mineralogical composition: phillipsite 46%, chabazite 5%, analcime 9%, smectite 10% and 30% phases with no ion- exchange ability.

[3] The HDTMA-form of the tuff was prepared by treating for 24 hours 5 g of raw tuff with 25 mL of a 60 mmol/L HDTMABr solution at 60 °C.

uranium was performed by photometry using Arsenazo-III as complex-forming agent [24]. Figure 7 shows the experimental results obtained using uranium solutions of pre-adjusted pH 3 and 4.

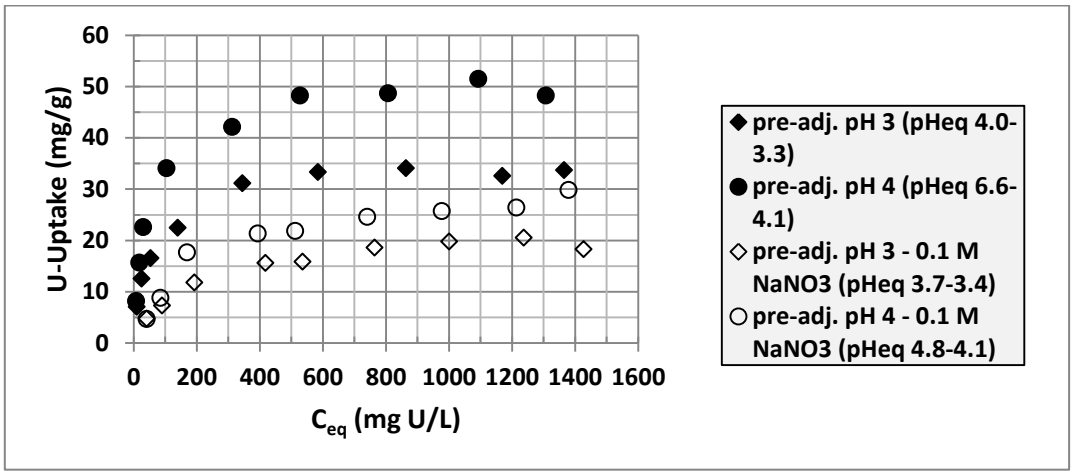

Fig. 7: Equilibrium uranium uptake by the raw phillipsitic tuff in absence and presence of background electrolyte as a function of the equilibrium concentration (C_{eq}) of the solutions [23].

The obtained sorption isotherms could be satisfactorily modelled by the Langmuir equation[4].The maximum uptake capacity values (q_{max}) calculated by fitting the experimental data by the Langmuir equation were 34.8 and 23.5 mg/g for solutions of initial pH (pH_{init}) 3 and 51.3 and 30.6 mg/g of pH_{init} 4 in the absence and presence of background electrolyte.

The U-removal from aqueous solutions of pre-adjusted pH 3 and 4 by the phillipsite-containing tuff could be attributed to different processes unavoidably also connected with simultaneous modification of the sorbent surface (e.g. dealumination, dissolution). However, the rather small dimensions of the phillipsite channel apertures (3.8 x 3.8 (100), 3.0 x 4.3 (010) and 3.2 x 3.3 (010) Å) did not especially favor the entrance of the voluminous uranium-containing ions into the zeolite structure and their ion-exchange. Similar observations were previously also made, using Rutherford Backscattering Spectrometry (RBS), in the case of pure heulandite crystals possessing larger channel openings (7.5 x 3.1 Å) than phillipsite [25]. Figure 8 shows a SEM/EDS microphotograph of a fraction of a phillipsite single crystal after contacting a uranium solution along with the uranium distribution on its surface obtained X-ray mapping using the U M_{a1} X-rays.

The hexadecyl-trimethylammonium (HDTMA)-modified form of the tuff was used to remove uranium anionic species (carbonato-complexes) from alkaline aqueous solutions of pH_{init} 8, 9 and 10. The corresponding q_{max} values obtained by fitting the experimental data by the Langmuir equation were 120.5, 86.2 and 88.5 mg/g for the solutions of pH_{init} 8, 9 and 10 respectively.

The kinetics data obtained for the raw- and HDTMA-modified tuff, using solutions of pH 4 and 8 respectively, at 25, 35, 45 and 55 ^{o}C indicated that the uranium uptake was fast and completed in less than 100 min. The treatment of the kinetics data lead to activation energy for the overall uptake

[4] The Langmuir model $q_{eq} = q_{max} \frac{K_L C_{eq}}{1+K_L C_{eq}}$ assumes a localized monolayer adsorption on a fixed number of adsorption sites of equal energy. K_L is a constant related to the sorption/desorption energy (L/mg), and *qmax* is the maximal uptake upon complete saturation of the sorbent surface (mg/g) [26].

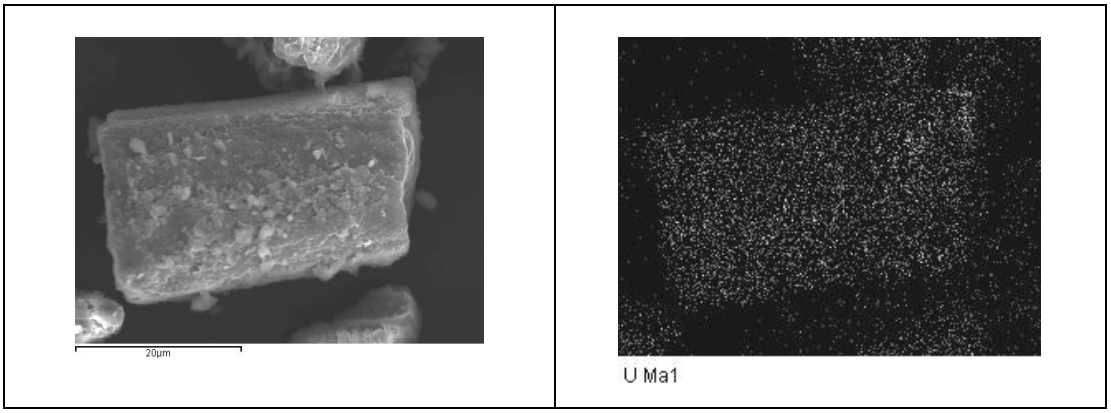

Fig. 8: Phillipsite crystal after interaction with a 1500 mg/L uranium solution of pH_{init} 3 (left) along with the uranium distribution on its surface obtained by EDS (right).

process of 38.44 and 43.37 kJ/mole for the raw and HDTMA-modified tuff respectively. These values are higher than the characteristic range for the physisorption (5-20 kJ/mol) fact that could also eventually be taken as indication of the complex nature of the sorption process.

The obtained results indicated that the investigated raw- and HDTMA-modified phillipsite-bearing tuff could successfully be used for the removal uranium from aqueous streams in the environmental technology.

2.1.2 The cases of interaction of thorium and neptunium anionic species with natural zeolites

The presence of thorium in the environment is not only due to natural reasons but also to a number of human activities including power generation (both nuclear and conventional) and the production and use of phosphate fertilizers. The most stable redox state of Th in aqueous systems is +IV, which shows a strong tendency to hydrolyze above pH 2 forming both mononuclear (e.g., $ThOH^{3+}$, $Th(OH)_2^{2+}$ and $Th(OH)_3^{+}$) and oligomeric species of the general type $Th_x(OH)_y^{(4x-y)}$. The number of hydroxyl ligands depends on the Th concentration and strongly rises with increasing pH. In carbonate containing solutions, Th forms a series of carbonato- and hydroxy-carbonato- complexes of the general type $Th(OH)_y(CO_3)_z^{4-y-2z}$ (e.g. $Th(CO_3)_5^{6-}$, $ThOH(CO_3)_4^{5-}$, $Th(OH)_2(CO_3)_2^{2-}$ and $Th(OH)_4(CO_3)_2^{-}$). The formation of these species is strongly dependent on the pH and carbonate concentration.

The most stable neptunium isotope, the neptunium-237 ($T_{1/2}$: 2.14 million years), is routinely formed in nuclear reactors as a result of the neutron capture by uranium-235 and -238. Neptunium-237 can also be produced by the americium-241 α-decay.

Under sub-oxic and oxidizing redox conditions, neptunium is mainly found in its +V redox state. Due to the low effective charge of the neptunyl-cation (NpO_2^{+}, Z_{eff} ~2.3), Np(V) shows a weak hydrolysis, high solubility and weak sorption. These properties facilitate its mobility in the environment, which can be further enhanced in the presence of carbonate.

The thorium and neptunium behavior in the aquifer systems and their interaction with natural materials are subjects of great interest because of their environmental relevance and possible connection with the far-field in underground repositories for nuclear waste disposal.

The investigation of the thorium and neptunium removal from carbonate-rich aqueous solutions by a greek HDTMA-modified HEU-type zeolite.

The Th-sorption experiments were performed using 9.7 x 10^{-5} M ^{232}Th(IV) in carbonate solutions of 9.0<pH< 10.8 (Na_2CO_3/$NaHCO_3$ buffering; total carbonate concentration 0.25 M). The solid to liquid ratio was 10 g·L^{-1} and the contact time 48 hours. HDTMA-modified heulandite-bearing tuff (HEU-type zeolitic tuff) from Petrota, Greece, containing 89% zeolite, was used for the experimental work [29]. The determination of Th at the end of the contact time was performed by ICP-MS (Perkin Elmer, Elan 6100).

The obtained Th sorption coefficients (R_d = $[Th]_s$ / $[Th]_{aq}$) for the investigated zeolitic material are given in Fig. 9 along with the fraction diagrams calculated for 5<pH<12 and $[CO_3^{2-}]_{tot}$ = 0.25 M and $[Th]_{tot}$ = 10^{-4} M [4, 30]. A very high sorption was observed for the modified tuff at pH 9 where the predominance of highly charged anions ($Th(CO_3)_5^{6-}$ and $ThOH(CO_3)_4^{5-}$) promotes the strong uptake by the HDTMA-modified material. The decrease of R_d with increasing pH values can be explained by the increase of $[CO_3^{2-}]$ in solution and the consequent competition for the sorption sites of the modified tuffs. The increase in sorption observed at pH > 10.5 is attributed to the precipitation of the $Th(OH)_4$(am) solid phase.

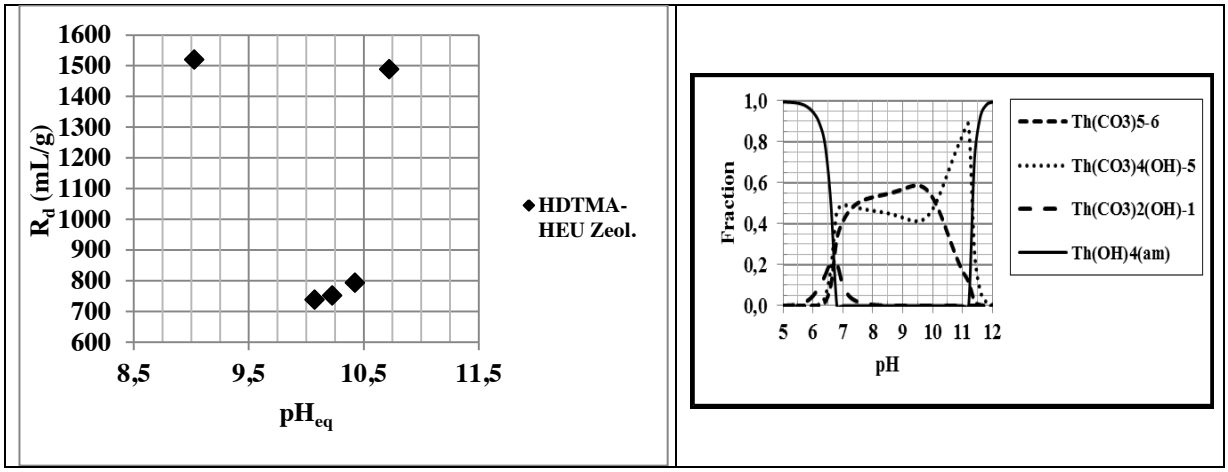

Fig. 9: Left: Sorption coefficients for the Th(IV)-removal from carbonate solutions by the HDTMA-modified HEU-type zeolite tuff (Th conc.: 9.7 10^{-5} M; carbonate conc.: 250 mM). Right: Fraction diagrams of Th calculated for 5<pH<12, $[CO_3^{2-}]_{tot}$ = 0.25 M and $[Th]_{tot}$ = 10^{-4} M. Calculations performed with the computer code MEDUSA using data from the OECD-NEA Thermochemical Database for T = 25 ^{o}C [4, 30].

For the neptunium sorption experiments HDTMA-modified HEU-type zeolitic tuff from Petrota and pulverized pure heulandite crystals from Poona India were used.

The neptunium sorption experiments were performed in a glove-box (inert Ar-atmosphere) using ^{237}Np(V) solutions of 2.6·10^{-5} M concentration. The region of pH 6 -11 was covered by two sets of experiments: the first one using solutions of total carbonate concentration 0.25 M (Na_2CO_3/$NaHCO_3$ buffering) and the other of 3·10^{-4} M (organic buffering by MES, PIPES, HEPES and TRIS). The ^{237}Np concentration in the solutions after 48 hours contact time was determined by liquid scintillation counting (Wallac/ Perkin-Elmer QUANTULUS).

The Np-sorption coefficients ((R_d = $[Np]_s$ / $[Np]_{aq}$)) for the investigated material are given in Fig. 10. A significantly high uptake was observed for the HDTMA-modified HEU-type zeolitic tuff (mod.

HEU-tuff). For both essayed materials, the uptake shows a maximum at pH ~9 and decreases towards hyper-alkaline conditions.

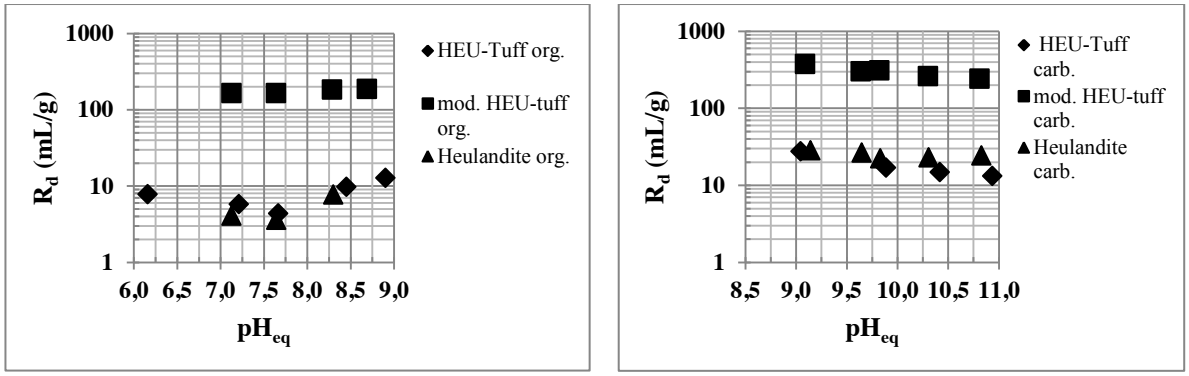

Fig 10: Sorption coefficients for the Np(V)-removal from carbonate solutions (left: $3 \cdot 10^{-4}$ M and right: 0.25 M total carbonate concentration) by raw- and HDTMA-modified HEU-type zeolite containing tuff and pulverized heulandite crystals (org: organic buffering, carb: $Na_2CO_3/NaHCO_3$ buffering).

These observations can be interpreted in relation with the aqueous speciation of Np(V) (Fig. 11) and carbonate within this pH-range. Hence, NpO_2^+ and $NpO_2CO_3^-$ species coexist at $6 \leq pH \leq 9$ and lower carbonate concentrations (organic buffers), whereas highly charged anions prevail at $9 \leq pH \leq 11$ and $[CO_3]_{tot} = 0.25$ M. The latter species are expected to promote a stronger uptake by the modified tuff. Above pH = 9, the fraction of CO_3^{2-} increases (in detriment of HCO_3^-), thus competing with Np(V) species for the sorption sites of the material and consequently decreasing R_d. The total Np(V)-uptake from solutions of high carbonate concentration ($Na_2CO_3/NaHCO_3$-buffered solutions) by the HDTMA-modified tuff varies between 0.24 and 0.35 $mg \cdot g^{-1}$, whereas the corresponding values for the raw tuff between 0.07 and 0.14 $mg \cdot g^{-1}$. These values, although not especially high, represent a significant decrease of neptunium concentration in solution with respect to the upper solubility limit expected for Np(V) in these conditions (oxidizing, high carbonate concentration) and thus confirm the potential of this material for specific environmental applications.

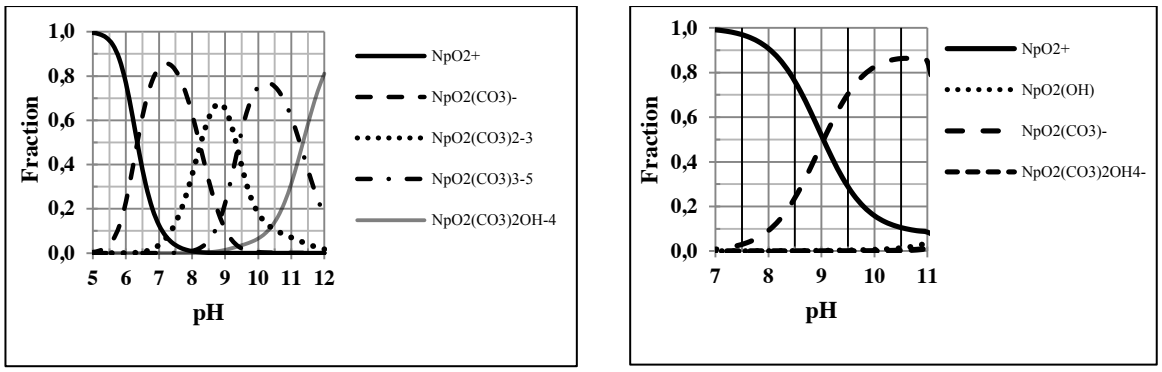

Fig. 11: Fraction diagrams of Np(V)-species in solutions of varying pH in the presence of 0.30 mM (left) and 250 mM (right) carbonate. Total Np(V) concentration: 10 μM. Calculations performed with the computer code MEDUSA using data from the OECD-NEA Thermochemical Database for T = 25 °C [4,5].

2.2 Actinide removal from aqueous solutions raw and HDTMA-modified clay minerals and micas.

The clay minerals, due to their known sorptive properties, were the first natural microporous materials investigated in respect of actinide elements and especially U and Th [14]. A distribution of the works concerning the interaction of the actinide elements with clay minerals is given in Fig. 12. The application of advanced spectroscopic techniques (e.g. EXAFS) considerably contributed to the elucidation of the processes taking place during the clay-actinide interactions whereas high resolution electron microscopy and surface analysis methods (e.g. XPS, AES, SIMS) lead to the conclusion that, besides the ion-exchange, surface precipitation of U-compounds plays an important role in the phenomena observed. These findings are also supported by thermodynamic calculations. As in the case of natural zeolites, the number of studies dealing with modified clays suitable for the removal of anionic actinide species from aqueous streams is very limited.

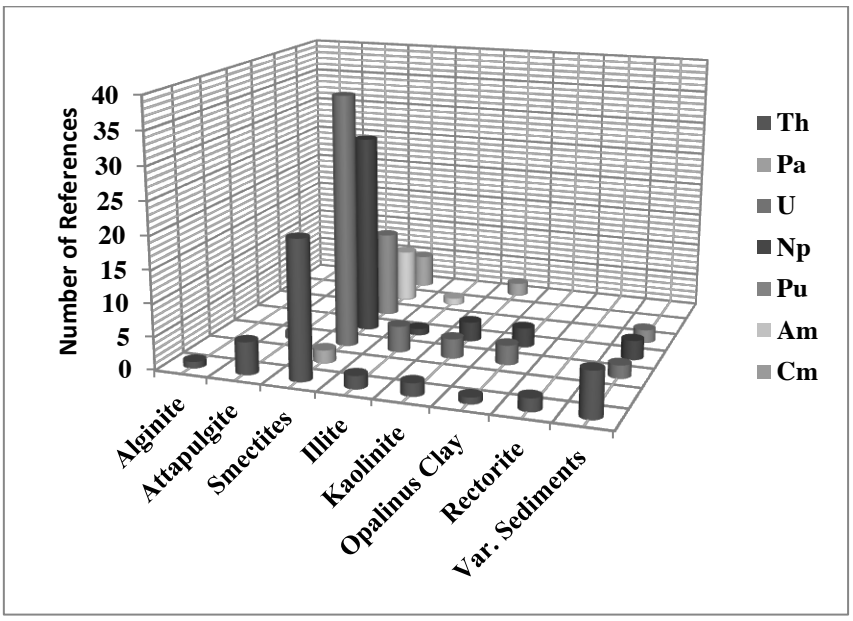

Fig. 8: Number of works concerning the interactions of the individual types of clay minerals with the minor actinides. – Status June 2014

The interaction of uranium with clay minerals with uranium aqueous solutions

Within the frame of the investigations of the interactions of clay minerals with low-Z actinides, we recently studied the interaction of Greek and Slovak bentonites with uranium[5]. Especially interesting for us is the study of the removal of uranyl anionic species from aqueous solutions by surfactant modified (e.g. HDTMA-modified) clay minerals.

For the experimental work bentonites from Kimolos Island (>95% Na-montmorillonite) [31] as well as Slovak bentonites from Jelsovy Potok and Kopernica were used. For the experimental work 50 mg of the raw- or HDTMA-modified materials were contacted for 24 hours with 10 mL of uranium solutions of different concentration. The initial pH (pH_{init}) of the solutions was 3 for the raw materials and 8.5, 9.5 and 10.5 for the modified ones.

[5] Part of the MSc Thesis of the ERASMUS students E. Viglasova and A. Krajnak (Comenius University Bratislava) performed at the Aristotle University of Thessaloniki; not yet published data.

Figure 9 presents the sorption isotherms obtained for the raw Kimolos bentonite for pH_{init} 3 and the HDTMA-modified one for pH_{init} 9.5 and 10.5. The corresponding equilibrium pH (pH_{eq}) after the contact was 3.7- 3.3 and 9.1-8.8 and 10.2 – 10.0 respectively. The experimental data were modelled using the Langmuir, Freundlich, Dubinin-Radushkevich, Tempkin isotherm equations [43]. The best agreement based on the R^2 of the fit was obtained using the Langmuir equation. The calculated maximum uptake capacity (q_{max}) was 54.3 mg U/g for the raw bentonite and 18.1 and 30.8 mgU/g for the HDTMA-modified.

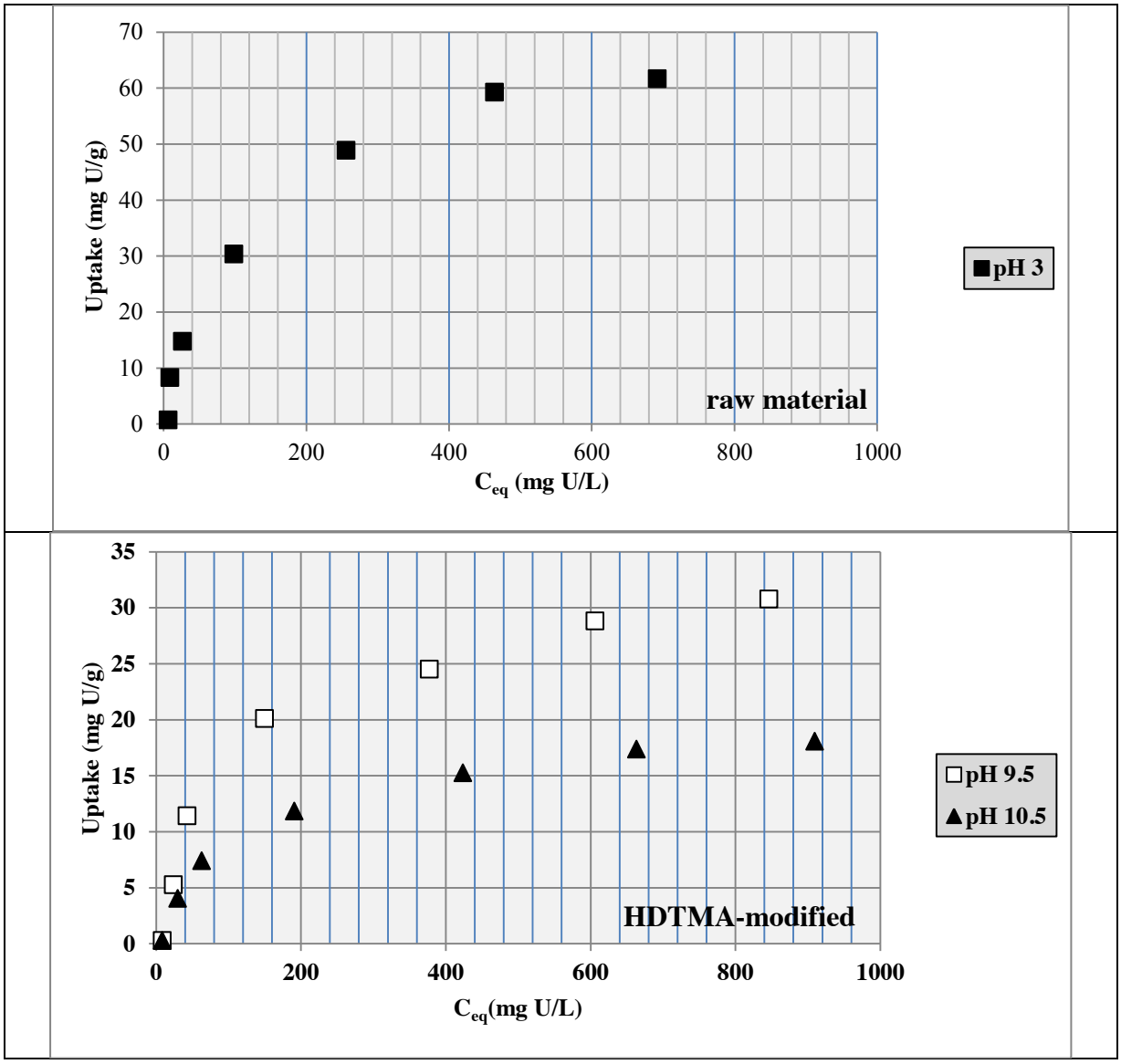

Fig. 9: Uranium uptake isotherm by raw (upper diagram) and HDTMA-modified Kimolos bentonite (lower diagram).

Kinetic measurements performed at 25, 35, 45 and 55 ^{o}C indicated the process, for both the raw and HDTMA-modified material, was rather fast and less than 60 min were required for the achievement of the maximum uptake. On the basis of the kinetic data the thermodynamic parameters (ΔG, ΔH, ΔS) as well the activation energy of the uptake process were calculated.

The interaction of granitic biotite with uranium aqueous solutions.

The consideration to use granite rocks for the storage of nuclear waste increased the number of works dealing with the interaction of micas (biotite, muscovite, phlogopite) with actinide elements. At this point one should mention the considerable contribution of ion beam analysis techniques to the study of micas present in granitic rocks after the interaction with actinide solutions. These studies had as aim the clarification of the sorption processes taking place.

An example from our work is given in Fig. 10 presenting the uranium depth distribution on granitic biotite obtained, after interaction with a uranium solution, by ^{12}C-RBS [32]. The uranium is concentrated on the surface of the biotite crystal. The same figure also gives the uranium uptake by powdered biotite calculated on the basis of neutron activation analysis data. The thorium distribution on the biotite surface, as well as the thorium uptake by the material is given in the same publication.

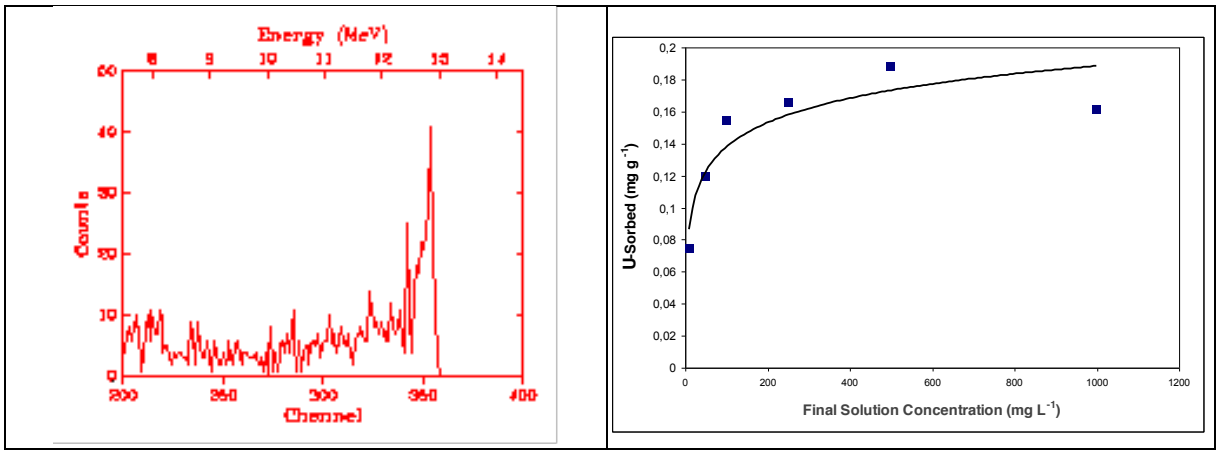

Fig. 10: ^{12}C-RBS of the U-distribution on granitic biotite treated with a uranium solution (left). U-uptake by granitic biotite (right).

2.3 Interaction of actinides with natural metal oxides/hydroxides/oxy-hydroxides.

The rather limited investigations on the interaction of actinides with natural metal oxides/hydroxides/ oxy-hydroxides mainly concern Fe- and Mn-containing phases (e.g. goethite, hematite, romanchite, todorokite) [14, 33, 34].

Although in the past specific activity in the field of interaction natural metal oxides (e.g. MnO_2, todorokite [34]) existed in our Lab., our main recent activity on this subject is restricted to synthetic metal oxides (Fe-, Zn- oxides).

2.4 Conclusions

Despite of the considerable work already performed in the field of interactions of actinide element solutions with natural microporous materials, there is still need for basic data as the emphasis shifts from the production of plutonium for civil and military purposes to nuclear waste management and environmental protection and remediation. Fundamental knowledge about the interaction of actinides with different natural microporous materials under different conditions can considerably contribute to

the understanding their environmental behavior and to development of new strategies for the restriction of their migration in the biosphere.

References

[1] Choppin G.R. (2003). Actinide speciation in the environment, Radiochim. Acta 91: 645–649.

[2] Runde W. (2000) *The Chemical Interactions of Actinides in the Environment*, Los Alamos Science 26: 392-411

[3] Altmaier M. Gaona X. and Fanghänel T. (2013) Recent Advances in Aqueous Actinide Chemistry and Thermodynamics, *Chem. Rev*. 113: 901–943

[4] Puigdomènech I (1983) *INPUT, SED, and PREDOM: Computer programs drawing equilibrium diagrams*, Report TRITA-OOK-3010, Royal Institute of Technology (KTH) Dept Inorg Chemistry, Stockholm.

[5] Guillaumont, R., Fanghänel, Th., Neck, V., Fuger, J., Palmer, D. A., Grenthe, I., Rand, M.H. (2003*). Chemical Thermodynamics, Vol. 5, Update on the Chemical Thermodynamics of Uranium, Neptunium, Plutonium, Americium and Technetium*, OECD, NEA-TDB, Elsevier, North Holland, Amsterdam.

[6] Eisenbud M., Gesell T.F., *Environmental Radioactivity from Natural, Industrial & Military Sources*, 4th Edition, Academic Press, San Diego CA, 1997

[7] Maher K., Bargar J.R., Brown J.E. Jr (2013) Environmental speciation of actinides, Inorg. Chem. 52: 3510-3532

[8] Misaelides P. (2010) Separation of Cesium-137, Strontium-90 and Actinides from Waters and Wastewaters: A Short Review of the Materials and Processes, in: M. Vaclavikova, K. Vitale, G.P. Gallios, and L. Ivanicova, (Eds.), *Water Treatment Technologies for the Removal of High-Toxicity Pollutants*, Springer, Dordrecht, 183–191

[9] Misaelides P. (2011) Application of natural zeolites to the environmental remediation: A short review, Micropor. Mesopor. Mater. 144: 15-18

[10] Dyer A. (1988), *An introduction to zeolite molecular sieves*, John Wiley & Sons, Chichester

[11] Mumpton F.A.(1999), La roca magica: Uses of natural zeolites in agriculture and industry, Proc. Natl. Acad. Sci. USA 96: 3463–3470

[12] Baerlocher C, Olson DH, Meier WM (2001) *Atlas of Zeolite Framework Types*, Elsevier, Amsterdam

[13] IZA (International Zeolite Association) (http://www.iza-structure.org/databases).

[14] Misaelides, P. and Godelitsas, A. (1999). Interaction of actinides with natural microporous materials, In *Natural Microporous Materials in Environmental Technology*, P. Misaelides, F. Macasek, T.J. Pinnavaia and C. Colella (eds), NATO Science Series Vol. E-362, Kluwer Acad. Publ., Dordrecht, pp.193-205

[15] Bish D. L., Vaniman D. T., Chipera S. J. and Carey J. W. (2003) The distribution of zeolites and their effects on the performance of a nuclear waste repository at Yucca Mountain, Nevada, U.S.A., Amer. Mineral. 88: 1889-1904

[16] Bowman, R.S. (2003) Applications of surfactant-modified zeolites to environmental remediation, Micropor. Mesopor. Mater. 61: 43-56

[17] *Use of inorganic sorbents for treatment of liquid radioactive waste and backfill of underground repositories*, Proceedings of a final Research Co-ordination Meeting held in Řež (November 4-8, 1991), International Atomic Energy Agency, Vienna, IAEA-TECDOC-675, pp.189, 1992.

[18] Rajec P., Macasek F. and Misaelides P. (1999) Sorption of heavy metals and radionuclides on zeolites and clays, in: P. Misaelides, F. Macasek, T. J. Pinnavaia and C. Colella (Eds), *Natural*

Microporous Materials in Environmental Technology, Kluwer, Dordrecht, NATO Science Series, Applied Sciences Vol. 362 , pp. 353-363

[19] Godelitsas A. and Armbruster Th (2003) HEU-type zeolites modified by transition elements and lead, Micropor. Mesopor. Mater. 61: 3-24

[20] Moulin C., Laszak I., Moulin V., Tondre C. (1998) Time-resolved laser-induced fluorescence as a unique tool for low-level uranium speciation, Appl. Spectrosc. 52: 528-535

[21] Bargar J.R., Reitmeyer R., Davis J.A. (1999) Spectroscopic confirmation of uranium(VI)-carbonato adsorption complexes on hematite, Envir. Sci. Technol. 33: 2481–2484.

[22] Lehto J., Hou X. (2011) *Chemistry and analysis of radionuclides*,Wiley-VCH, Weinheim

[23] Bampaiti A., Misaelides P., Noli F. (2015) Uranium removal from aqueous solutions using a raw and HDTMA modified phillipsite-bearing tuff, J. Radioanal. Nucl. Chem. (accepted for publication, in press) DOI 10.1007/s10967-014-3796-4

[24] Savvin S.B. (194) Analytical applications of arsenazo III—II: Determination of thorium, uranium, protactinium, neptunium, hafnium and scandium, Talanta 11: 1–6

[25] Misaelides P., Godelitsas A., Kossionidis S., Manos G. (1996), Investigation of chemical processes at mineral surfaces using accelerator-based and surface analytical techniques: heavy metal sorption on zeolite crystals, Nucl. Instrum. Methods Phys. Res., Sect. B 113: 296–299

[26] Gerente C., Lee V.K.C., Le Cloirec P., McKay G. (2007), Application of chitosan for the removal of metals from wastewaters by adsorption - Mechanisms and Models, Crit. Rev. Env. Sci. Technol. 37: 41–127

[27] P. Misaelides, X. Gaona, M. Altmaier and H. Geckeis, Thorium removal from carbonate solutions by HDTMA-modified HEU-type zeolite-, chabazite- and phillipsite-bearing tuffs, Book of Abstracts of the 9th Intern Conf. on the Occurrence, Properties and utilization of Natural zeolites, Belgrade, Serbia, 8-13 June 2014, p.159

[28] P. Misaelides, D. Fellhauer, X. Gaona, M. Altmaier and H. Geckeis, Neptunium removal from carbonate solutions by a greek HDTMA-modified HEU-type zeolite containing tuff, , Book of Abstracts of the 9th Intern Conf. on the Occurrence, Properties and utilization of Natural zeolites, Belgrade, Serbia, 8-13 June 2014, p.157.

[39] Filippidis, A. and Kantiranis, N. (2007), Experimental neutralization of lake and stream waters from N. Greece using domestic HEU-type rich natural zeolitic material. Desalination 213: 47-55

[30] Rand M., Fuger J., Grenthe I, Neck V, Dahnpat R. (2009), *Chemical thermodynamics of thorium*, Vol. 11, OECD, NEA-TDB, http;//www.oecd-nea.org/science/pubs/2007/6254-DB-chemical-thermodyn-11.pdf

[31] Godelitsas A., Gamaletsos P., Roussos-Kotsis M. (2010) Mordenite-bearing tuffs from Prassa quarry, Kimolos island, Greece, Eur. J. Mineral. 22: 797-811

[32] Misaelides P., Godelitsas A., Harissopoulos S. and Anousis A. (2001) Interaction of granitic biotite with selected lanthanides and actinides, J. Radioanal. Nucl. Chem. 247: 325-328

[33] Missana T., García-Gutiérrez M. and Maffiotte C. (2003) Experimental and modeling study of the uranium (VI) sorption on goethite, J. Colloid Interf. Sci. 260: 291-301

[34] Misaelides P., Katranas T., Godelitsas A, Klewe-Nebenius H. and Anousis I. (2002) The chemical behavior of natural microporous manganese oxide todorokite in actinides (Th, U, Pa) aqueous solutions, Sep. Sci. Technol. 37: 1-13

Vertical profile of ^{210}Pb, ^{137}Cs and ^{40}K in Algerian soil samples

M. Nadri, A. Papamichail, M. Antoniou, A. Ioannidou

Aristotle University of Thessaloniki, Physics Department, Nuclear Physics & Elementary Particle Physics Dicvision, 54124 Thessaloniki, Greece

Aabstract.

The depth profiles of ^{210}Pb, ^{137}Cs and ^{40}K concentrations in two types of soil from different areas of Algeria were examined. The soil collection areas are near the location where the French nuclear tests took place at 1960 – 1961. The collection area of sample 1 is rocky with sand while the collection area of sample 2 is porous with stones and sand. The three radionuclides have different rhythm of diffusion and different transfer rate at the two different soils. The diffusion and transport of radionuclides in the two soils are different and depend on the natural soil composition. Sample 1 shows uniformity in the distribution of radionuclides, without a clear maximum (peak), while sample 2 shows a clear peak at 20 – 50 CM depth which is probably due to the different nature of the soil samples. The ^{210}Pb activity values ranged between 27 Bq kg^{-1} and 50 Bq kg^{-1} in sample 1 and between 37 Bq kg^{-1} and 75 Bq kg^{-1} in sample 2. The ^{137}Cs activity values ranged between 0.2 Bq kg^{-1} and 3 Bq kg^{-1} in sample 1 and between 4 Bq kg^{-1} and 6 Bq kg^{-1} in sample 2. And finally the ^{40}K activity values ranged between 75 Bq kg^{-1} and 90 Bq kg^{-1} in sample 1 and between 140 Bq kg^{-1} and 180 Bq kg^{-1} in sample 2. The vertical distribution of sample 2 refers more to the influence of the rate of sedimentation (movement of layers in soil) and less to the vertical diffusion and dispersion of the isotope. The observed activity concentrations of ^{137}Cs are smaller than concentrations observed in Europe. The similar behavior of ^{137}Cs and ^{40}K at both soil samples is probably due to the similar chemical behavior.

1. Introduction

Nuclear explosions consititute the main source of artificial radionuclides that are contributing to the external radiation, since nuclear energy is in use. The main important radioactive contamination of the environment originates from nuclear bombe tests in the atmospher 1945-1991 and accident in nuclear power stations. The degree of contamination is correlate to the intensity of fallout and washout during rainfalls in the period of radioactive cloud passage. (O. El Samad et al.,2007). Over 50 tons of radioactive material escaped and was carried around the world by winds. The radations released was nearly 200 times the total given off the Hirochima And Nakasaki atomic bombs in 1945. (Arthur Beiser, 2003).

In the early 1960s, France conducted a series of above-ground and underground nuclear tests in the south of Algeria at the Reggane and In Ekker sites (Taourirt Tan Affella and AdrarTikertine). These nuclear tests resulted in releases of radioactive material to the environment (Danesi et al., 2008).

Mesurments of ^{137} Cs fallout are of major importance on environmental studies, most of these studies are based on processes related to ^{137} Cs migration in soils, wich is affected of number of factors, such as type

of soil, chemical properties, organic matter content, climatic conditions (such as rainfall, tempreture, or humidity), and biological activity of microorganisms in soil, Cesium undergoes vertical and horizontal migration.whil vertical migration depends on the physicochemical forms of ^{137} Cs, the taype of soils, the hydrological regime and the ecological conditions of the polluted area. Therefor, these two type of migrations and resulting profile distributions differ from area to area and depend strongly on landscape position. Consequently, the relations between ^{137} Cs contents and diffrent parameters have to be determined at each location (M.S. AL-Masri, 2006)

As a consequences of nuclear probes and nuclear accidente (The largest one was Chernobyl at 1986), The ^{137} Cs concentration in surface soil decrease under the influence of various processes like decay, mechanical removing with rain water, vertical migration and diffusion into deeper layers of soil. Several models have been devloped to describe ^{137}Cs migration in soils and explain its vertical distribution (D. Krstic, 2004).

Following the Chernobyle accident on April 26, 1986, a considerable amount of radioactive materials was released into the atmospher contaminating the environment of whole earth. Algeria with its large caost line (1200 Km) facing the European continent was certainly, in north Africa, the country The most exposed to this large scale contamination and might have been affected, to some extent, by the accident (B.Baggoura et al., 1997).

Most of the surface explosions in nuclear tests have released radioactivity to the environment in the form of bulk glassy materials originating from the melting of sandy soil in the neighbourhood of ground zero (F. Belloni et al., 2006). The ^{137}Cs soil vertical distribution, formed many years after a contamination event, can be regarded as an integrating parameter characterizing the resultant vector of prolonged interaction of the aforementioned factors. In turn, vertical distribution of radiocaesium in soil profiles may have a significant influence upon soil-to-plant transfer of the radionuclide, and, therefore, oninternal dose formation (Ehlken and Kirchner, 2002; Ramzaev et al., 2006a).

The activity-depth profiles of ^{137}Cs isotope evaluated by the classical convection-despretion equation and random walk partical model (W. Schimmack, W.Schultz., 2006). For sush an evauation, several mathematical transport models are available (K. Bunzle, 2001).

The main objective of this paper is to present the vertical migration in soil samples of ^{137}Cs, ^{40}K and ^{210}Pb, In Ghardia Region, Algeria.

2. *Materials and methods:*

Soil samples were taken during Summer 2012.Two sites were chosen located near Ghardia city in central Algeria, chacaterized with different soil types, between the atlas mountain and the Sahara desert, sparsely populated, when the main economic activity is ovine and cattle breeding ; This citiy a deset region caracterized by average tempreture in june by 36 ^{0}C and humidity 25.9/.

Soil samples where collected at June 8, 2012. These two sites are Berriane 16 S1 north Ghardia center city about 450 km from Algiers (Algeria Capital) and the second site Zelfana 16 S2 south Ghardia city center about 650 Km from Algiers (Algeria Capital) southern , thes sites located near the National way (N49). Figure1 gives the samples sites map. The samples were taken in rectangular blocks (5*5) CM² up to 70 cm, and cut in to horizontal layer of 2 cm, 5 cm and 10 cm thicknesses respectively. Stones and plant roots were removed before treatment. Soil samples were sifted through the sieve (<200 μm) and prepared for gamma spectrometry. The activity of ^{137}Cs, ^{40}K and ^{210}Pb, in the samples was measured by HPGe All the samples were measured for ^{137}Cs ($E\gamma$=661,65 keV), ^{40}K ($E\gamma$=1460,75 keV) activity using a high resolution (1.9 keV at 1.33 MeV), high-efficiency (42%), low-background HPGe detector and for ^{210}Pb ($E\gamma$= 46:50 keV) using a Ge planar detector with active area 2000mm^2, thickness 20 mm, energy resolution (FWHM) 400 eV at 5.9 keV or 700 eV at 122 keV, Be window 0.5mm thin.

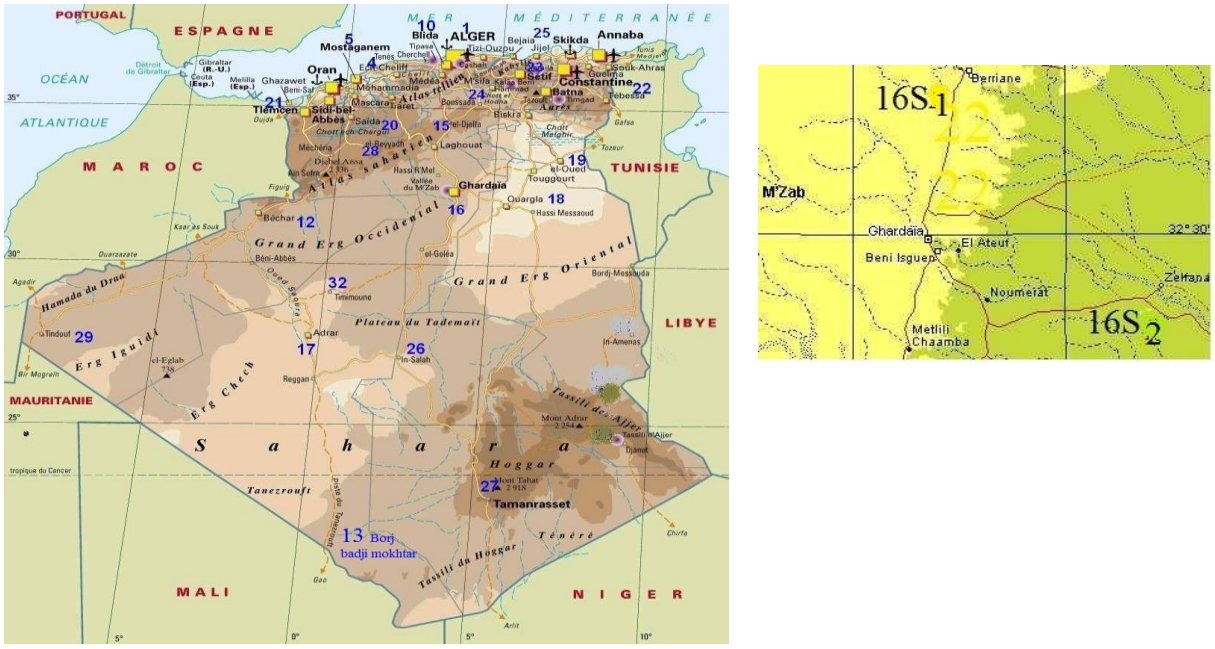

Fig. 1. Ghardia soil Sampling sites;16 S1, 16 S2.

3 **Results and discusions**:

The activity concentrations of radionuclides,^{137}Cs, ^{40}K and ^{210} Pb measured by gamma spectrometry in the analyzed soil samples, collected at two sites of Ghardia City (Algeria) are listed in Tabe1, table 2, and Table 3.

3.1 Vertical profile of ^{137}Cs in soil

The ^{137}Cs activity Distribution for the two sites are shown in the Fig1a. and Fig1b.

The ^{137}Cs concentration at 16S1 range varie between 2.05 Bq.kg^{-1} at 0-5 cm increase to a maximum value 3.03 Bq.kg^{-1} at 30-40 cm and decreased to 0,2 Bq.kg^{-1} at 60-70 cm.The ^{137}Cs concentration at 16S2

between 3.98 Bq.kg^{-1} at 0-5 cm increase to a maximum value 6.09 Bq.kg^{-1} at 20-30 cm and decreased to 4.3 Bq.kg^{-1} at 60-70 cm. The ^{137}Cs activity concentration were lower than the value detected by B.Baggoura et al., (1997) (6-43 Bq.kg^{-})and that reported in UNSCEAR2006.

Table 1., ^{137}Cs vertixal profiles in

16S1				*16S2*		
Depth (CM)	**Smple quantity (Kg)**	**Activity (Bq.kg^{-1})**	**Errors%**	**Smple quantity (Kg)**	**Activity (Bq.kg^{-1})**	**Errors%**
[00-02]	0.081	2.05	3,1	0.078	3,98	3,1
[02-05]	0.081	2.44	3,1	0.080	3,84	3,1
[05-10]	0.081	2.92	3,1	0.077	3,76	3,1
[10-15]	0.082	2.80	3,1	0.077	3,99	3,1
[15-20]	0.078	2,8	3,1	0.076	4,04	3,1
[20-30]	0.084	3,02	3,1	0.073	6,09	3,1
[30-40]	0.085	3,03	3,1	0.071	5,86	3,1
[40-50]	0.085	0,95	3,1	0.077	6,14	3,1
[50-60]	0.088	-	-	0.077	4,35	3,1
[60-70]	0.082	0,22	3,1	0.082	4,3	3,1

3.1 Verticla profile of ^{40}K in soil

Most ^{40} ***K*** in soils is found in minerals. Approximately 95-99% of this ^{40} ***K*** resides in the lattice of silicate minerals such as feldspars and micas (fixed potassium). During weathering, these minerals release potassium ions, which are transferred to soil solutions and adsorbed on the cation exchange sites eg clays. Both solution and exchangeable potassium are considered plant available (Ryoko Fujiyoshi et al., 2004).

The ^{40}K activity distribution for the two sites shown in the Fig1a.And Fig2b.

The ^{40}K concentration at the first site 16S1 increase from 76.92 Bq.kg^{-1} at 0-5 cm to a maximum value 91.56 Bq.kg^{-1}.at 60-90 cm.

The ^{40}K concentration at the secod site 16S2 increase from 138.59 Bq.kg^{-1} at 0-5 cm to a maximum value 183.09 Bq.kg^{-1}.at 20-50 cm. and decreased to 118.19 Bq.kg^{-1} at 60-70 cm.

UNSCEAR 2008	(B.Baggoura et al., 1997).	PRESENT WORK
66 - 1150	93 – 376	76,92 – 183,96

3.3 Verical Profile of ^{210}Pb activity in soil

^{210}Pb , a long-lived radionuclide (T½ = 22,6 y) is produced in the atmosphere near ground level by the decay of its precursor 222Rn (T½ = 3,82 d), an inertnoble gas, which is released from the ground to the atmosphere predominantly from continental surfaces.(A. Ioannidou et al., 2005).

The ^{210} Pb activity Distribution for the two sites shown in the Fig3a.And Fig3b. The ^{210} Pb concentration at the first site 16S1 increase from 45,68 Bq.kg^{-1} at 0-5 cm to a maximum value 49.4 Bq.kg^{-1}.at 20-30 cm. and decreased to 31.21 Bq.kg^{-1} at 60-70 cm.

The ^{210} Pb concentration at the first site 16S2 increase from 55.42 Bq.kg^{-1} at 0-5 cm to a maximum value 75.32 Bq.kg^{-1}.at 20-30 cm. and decreased to 37.11 Bq.kg^{-1} at 60-70 cm.

UNSCEAR 2008	(B.Baggoura et al., 1997).	PRESENT WORK
		26,33 – 74,52

Table 2. ^{40}K:

16S1				*16S2*		
Depth (CM)	**Smple quantity (g)**	**Activity (Bq.kg^{-1})**	**Errors%**	**Smple quantity (Kg)**	**Activity (Bq.kg^{-1})**	**Errors%**
[00-02]	0.081	76.92	0.3	78	138.59	3,1
[02-05]	0.081	91.38	0.3	0.080	137.79	3,1
[05-10]	0.081	94.01	0.3	0.077	139.7	3,1
[10-15]	0.082	84.42	0.3	0.077	148.69	3,1
[15-20]	0.078	86.7	0.3	0.076	152.04	3,1
[20-30]	0.084	87.48	0.3	0.073	183.09	3,1
[30-40]	0.085	87.71	0.3	0.071	183.75	3,1
[40-50]	0.085	80.82	0.3	0.077	183.96	3,1
[50-60]	0.088	91.37	0.3	0.077	132.78	3,1
[60-70]	0.082	91.56	0.3	0.082	118.19	3,1

Table 3.16S1 and 16S2;^{210} Pb:

16S1				*16S2*		
Depth (CM)	**Smple quantity (g)**	**Activity (Bq.kg^{-1})**	**Errors%**	**Smple quantity (Kg)**	**Activity (Bq.kg^{-})**	**Errors%**
[00-02]	0.081	45.68	8,3	0.078	55.42	8,3
[02-05]	0.081	46.96	8,3	0.080	49.28	8,3
[05-10]	0.081	43.55	8,3	0.077	48.06	8,3
[10-15]	0.082	42.59	8,3	0.077	53.44	8,3
[15-20]	0.078	42.56	8,3	0.076	49.6	8,3
[20-30]	0.084	49.4	8,3	0.073	75.32	8,3
[30-40]	0.085	41.5	8,3	0.071	74.52	8,3
[40-50]	0.085	28.89	8,3	0.077	67.82	8,3
[50-60]	0.088	26.33	8,3	0.077	40.87	8,3
[60-70]	0.082	31.21	0,3	0.082	37.11	8,3

Conclusions

Concentration values of ^{137}Cs and ^{40}K at sample 1 are lower than the corresponding values in sample 2.

Depth profiles of ^{137}Cs and ^{40}K in sample 1 have almost the same format

In sample 2 maximum of ^{137}Cs and ^{40}K concentration at 20 – 50 cm

Similar vertical distribution profiles of ^{210}Pb, ^{137}Cs and 40K at every sample.

^{137}Cs concentration values are smaller than most ^{137}Cs values observed in Europe.

In sample 2, maximum of ^{210}Pb, ^{137}Cs and ^{40}K concentration at 20 – 50 cm.

References

B.Baggoura and M.Benkrid. Level of Natural and Artificial Radioactivity in Algeria. Appl Radiat. Isot. Vol.49, No.7, pp. 867-73 (1998).

Arthur Beiser. Isabel Berg. Concepts of Modern Physics (2003). - 6th ed . MmcGraw – Hill, ISBN 0 - 07-244848 - 2 , ISBN 0 - 07 – 11096 – X (ISE).

F. Belloni, J. Himbert,O. Marzocchi, V. Romanello.Investigating incorporation and distribution of radionuclides in trinitite. Journal of Environmental Radioactivity 85 (2006) 103-120.

P.R. Danesi a,, J. Moreno b, M. Makarewicz c, D. Louvat c, Residual radionuclide concentrations and estimated radiation doses at the former French nuclear weapons test sites in Algeria. Applied Radiation and Isotopes 66 (2008) 1671– 1674.

Ehlken, S., Kirchner, G., 2002. Environmental processes affecting plant root uptake of radioactive trace elements and variability of transfer factor data: a review. J. Environ. Radioact. 58, 97-112.

Ryoko Fujiyoshi, Sadashi Sawamura, Mesoscale variability of vertical profiles of environmental radionuclides (^{40}K, ^{226}Ra ^{210}Pb and ^{137}Cs) in temperate forest soils in germany.Science of the the total environment 320 (2004) 177-188.

A. Ioannidou, M. Manolopoulou, C. Papastefanou. Temporal changes of 7Be and 210Pb concentrations in surface air at temperate latitudes (401N).Applied Radiation and Isotopes 63 (2005) 277–284.

D. Krstic, D.Nikezic,N, Stevanovic, M. Jelic, Vertical profile of ^{137}Cs in soil. Applied Radiotion and Isotopes 61 (2004)1487-1492.

M.S. AL-Masri, 2006, Vertical distribution and inventories of ^{137}Cs in the Syrian soils of the eastern Mediterranean region. Journal of Environmental Radioactivity 86 (2006)187-198

O. El Samad, K Zahraman, Baydoun, M. Nasreddine Analysis of radiocaesium in the Lebanese soil one decade after the Chernobyl accident.Journal of Environmental Radioactivity. Volume 92, Issue 2, (2007) 72–79.Journal of Environmental Radioactivity 88 (2006) 199- 204.

W. Schimmack, W.Schultz, Migration of fallout radiocaesium in a grassland soil from 1986 to (2001). Part I: Activity-depth profiles of ^{134}Cs and ^{137}Cs, Science of the Total Environment 368(2006)853-862.

UNSCEAR, 2008.United Nation Scientific Committee on the effects of Atomic Radiation. Natural Radionulide of the soil, United Nations, New York.

Post-Chernobyl ^{137}Cs released in the atmosphere due to biomass combustion: A consequence of the financial crisis in Greece

S. Stoulos, A. Ioannidou, E. Vagena, P. Koseoglou and M. Manolopoulou
Aristotle University of Thessaloniki, Nuclear Physics Laboratory, Thessaloniki 54124, Greece

Abstract
The background radiation level of ^{137}Cs at the urban atmosphere of Thessaloniki during the recent decade has been increased only due to Fukushima fallout. Since then no other signal of ^{137}Cs was observed until the winter period of 2013, when slightly elevated ^{137}Cs concentrations were measured at weekends, followed by non detectable activities in the next working days. Those episodes are a consequence of the financial crisis rose in the country since the majority of the inhabitants use wood products for residential heating releasing the ^{137}Cs absorbed by the trees after the Chernobyl accident. The ^{137}Cs signals observed were up to 12 μBq.m^{-3} one order of magnitude higher than the background measurements. In order to examine the contribution of biomass combustion a preliminary survey of various wood products as well as of bottom ashes from different domestic burning devices has been implemented. The ^{137}Cs concentration up to 11 Bq.kg^{-1} was measured in wood products and up to 500 Bq.kg^{-1} in ash samples. The release of ^{137}Cs estimated from 41% up to 89% of the wood concentrations corresponds to activities ranged from 0.8 up to 6.5 Bq of ^{137}Cs per kg of wood burned. However, a more detailed study is necessary in order to confirm the presented preliminary results.

Keyword: Chernobyl ^{137}Cs in atmosphere, biomass combustion, wood, ash

Introduction

The recent financial crisis raised in Greece after 2009 has among the others consequences an increase of biomass combustion by the inhabitants. According to the National Statistical Commission the oil and gas consumption have been reduced from 50% up to 80% the last two years comparing with the data of 2010. The customary fuels have been replaced by wood products since they are more reasonably priced.

Wood can be used in raw form or in processed form like pellets, briquettes and chips. Using wood and others bio-fuels is one of the main supplies of particulate matter, organic compounds and aerosol formations in urban areas during winter. The pollutants production is a function of various factors such as: the type and quality of the wood products as well as the burning appliance and conditions, while the pollutants accumulation in the atmosphere is influenced by the meteorological conditions and the topography of the area (Johanson at al., 2004; Caisero et al., 2009; Chrysikou & Samara, 2009; Gonçalves et al., 2010; Holden et al., 2011; Vu et al., 2012). Among the pollutants released in the atmosphere due to biomass usage some are radioactive like the long-lived ^{137}Cs and ^{90}Sr. The specific radionuclides have been inserted in the atmosphere due mainly to Chernobyl accident in 1986 and since then the forest ecosystem in Europe has been contaminated (Bunzl et al., 1988; Ronneau et al., 1991; Ravila and Holm, 1996; Fogh and Andersson, 2001; Clouvas et al., 2007; Zhiyanski et al., 2010). The contaminated biomass is not dangerous itself; however there are some health impacts especially occurred due to inhalation of the smoke and ash fine aerosols produced during the burning process as well as due to ash usage as fertilizer for soil (Bølling et al., 2009; Ladygiené et al., 2010).

The last decades after the Chernobyl accident the radioactivity in the atmosphere of Thessaloniki, Greece, is continuously measured as part of the environmental radioactivity monitoring program carried out. Naturally occurring radionuclides like radon and thoron progeny as well as Be-7 are normally present on

the urban air; while no detectable ^{137}Cs concentration is presented in the atmosphere during the previous years with a peak appeared due to Fukushima fallout (Manolopoulou et al., 2012). An exception was observed during the last winter of 2013 when some measurements showed slightly elevated ^{137}Cs concentrations at weekends, followed by non detectable activities in the next working days. Similar conclusions have been reported concerning the PM_{10} and $PM_{2.5}$ concentrations measured in the atmosphere at the same time period which are attributed to the domestic heating using biomass (Petrakakis et al, 2013). In order to examine the contribution of wood products combustion to the increase of ^{137}Cs measured in the urban atmosphere of Thessaloniki a preliminary survey of various kind of wood and pellet samples as well as of bottom ashes from different type of domestic burning devices have been implemented, in addition to the atmospheric radioactivity monitoring program. The results and data discussions are presented in this study regarding to estimate the ^{137}Cs released in the urban atmosphere of Thessaloniki due to biomass combustion.

Experimental methods and materials

The air sampling was carried out using a Staplex type TFIA-2 high volume air sampler operating with a glass fiber filter type TFAGF 810 with dimensions 8'' x 10'' and the collection efficiency was 95% of particles 0.3 μm and over. This design involves a regulated air flow rate ranging from 28 to 31 $L.s^{-1}$. The length of collection period was about 24 h and the air sample quantity was around 2,800 m^3. The location of the air sampling was 25 m above the ground at the roof of a building near by the center of the city whereat the main contributors of biomass combustion were: (a) the fireplaces existed in the majority of the dwellings at the 'historic' town of the city and (b) the wood- and/or pellet-stove used by the inhabitants at the center of the city whereat no central heating devices existed at the dwellings.

The wood samples collected came from two areas, Hmathia and Chalkidiki, which are the main providers of wood for the residential burning devices in Thessaloniki city. Three types of wood have been measured: oak, beech and plane. Imported wood and pellet samples produced in Serbia, Bulgaria and Romania were also measured. The samples were oven-dried at 40°C to constant weight. The bottom ash samples were collected from different type of domestic burning devices like fireplaces as well as wood- and pellet-stoves. The samples were oven-dried at 80°C to constant weight.

All samples were measured for radioactivity using a high purity and low background Ge detector of high resolution (1.9 keV at 1.33 MeV) and high efficiency (42%). The air filters collected were measured using 'standard filter' geometry (Ø 8 cm) for 400000 sec regarding to obtain the best statistical-counting uncertainty. Marinelli geometry (1 litre) was used for ash and pellet samples while the wood samples measured have a cylindrical form. The γ-spectrometric system was calibrated using standard reference sources for filter and ash samples while for wood and pellet samples the counting efficiency were determined using GEANT code simulations. The overall uncertainty of measurements was ranged between 25–41 % for the filter geometry, < 5% for the ash samples and 12-40% for woods and pellets.

Results and Discussions

The background radiation level of ^{137}Cs at the urban atmosphere of Thessaloniki during the recent decade (2010-2013) was lower than the Minimum Detectable Activity (MDA) of the counting systems used, i.e. < 2 $\mu Bq.m^{-3}$, with an exception due to Fukushima fallout. The activity concentrations of aerosol-bound ^{137}Cs in air from March 24, 2011 through April 25, 2011 ranged from <5 up to 145 $\mu Bq.m^{-3}$ accompanied by ^{134}Cs in similar concentrations. Since then no other signal of ^{137}Cs was observed until the winter period of 2013, soon after the high increase of

'domestic usage oil' price due to the recommendations applied regarding to face off the financial crisis rose in the country.

The data of ^{137}Cs concentrations obtained in the urban atmosphere of Thessaloniki through January – March 2013 are presented in Figure 1. Values ranged between 3.6 (±41%) - 9.4 (±26%) μBq.m^{-3} were measured during only weekends when the inhabitants spend their time indoors with the domestic wood-heating devices working constantly all day long. The following days the signal of radioactivity was removed since the inhabitants were at their working place or at school during the day time whereat central oil- or gas- burning devices were used.

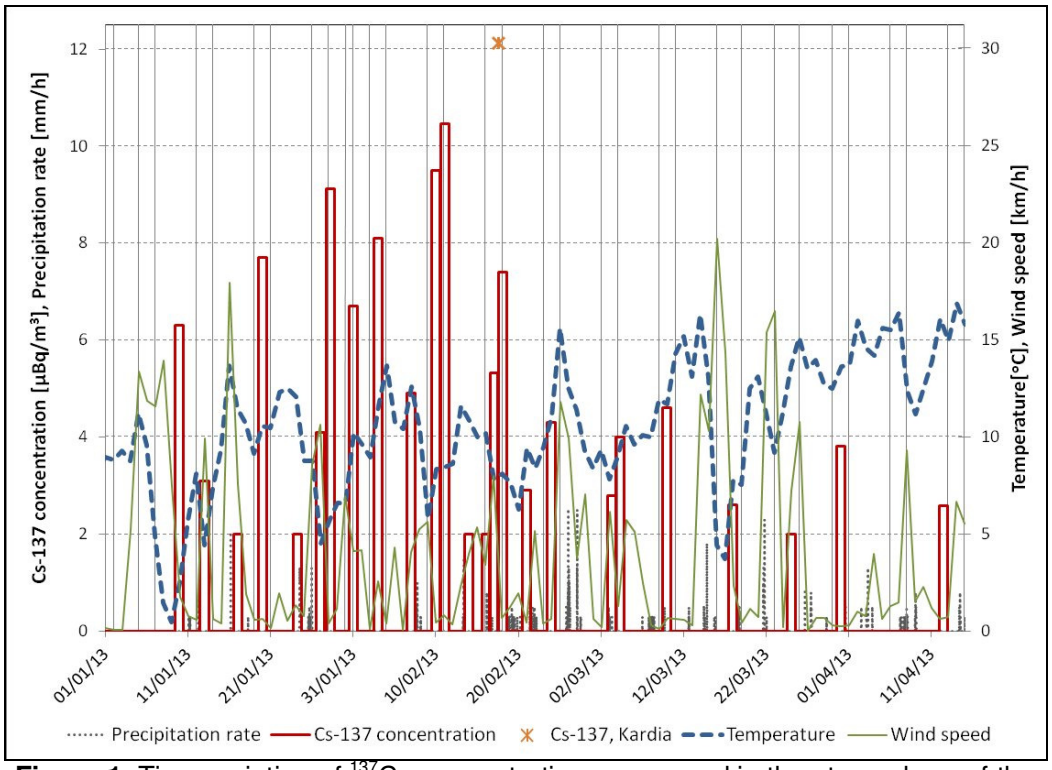

Figure 1. Time variation of ^{137}Cs concentrations measured in the atmosphere of the Thessaloniki during winter 2013 in association with meteorological conditions.

The signals of ^{137}Cs accumulation in the atmosphere were influenced by the meteorological conditions of the time period studied, i.e. the temperature and wind velocity. The low wind velocity joint with low temperature triggers the increase of wood consumption for heating and in addition the accumulation of aerosol-bound ^{137}Cs in the atmosphere. That could be the reason of the highest concentration measured during February 11, 2013 (see fig.1) when both wind velocity and temperature were the lowest. In contrary, during February 2, 2013 measurement no signal was presented due to highest temperature and wind velocity appeared for this time period. The topography of the sampling location was also affecting the ^{137}Cs accumulation in the atmosphere as it is presented in figure 1, where simultaneous measurement take place at the standard sampling location and also at the suburbs of Thessaloniki area during February 17, 2013. The standard sampling location was placed at an almost open landscape while the location in the suburbs resembled with a closed urban gap. Therefore, higher concentration was measured in the closed urban gap, 10.9 (±25%) μBq.m^{-3}, due to air-mass trapping than at the open landscape, 6.63 (±36%) μBq.m^{-3}. However, a more detailed study of the influence due to

meteorological conditions and the topography of the urban area are necessary in order to clarify the subject.

In order to examine the contribution of wood products combustion to the increase of ^{137}Cs measured in the urban atmosphere of Thessaloniki a preliminary survey of various kind of wood and pellet samples as well as of bottom ashes from different type of domestic burning devices have been implemented. According to the experimental results, the ^{137}Cs concentrations of the ash collected was ranged from 31 up to 64 $Bq.kg^{-1}$ concerning appliances that burning imported woods from the Balkan area while the respect activities for imported pellets was 174 $Bq.kg^{-1}$. The concentrations in the ash originated by enchorial woods combustion were estimated as 25 up to 500 $Bq.kg^{-1}$, which presented to be higher than ashes originated by imported wood (see Table 1) indicating the higher Chernobyl fallout deposition in North Greece than in the neighbor countries. Wood samples originated from oak trees contained the lowest ^{137}Cs concentrations measured, lower than 1.3 $Bq.kg^{-1}$, while the concentrations in beech and plane trees ranged up to 11.0 $Bq.kg^{-1}$ (see Table 2). That could be attributed to the different growing location of each type in the forest ecosystem. Concerning ^{40}K measurements no deviations were presented due to different type of wood products used.

Table 1. Activity concentrations measured in ash samples ($Bq.kg^{-1}$).

Ash samples originate by	^{137}Cs	^{40}K
wood imported from Bulgaria-Romania [7]*	31 – 64	3280 – 4370
pellet imported from Serbia [1]	174	3082
wood enchorial [16]	25 - 499	1592 - 7060

The values in the brackets refer to the number of samples.

The activities presented in Tables 1 and 2 are in good agreement with previously reported data during the last years by others that referred to the same area and wood products (Clouvas et al., 2007; Zhiyanski et al., 2010; Ladygiené et al., 2010; Desideri et al., 2012). The ^{137}Cs activities measured were lower than the exemption level of 10 Bq per gram according to the Council Directive 96/29/EURATOM, so no public radiological risks arise due to use of the specific ash for soil fertilisations.

Table 2. Activity concentrations measured in wood products ($Bq.kg^{-1}$). The values in the brackets refer to the number of samples.

Wood product originated by	^{137}Cs	^{40}K
Oak trees [4]*	< 0.3 – 1.33	12 - 37
Beech trees [4]	< 0.3 – 11.02	35 - 34
Plane tree [1]	8.18	23
Pellet imported from Serbia [1]	5.20	36

* The values in the brackets refer to the number of samples.

The activities measured in ash samples were enriched compared to the activities of the wood products burned due to removal of organic compound during combustion. Regarding to estimate the ash-to-wood enrichment factor as a function of domestic heating devices the ^{40}K concentrations were used taken under consideration that K is less volatile than Cs and so the whole amount contained in the wood fuels are settled down to the ash produced. The ash-to-wood enrichment factor was ranged from 77 up to 209 for fireplaces, 107 up to 118 for wood-stoves and 85 for the pellet-stove, according to the experimental results presented in Table 3. The enrichment factors estimated in the present study were similar with those reported in the literature (Ladygiené et al., 2010).

Table 3. Ash-to-wood enrichment factor estimated using ^{40}K concentrations. The values in the brackets refer to the number of samples.

Type of appliance	Wood ($Bq.kg^{-1}$)	Ash ($Bq.kg^{-1}$)	Ash / Wood
Fireplace [5]*	12 – 34	2602 - 3322	77 - 209
Wood-stove [2]	35 - 37	3928 - 4096	118 - 107
Pellet-stove [1]	36	3082	85

* The values in the brackets refer to the number of samples.

The ash-to-wood enrichment factors estimated for ^{40}K were applied to the data of ^{137}Cs obtained regarding to estimate the activities subsided at the bottom ashes. Due to MDA measured in three wood samples studied the number of appliances used for Cs calculations were less than the K ones. The ^{137}Cs released in the urban atmosphere of Thessaloniki due to biomass combustion were ranged between 41% up to 89% of the activity concentration in the wood products used according to the results presented in Table 4.

Table 4. ^{137}Cs released in the atmosphere (%) according to the activities measured ($Bq.kg^{-1}$) in wood and ash products. The values in the brackets refer to the number of samples.

Type of appliance	Wood/Pellet	Ash	Realised in atmosphere
Fireplace using plane and beech [2]*	8.18 – 11.02	1.67 – 6.51	80 – 41
Wood-stove using oak and beech [2]	1.33 – 3.11	0.56 – 0.33	57 – 89
Pellet-stove [1]	5.20	2.04	61

* The values in the brackets refer to the number of samples.

Assuming that 1-5 Bq of ^{137}Cs released in the atmosphere by each heating device and 10^4 are a reasonable number of devices working during the weekend then values from 10 up to 60 KBq of ^{137}Cs released per Kg of wood burned. These values could support the concentrations of aerosols-bound ^{137}Cs measured in the atmosphere.

Conclusions

Signals of ^{137}Cs have been observed during the winter of 2013 in the urban atmosphere of Thessaloniki, which were up to one order of magnitude higher than the background measurements. The ^{137}Cs concentrations measured were up to 12 $\mu Bq.m^{-3}$ one order of magnitude higher than the background measurements at they appeared only during weekends followed by no detectable values the next working days. The signals were influenced by meteorological conditions and the topography of the area. Those episodes are a consequence of the financial crisis rose in the country since the majority of the inhabitants turn to wood products for residential heating releasing the ^{137}Cs absorbed by the trees after the Chernobyl accident. According to the preliminary results of this study ^{137}Cs concentration up to 11 $Bq.kg^{-1}$ was measured. The release of ^{137}Cs estimated from 41% up to 89% of the wood concentrations corresponds to activities ranged from 0.8 up to 6.5 Bq of ^{137}Cs per Kg of wood burned. However, a more detailed study is necessary in order to confirm the preliminary results presented.

Acknowledgements

Special gratitude is due to the inhabitants in Thessaloniki city, Hmathia and Chalkidiki whom heating devices and wood products were the experimental set-up of this study.

References

Bølling, A.K., Pagels, J., Yttri, K.E., Barregard, L., Sallsten, G., Schwarze, P.E., Boman, C., 2009. Health effects of residential wood smoke particles: the importance of combustion conditions and physicochemical particle properties. Particle and Fibre Toxicology 6, 29. doi:10.1186/1743-8977-6-29.

Bunzl, K., Kracke, W., 1988. Cumulative deposition of cesium-137, plutonium-238, plutonium-239, plutonium-240 and americium-241 from global fallout in soils from forest, grassland and arable land in Bavaria, West Germany. J. Environ. Radioact. 8, 1-14.

Caseiro, A., Bauer, H., Schmidl, C., Pio, C.A., Puxbaum, H., 2009. Wood burning impact on PM10 in three Austrian regions. Atmosp. Environ. 43, 2186-2195.

Chrysikou, L.P. and Samara, C.A., 2009. Seasonal variation of the size distribution of urban particulate matter and associated organic pollutants in the ambient air. Atmosph. Environ. 43 , 4557–4569.

Clouvas, A., Xanthos, S., Takoudis, G., Antonopoulos-Domis, M., Alifrangis, D.A., Zhiyanski, M., Sokolovska, M., 2007. Follow up study of radiocesium contamination in a Greek forest ecosystem. Health Phys. 93, 312-317.

Desideri, D., Rongoni, A., Roselli, C., Saetta, D., Feduzi, L., 2012. Analytical methods for the determination of ^{137}Cs and ^{90}Sr in ash of fuel pellets used in Italy. Microchemical Journal 103, 131–134.

Fogh, C.L. and Andersson, K.G., 2001. Dynamic behaviour of ^{137}Cs contamination in trees of the Briansk region, Russia. Sci. Total Environ. 269, 105-115.

Gonçalves, C., Alves, C., Evtyugina, M., Mirante, F., Pio, C., Caseiro, A., Schmidl, C., Bauer, H., Carvalho, F., 2010. Characterisation of PM10 emissions from woodstove combustion of common woods grown in Portugal. Atmosp. Environ. 44, 4474-4480.

Holden, A.S., Sullivan, A.P., Munchak, L.A., Kreidenweis, S.M., Schichtel, B.A., Malm, W.C., Collett Jr., J.L., 2011. Determining contributions of biomass burning and other sources to fine particle contemporary carbon in the western United States. Atmosp. Environ. 45, 1986-1993.

Johansson, L.S., Leckner, B., Gustavsson, L., Cooper, D., Tullin, C., Potter, A., 2004. Emission characteristics of modern and old-type residential boilers fired with wood logs and wood pellets. Atmospheric Environment 38, 4183-4195.

Ladygienė, R., Orentienė, A., Pilkytė, L., Skripkienė, A., Žukauskaitė, V., Kievinas, R., 2010. Radiological investigation of wood used for combustion. Ekologija 56, 87-93.

Manolopoulou, M., Stoulos, S., Ioannidou, A., Vagena, E. and Papastefanou, C., 2012. Radiation measurements and Radioecological aspects of fallout from the Fukushima nuclear accident. J. Radioanal. Nucl. Chem. 292, 155–159.

Petrakakis, M.J., Kelessis, A.G., Tzoumaka, P.N., and Samara, C., 2013. Levels of suspended particulate matter before and after the economic crisis in Thessaloniki, Greece. Pros. 17th International MESAEP Symposium, Istanbul-Turkey, 28 Sept.-1 Oct. 2013.

Ravila, A. and Holm, E., 1996. Assessment of the radiation field from radioactive elements in a wood-ash-treated coniferous forest in southwest Sweden. J. Environ. Radioact. 32, 135-156.

Ronneau, C., Sombre, L., Myttenaere, C., Andre, P., Vanhouche, M., Cara, J., 1991. Radiocesium and potassium behaviour in forest trees. J. Environ. Radioact. 14, 259-268.

Vu, B., Alves, C.A., Gonçalves, C., Pio, C., Carvalho, F. Pereira, R., 2012. Mutagenicity assessment of aerosols in emissions from wood combustion in Portugal. Environ. Pollution 166, 172-181.

Zhiyanski, M., Sokolovska, M., Bech, J., Clouvas, A., Penev, I., Badulin, V., 2010. Cesium-137 contamination of oak (Quercus peterae Liebl.) from sub-mediterranean zone in South Bulgaria. J. Environ. Radioact. 101, 864-868.

Covariant Density Functional Theory

Georgios A. Lalazissis
Department of Theoretical Physics, Aristotle University of Thessaloniki

Abstract

In recent years covariant density functional theory has developed as a very successful tool to describe nuclear structure phenomena. We discuss in this article, why Lorentz invariance should be taken seriously in this context and show several very successful nuclear applications of relativistic density functional theory.

Introduction

The possibility to investigate the nuclear chart to the very limits of nuclear binding by new accelerators with radioactive beams has stimulated considerable new efforts on the theoretical side to understand the dynamics of the nuclear many-body problem by microscopic methods. Density Functional Theory (DFT) [1] is a powerful tool for studying ground state (g.s) properties of finite nuclei at and away from stability. It is based on the Hohenberg-Kohn (H-K) [2] theorem which states that the g.s properties can be represented by the g.s density alone. The g.s results from the minimization of the total energy of the functional. For practical applications in nuclear physics, we use the effective Kohn-Sham (K-S) [3] equation. The idea is to introduce an auxiliary system of non-interacting particles that generates the same densities as any given system of interacting particles. The K-S equation is defined by a local effective potential in which the non interacting particles are moving. Certainly, the K-S wave function is a single determinant constructed by the loewst energy solutions. The uniqueness of the effective potential U_{eff} follows from K-S theorem, as the single particle orbits are unique functions of the density:

$$\varphi_i(\mathbf{r}) \equiv \varphi_i([\rho], \mathbf{r})$$

One of the underlying symmetries of QCD is Lorentz invariance and therefore covariant density functionals (CDFT) are of particular interest in nuclear physics [4-5] . This symmetry not only allows to describe the spin--orbit coupling in a consistent way, but it also puts stringent restrictions on the number of parameters in the corresponding functionals without reducing the quality of the agreement with experimental data. Therefore,a relatively small number of parameters is necessary, which are adjusted to reproduce a set of bulk properties of spherical nuclei. The resulting energy density functionals (EDF) are considered universal in the sense that they can be used for nuclei all over the chart of nuclides, where mean field is applicable, for ground state properties as well as for excited states.

It is well known that non-relativistic Brueckner calculations based on two-body forces are not able to reproduce the saturation point in symmetric nuclear matter. Therefore phenomenological three-body forces have been introduced in non-relativistic ab-initio calculations. The situation is different in relativistic Brueckner theory, where one does not need three-body forces in order to reproduce saturation. Although it is still an open question, whether there is a connection between three-body forces and relativistic effects, this is a strong hint that relativistic effects should not be neglected in ab-initio calculations.

There exists a *relativistic saturation mechanism :* Non-relativistic Hartree calculations with such simple interactions would lead to a collapse. Therefore one has introduced in such theories a strongly

repulsive term depending on the density. In the relativistic model this is not necessary. The source of the attraction is the scalar density, which because of Lorentz invariance is automatically quenched at high densities. This relativistic effect leads always to saturation. This is a genuine relativistic effect which is taken into account in the present non-relativistic descriptions by introducing additional terms with additional parameters.

Covarinat Density Functional Theory

The essential ingredient of density functional theory is the Kohn-Sham equation with its effective single particle potential, the self energy. In a relativistic description it has the form of a Dirac equation

$$\begin{pmatrix} m + W_+ & \vec{\sigma} \cdot \vec{p} \\ \vec{\sigma} \cdot \vec{p} & -m + W_- \end{pmatrix} \begin{pmatrix} \mathrm{g} \\ \mathrm{f} \end{pmatrix} = \epsilon_i \begin{pmatrix} \mathrm{g} \\ \mathrm{f} \end{pmatrix}.$$

The potentials W_+ = V+S and W_= V-S contain an attractive scalar field S and a repulsive vector field V. In the simplest form of the Walecka model [7] for symmetric nuclear matter these two numbers are adjusted to the saturation point (binding energy and density) and it is found that these potentials are very large having nearly the same size, but opposite phase: ≈ 400 MeV and ≈ 350 MeV. Therefore the nucleons in the Fermi sea feel a relatively week potential W_+=V+S ≈ -50 MeV. Their Fermi momentum is roughly 250 MeV/c and small as compared to the rest mass of a nucleon m ≈ 940 MeV/c^2. This shows clearly that we do not need relativistic kinematics in order to describe phenomena of low energy nuclear structure. By this reason non-relativistic functionals are very successful, if their parameters are carefully chosen. As compared to the non-relativistic description covariant theories show a number of technical difficulties: The solution of the Dirac equation is definitely more complicated than the Schroedinger equation. In dynamic applications for the investigations of excited states the Dirac sea has to be treated properly [6]. Therefore it is understandable that large parts of the community prefer non-relativistic functionals, where standard computer codes are available and where much experience has been accumulated since more than 40 years. Nonetheless there are important arguments for covariant density functionals. Most of them are based on the simplicity and beauty of the Walecka model [7], which serves as a vehicle to implement relativistic symmetries.
Usually nuclear density functionals are adjusted to experimental ground state properties or to nuclear matter data. They depend only on time even parts of the potentials and therefore in non-relativistic density functionals the time odd parts show some ambiguity. Covariant functionals have the advantage that the *time odd fields* described by the currents, i.e., the spatial components of the vector fields, have the same coupling constant as the time-like components. No new parameters are required. This effect is usually called *nuclear magnetism*. In fact, some of the applications of non-relativistic density functional theory fail to describe the moments of inertia of rotational bands properly. On the other side, relativistic applications to rotational ground state bands, to super-deformed and magnetic dipole bands show good agreement with experimental data [5]. A proper treatment of nuclear magnetism is crucial.

The most successful EDF originate from the Relativistic Hartree Bogoliubov (RHB) model in which p-h and p-p channels are treated simultaneously in a self-consistent manner. A large variety of nuclear phenomena have been described over the years within this model, the equation of state of symmetric nuclear matter, ground state properties of finite spherical and deformed nuclei at and far away from the valley of stability. The model is able to describe very successfully exotic phenomena such as nuclei, weakening of shell effects away from stability line, super-heavy nuclei. In addition the model can successfully describe excited states, particularly those of collective character.

In time dependent systems there is no variational principle on the basis of the total energy because it is not conserved quantity. For this a new theorem has been proposed which somewhat is sort of formal foundation of time-dependent density functional theory. This is the Runge Gross (R-G) theorem [8]. It shows that the density can be used as fundamental variablein describing quantum many-body systems in place of the wave function and thayt all properties of the system are functionals of the density. Starting from R-G theorem, one is able to derive the time dependent K-S equations and then using the adiabatic approximation excited states can be described. For example rotational bands in normal deformed and superdeformed nuclei [5]. Rotations are treated in the cranking approximation which provides a quasi-static description of the nuclear dynamics in rotating frame.

Giant Resonances

For the description of vibrations, a time-dependent mean field approximation is used by assuming independent particle motion in time dependent average field. In the small In the small amplitude limit, one obtains the relativistic Random Phase Approximation (RRPA) [6] and for open shell nuclei the corresponding relativistic quasi-particle random phase approximation (QRPA) [9]. This method provides a natural framework to investigate collective and non-collective excitations of ph character. It is successful, in particular, for understanding the position of giant resonances and spin-or/and isospin excitations such as the Gamow-Teller Resonance (GTR) or the isobaric Analog Resonances (IAR) [10]. The corresponding eigenmodes can be determined either by diagonalizing the RRPA / RQRPA equations in an appropriate basis~[6] or by solving the linear response equations in time-dependent external field [11]. The two methods lead, in principle, to exactly identical results. It should be noted however, that the second method provides a more consistent treatment of the coupling to the continuum.
The fully self-consistent RRPA [12] and RQRPA [9] have been used to calculate excitation energies of giant resonances in doubly-closed and open-shell nuclei, respectively. The RQRPA is formulated in the canonical basis of the RHB model and, both in the ph and pp channels, the same interactions are used in the RHB equations that determine the canonical quasiparticle basis, and in the matrix equations of the RQRPA. For ^{208}Pb the RRPA results for the monopole (ISGMR) and isovector dipole (IVGDR) response with the DD-ME2 force[13] are in excellent agreement with experiment [14-15]. The same is the case with RQRPA calculations in the Sn isotopic chain, where RHB+RQRPA calculation with the DD-ME2 interaction reproduce in detail the experimental excitation energies and the isotopic dependence of both the IVGDR andISGMR.

Pygmy Resonances

Using the relativistic QRPA scheme CDFT can also be used to study nuclear excitations and new modes have been found. On the neutron-rich side, in particular, the possible occurrence of the pygmy dipole resonance (PDR), i.e. the resonant oscillation of the weakly-bound neutron skin against the isospin saturated proton-neutron core, has been investigated. On the theory side, various models have been employed in the investigation of the nature of the low-lying dipole strength [16], in particular also the relativistic quasiparticle RPA (RQRPA)~[17]. The calculated value (7.13 MeV) is in excellent agreement with recent experimental information.
We can also use the relativistic QRPA to study the evolution of low-lying dipole strength in proton-rich nuclei~[18]. The study of the N=20 isotones: 40Ca, 42Ti, 44Cr, and 46Fe shows that as the number of proton increases, low-lying dipole strength appears in the region below the GDR. The low-lying state represents a fundamental mode ofexcitation: the proton electric pygmy dipole resonance (PDR).

Beyond the mean field

It should be noted, however, that nuclear DFT based on the mean field framework cannot provide an exact treatment of the full nuclear dynamics. It is known to break down in transitional nuclei, where one has to include correlations going beyond the mean field approximation by treating quantum fluctuations through a superposition of several mean field solutions as for instance in the generator coordinate method (GCM)~[19]. Starting from constrained self-consistent mean field calculations of potential energy curves the GCM method is used to perform configuration mixing of angular momentum and particle-number projected relativistic wave functions. The resulting GCM spectra in the region of rare earth nuclei were found in excellent agreement with data. Moreover, the GCM appraoch , within CDFT, gave very good results in a macroscopic analysis of nuclear quantum phase transitions in the N≈ 90 region [20-21].

It is also known that even in ideal shell model nuclei such as in ^{208}Pb, with closed proton and neutron shells one finds in self-consistent mean field calculations usually a single particle spectrum with a considerable enhanced Hartree-Fock gap in the spectrum and a reduced level density at the Fermi surface as compared with experiment. The situation is considerable improved by taking into account the energy dependent part of the self-energy and treating it in terms of the particle-vibration coupling model PVC [22-24]. Moreover, we get accurate information not only for the position of the giant resonances but also for their widths in agreement with the experimental observations [25].

Summary

In conclusion, covariant DFT provides a very successful and microscopic description for ground states and excited states in nuclei. Most of the successful functionals are at present phenomenological. On the mean field level there is no energy dependence of the self-energy, no fluctuations are taken into account and symmetry violations are not treated properly. The energy dependence of the self energy can be treated by means of the particle vibration model, while the symmetries and fluctuations can be considered by projections and the GCM method. Many things should be done in future. On the static part, we are still far from a microscopic derivation of the model. We have to improve the functionals both in ph- and pp-channels. On the dynamical part: the PVC model is so far restricted to spherical systems and GCM is so far restricted to very few degrees of freedom.

References

[1] M. Bender, P.-H. Heenen, and P.-G. Reinhard, Rev. Mod. Phys. **75**, 121 (2003)
[2] P. Hohenberg and W. Kohn, Phys. Rev. **136**, B864 (1964)
[3] W. Kohn and L.J. Sham, Phys. Rev. **140**, A1133 (1965)
[4] P. Ring, Prog. Part. Nucl. Phys. **37**, 193 (1996)
[5] D. Vretenar, A. Afanasjev, G. Lalazissis, and P. Ring, Phys. Rep. **409**, 101 (2005)
[6] P. Ring et al, Nucl. Phys. A **694**, 249 (2001)

[7] J. D. Walecka, Ann. Phys. (N.Y.) **83**, 491 (1974)
[8] E. Runge and E. K. U. Gross, Phys. Rev. Lett. **52**, 997 (1984)
[9] N. Paar, P. Ring, T. Niksic, and D. Vretenar, Phys. Rev. C **67**, 034312 (2003)
[10] N. Paar, T. Niksic, D. Vretenar, and P. Ring, Phys. Rev. C **69**,054303 (2004).
[11] J. Daoutidis and P. Ring, Phys. Rev. C **80**, 024309 (2009)
[12] T. Niksic, D. Vretenar, and P. Ring, Phys. Rev. C **66**, 064302 (2002)
[13] G.A. Lalazissis, T. Niksic, D. Vretenar, and P. Ring, Phys. Rev. C**71**, 024312 (2005)
[14] B.L. Berman and S.C. Fultz, Rev. Mod. Phys. **47**, 713 (1975)
[15] T. Li, U. Garg et al, Phys. Rev. Lett. **99**, 162503 (2007)
[16] N. Paar, D. Vretenar, E. Khan, and G. Colo, Rep. Prog. Phys. **70**, 691(2007)
[17] D. Vretenar, N. Paar, P. Ring and G.A. Lalazissis, Nucl. Phys. A **692**. (2001) 496
[18] N. Paar, D. Vretenar, and P. Ring, Phys. Rev. Lett. **94**, 182501 (2005)
[19] T. Niksic, D. Vretenar, and P. Ring, Prog. Part. Nucl. Phys. **66**, 519(2011)
[20] T. Niksic, D. Vretenar, G.A. Lalazissis and P. Ring, Phys. Rev. Lett. **99**, 092502 (2007)
[21] Z.P. Li, T. Niksic, D. Vretenar, J. Meng, G.A. Lalazissis, P. Ring, Phys. Rev C**79**, 054301 (2009)
[22] P. Ring and E. Litvinova, Phys. At. Nucl. **72**, 1285 (2009).
[23] E. Litvinova and P. Ring, Phys. Rev. C **73**, 044328 (2006).
[24] E. Litvinova, P. Ring, and V. I. Tselyaev, Phys. Rev. C **75**, 06430 (2007).
[25] E. Litvinova, P. Ring, and V. I. Tselyaev, Phys. Rev. C **78** , 014312 (2008).

Non standard neutrino interactions at the Spallation Neutron Source

D.K. Papoulias[1], T.S. Kosmas[2]

Division of Theoretical Physics, University of Ioannina, GR 45100 Ioannina, Greece

Abstract

In this work, we explore ν-nucleus processes from a nuclear theory point of view and derive results with high confidence level, based on accurate nuclear structure cross sections calculations. The present study includes total number of exotic events predicted to be measured for the various channels of the nonstandard neutrino-nucleus reactions and comes out with promising results within the current upper limits of the corresponding exotic parameters. We concentrate on the possibility of detecting laboratory neutrinos produced near the spallation neutron source facilities (at Oak Ridge National Lab) by the COHERENT experiment.

Keywords: `lepton flavour violation`, `nonstandard interactions`, `Spallation Neutron Source`, `neutrino-nucleus reactions`, `coherent scattering`

1. Introduction

Coherent scattering of neutrinos on complex nuclei was proposed long ago [1, 2] as a prominent probe to study neutral-current (NC) ν-nucleus processes, but up to now no events have been experimentally measured. Neutrino detection constitutes an excellent probe to search for a plethora of conventional neutrino physics applications and new-physics open issues [3]. In principle,

[1]e-mail:dimpap@cc.uoi.gr
[2]e-mail:hkosmas@uoi.gr

low-energy astrophysical and laboratory neutrino searches provide crucial information towards understanding the underling physics of the fundamental electroweak interactions within and beyond the SM [4, 5]. Well-known neutrino sources include (i) supernova neutrinos (with energies up to 60-100MeV) and (ii) laboratory neutrinos (with energies up to 52.8MeV) emerging from stopped-pion and muon decays at muon factories (Fermilab, PSI, JPARC, etc.) as well as at the spallation neutron source (SNS) at Oak Ridge National Lab [6, 7]. In recent years, it became feasible to detect neutrinos by exploiting the neutral current interactions and measuring the nuclear recoil signals through the use of very low threshold-energy detectors [8, 9]. To this purpose, great experimental effort has been put and new experiments have been proposed to be performed at facilities with stopped-pion neutrino beams, based on promising nuclear detectors like those of the COHERENT experiment [10, 11] at the SNS, or alternative setups at the Booster Neutrino Beam (BNB) at Fermilab [12]. The nuclear ν-detectors adopted by the relevant experiments include, ^{20}Ne, ^{40}Ar, ^{76}Ge and ^{132}Xe, detection materials [13].

Recently, neutral-current (NC) nonstandard interactions (NSI) involving (anti)neutrino scattering processes on leptons, nucleons, and nuclei have been extensively investigated [15]. The reactions of this type that take place in nuclei are represented by

$$(\tilde{\nu}_\alpha)\nu_\alpha + (A, Z) \to (\tilde{\nu}_\beta)\nu_\beta + (A, Z)\,, \tag{1}$$

($\alpha, \beta = e, \mu, \tau$ with $\alpha \neq \beta$). It has been suggested that, theoretically, the latter processes can be studied with the same nuclear methods as the exotic cLFV process of $\mu^- \to e^-$ conversion in nuclei [14]. The corresponding Lagrangians may be derived within the context of various extensions of the SM, like the seesaw mechanism [3, 16, 17].

It is well known that neutrino NSI may have rather significant impact in many areas of modern physics research and thus motivate a great number of similar studies [18]. Particularly in astrophysical applications, constraints coming out of some supernova explosion scenarios may be affected [19] and eventu-

ally lead to the necessity of further investigation of NSI in both LFV and cLFV processes [20, 21] that may occur in solar and supernova environment [22]. Such open issues motivated our present work too.

2. The formalism

2.1. Nonstandard neutrino-nucleus cross sections

The study of neutral current nonstandard neutrino interactions, initially begins by assuming the quark-level NSI Lagrangian at the four fermion approximation, $\mathcal{L}_{\rm NSI}$, parametrized (for energies $\ll M_Z$) as [4, 6]

$$\mathcal{L}_{\rm NSI} = -2\sqrt{2}G_F \sum_{\substack{f=u,d \\ \alpha,\beta=e,\mu,\tau}} \epsilon^{fP}_{\alpha\beta} \left[\bar{\nu}_\alpha \gamma_\rho L \nu_\beta\right] \left[\bar{f}\gamma^\rho P f\right] . \tag{2}$$

Here, three light neutrinos ν_α with Majorana masses are considered, f denotes a first generation SM quark and $P = \{L, R\}$ are the chiral projectors. In the latter Lagrangian (2), enter flavour preserving non-SM terms, known as non-universal (NU) interactions that are proportional to $\epsilon^{fP}_{\alpha\alpha}$, as well as flavour-changing (FC) terms proportional to $\epsilon^{fP}_{\alpha\beta}$, $\alpha \neq \beta$. These couplings are taken with respect to the strength of the Fermi coupling constant G_F [18]. In the present work we examine spin-zero nuclei thus, we are mainly interested for the polar-vector couplings defined as $\epsilon^{fV}_{\alpha\beta} = \epsilon^{fL}_{\alpha\beta} + \epsilon^{fR}_{\alpha\beta}$. For the case of the axial-vector couplings it holds $\epsilon^{fA}_{\alpha\beta} = \epsilon^{fL}_{\alpha\beta} - \epsilon^{fR}_{\alpha\beta}$.

Recently, it became feasible that terrestrial neutrino detectors expect to detect neutrino events by measuring nuclear recoils [6]. The NSI coherent differential cross section of neutrinos scattering off a spin-zero nucleus, with respect to the recoil energy of the nuclear target, T_N reads [5]

$$\frac{d\sigma_{{\rm NSI},\nu_\alpha}}{dT_N} = \frac{G_F^2 M}{\pi}\left(1 - \frac{M T_N}{2E_\nu^2}\right) \left|\langle gs||G^{\rm NSI}_{V,\nu_\alpha}(q)||gs\rangle\right|^2 , \tag{3}$$

$\alpha = e, \mu, \tau$, denotes the flavour of incident neutrinos and $|gs\rangle$ represents the nuclear ground state (for even-even nuclei, $|gs\rangle = |J^\pi\rangle \equiv |0^+\rangle$). The NSI

nuclear matrix element, that enters the cross section, is written as [15]

$$\begin{aligned}\left|\mathcal{M}^{\rm NSI}_{V,\nu_\alpha}\right|^2 \equiv \left|\langle gs||G^{\rm NSI}_{V,\nu_\alpha}(q)||gs\rangle\right|^2 = \\ \left[\left(2\epsilon^{uV}_{\alpha\alpha}+\epsilon^{dV}_{\alpha\alpha}\right)ZF_Z(q^2)+\left(\epsilon^{uV}_{\alpha\alpha}+2\epsilon^{dV}_{\alpha\alpha}\right)NF_N(q^2)\right]^2 \\ +\sum_{\beta\neq\alpha}\left[\left(2\epsilon^{uV}_{\alpha\beta}+\epsilon^{dV}_{\alpha\beta}\right)ZF_Z(q^2)+\left(\epsilon^{uV}_{\alpha\beta}+2\epsilon^{dV}_{\alpha\beta}\right)NF_N(q^2)\right]^2,\end{aligned} \tag{4}$$

($\beta = e, \mu, \tau$) where $F_{Z(N)}$ denote the nuclear (electromagnetic) form factors for protons (neutrons) entered due to the CVC theory. We stress that in the adopted NSI model, the coherent NC ν-nucleus reaction should not considered as flavour blind process. By incorporating the previously mentioned nuclear structure details, the cross sections become more realistic and accurate [5].

2.2. Nuclear structure

We study the nuclear structure details of the relevant matrix elements exploring the dependence of the coherent cross section on the incident-neutrino energy E_ν and the the recoil energy T_N. For the case of the even-even nuclei this study involves realistic QRPA calculations for the differential cross sections $d\sigma_{\nu_\alpha}/dT_N$, performed after constructing the nuclear ground state by solving iteratively the Bardeen Cooper Schrieffer (BCS) equations. The solution of these equations provides the probability amplitudes $\upsilon^j_{N_n}$ and $\mathrm{v}^j_{N_n}$ of the j-th single nucleon level to be occupied or unoccupied, respectively. Moreover, the latter equations provide the single quasiparticle energies, based on the single particle energies of the nuclear field (a Coulomb corrected Woods-Saxon potential in our case) as well as the pairing part of the residual two-body interaction (Bonn C-D potential in our case). Then, the nuclear form factors for protons (neutrons) are obtained as [22]

$$F_{N_n}(q^2) = \frac{1}{N_n}\sum_j [j]\,\langle j|j_0(qr)|j\rangle\left(\upsilon^j_{N_n}\right)^2 \tag{5}$$

with $[j]=\sqrt{2j+1}$, $N_n = Z$ (or N). For each nuclear system, the chosen active model space, as well as the required monopole (pairing) residual interaction which was obtained from a Bonn C-D two-body potential (strong two-nucleon

forces) and slightly renormalized with two parameters $g_{\rm pair}^{p\,(n)}$ for proton (neutron) pairs, are presented in Table 1.

Table 1: Nuclear structure parameters for the proton $g_{\rm pair}^{p}$ and neutron $g_{\rm pair}^{n}$ pairs [15].

Nucleus	model-space	b	Δ_p	Δ_n	$g_{\rm pair}^{p}$	$g_{\rm pair}^{n}$
^{20}Ne	10 (no core)	1.727	3.81516	3.83313	1.15397	1.27600
^{40}Ar	15 (no core)	1.902	1.75518	1.76002	0.94388	1.01348
^{76}Ge	15 (no core)	2.086	1.52130	1.56935	0.95166	1.17774
^{132}Xe	15 (core ^{40}Ca)	2.262	1.19766	1.20823	0.98207	1.13370

3. Results and Discussion

3.1. Exotic neutrino-nucleus events at the COHERENT experiment

The multitarget approach of the COHERENT experiment [10, 11] aiming at neutrino detection can also explore nonstandard physics issues such as NSI [5, 15], neutrino magnetic moment [6], etc. In this subsection, we find it interesting to evaluate the nonstandard neutrino-nucleus events that could be potentially detected by this experiment in each of the proposed nuclear targets. The high intensity SNS neutrino beams [7] and the two promising ν-detectors, liquid ^{20}Ne (391 kg) and liquid ^{40}Ar (456 kg), (located at distance 20 m from the source), constitute excellent probes to search for the exotic ν-reactions. Other possibilities [10, 11] include medium and heavy weight targets like ^{76}Ge (100 kg located at 20 m) and ^{132}Xe (100 kg located at 40 m).

In Figures 1 and 2, the resulting number of exotic events is illustrated and compared with the SM predictions. We note, however, that, especially for the case of the flavour changing (FC) channel, by using the extremely high sensitivity of the ongoing $\mu^- \to e^-$ conversion experiments, Mu2e [20] and COMET [21], very robust bounds have been set on the vector parameters [5]. To this end, we conclude that if the latter experiments will not detect muon-to-electron conversion events, then the new parameters extracted in [5] will lead to undetectable coherent rates at the SNS facility for this channel.

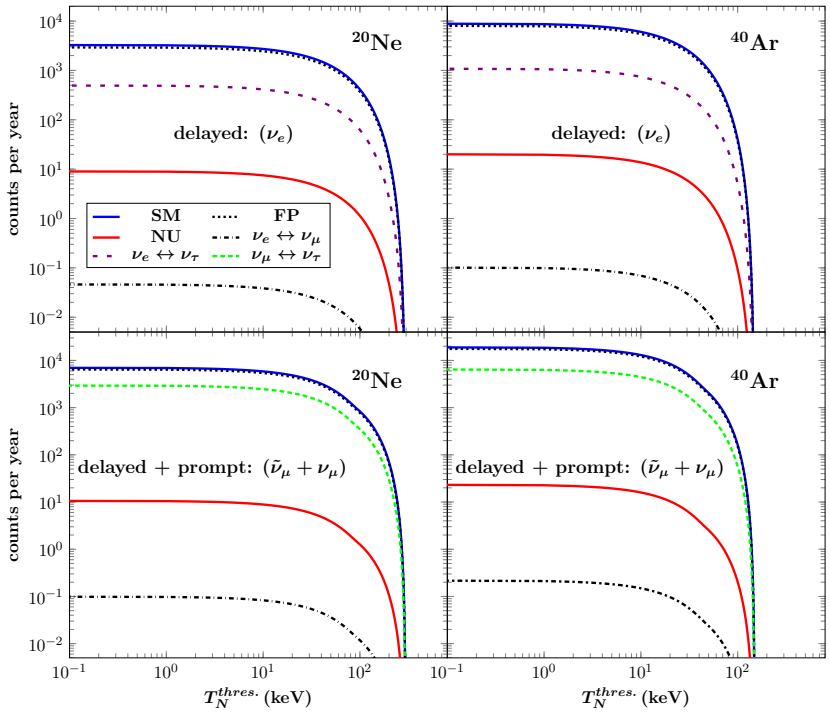

Figure 1: The expected nonstandard neutrino scattering events over the recoil energy threshold at the COHERENT detector, filled with (a) 391kg of liquid ^{20}Ne and (b) 456kg of liquid ^{40}Ar, both located at a distance of 20m ($\Phi_\nu = 2.5 \times 10^7 s^{-1} cm^{-2}$) from the source. A perfectly efficient detector and negligible neutrino oscillation effects are assumed [15].

4. Conclusions

Initially, the evaluation of all required nuclear matrix elements, related to standard model and exotic neutral-current ν-nucleus processes, is formulated, and realistic nuclear structure calculations of ν-nucleus cross sections for a set of interesting nuclear targets are performed. The calculations are concentrated on interesting nuclei, like ^{20}Ne, ^{40}Ar, ^{76}Ge and ^{132}Xe which are important detector materials for several rare event experiments, like the COHERENT at Oak Ridge National Laboratory. Moreover, the QRPA method that considers realistic nuclear forces has been adopted in evaluating the nuclear form factors, for both categories of ν-nucleus processes, the conventional and the exotic ones. Our

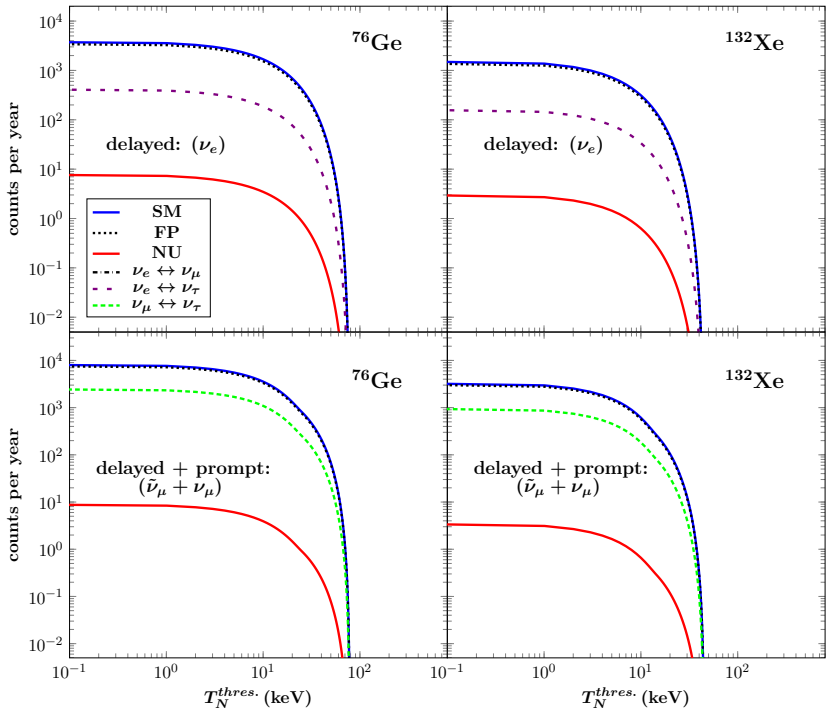

Figure 2: Same as Fig. 1, but for 100kg of ^{76}Ge at 20m ($\Phi_\nu = 2.5 \times 10^7 s^{-1} cm^{-2}$) and 100kg of liquid ^{132}Xe at 40m ($\Phi_\nu = 0.63 \times 10^7 s^{-1} cm^{-2}$) from the source [15].

predictions for the total number of events indicate that, within the current limits of the respective flavour violating parameters, the COHERENT experiment may come out with promising results on NSI.

References

[1] D.Z. Freedman, Phys. Rev. D 9 (1974) 1389.

[2] A. Drukier and L. Stodolsky, Phys. Rev. D 30 (1984) 2295.

[3] J. Schechter, J.W.F. Valle, Phys. Rev. D 22 (1980) 2227; Phys. Rev. D 25 (1982) 774.

[4] J. Barranco, O.G. Miranda and T.I. Rashba, JHEP 0512 (2005) 021.

[5] D.K. Papoulias and T.S. Kosmas, Phys. Lett. B 728 (2014) 482.

[6] K. Scholberg, Phys. Rev. D 73 (2006) 033005.

[7] F.T. Avignone and Y.V. Efremenko, J. Phys. G29, (2003) 2615.

[8] A.A. Aguilar-Arevalo et al., Phys. Rev. D 79 (2009) 072002.

[9] W.C. Louis, Prog. Part. Nucl. Phys. 63 (2009) 51-73.

[10] A. Bolozdynya et al., arXiv:1211.5199.

[11] D. Akimov et al. (CSI Collaboration), arXiv:1310.0125.

[12] S.J. Brice et. al., Phys. Rev. D 89 (2014) 072004.

[13] J.I. Collar et al., arXiv:1407.7524, submitted to Nucl. Instr. Meth. A.

[14] D.K. Papoulias and T.S. Kosmas, J. Phys. Conf. Ser. 410 (2013) 012123.

[15] D.K. Papoulias and T.S. Kosmas, Adv. High Energy Phys. 2014 (2014) 367648.

[16] F. Deppisch, T.S. Kosmas and J.W.F. Valle, Nucl. Phys. B 752 (2006) 80.

[17] D.V. Forero, S. Morisi, M. Tortola, J.W.F. Valle, JHEP 1109 (2011) 142.

[18] O.G. Miranda, M.A. Tortola and J.W.F. Valle, JHEP 0610 (2006) 008.

[19] P.S. Amanik and G.M. Fuller, Phys. Rev. D 75 (2007) 083008.

[20] R.H. Bernstein, P.S. Cooper, Phys. Rept. 532 (2013) 27.

[21] A. Kurup, Nucl. Phys. Proc. Suppl. 218 (2011) 38.

[22] T.S. Kosmas, J.D. Vergados, O. Civitarese and A. Faessler, Nucl. Phys. A 570 (1994) 637.

Symmetry energy effects on isovector properties of neutron rich nuclei with a Thomas-Fermi approach

M.C. Papazoglou and Ch.C. Moustakidis[1]

Department of Theoretical Physics, Aristotle University of Thessaloniki, 54124 Thessaloniki, Greece

Abstract

We employ a variational method, in the framework of the Thomas-Fermi approximation, to study the effect of the symmetry energy on the neutron skin thickness and the symmetry energy coefficients of various neutron rich nuclei. Our approach has the advantage that the isospin asymmetry function $\alpha(r)$ is directly related with the symmetry energy as a consequence of the variational principle. The Coulomb interaction is included in a self-consistent way. We confirm the strong dependence of the symmetry energy on the various isovector properties for the relevant nuclei, using possible constraints between the slope and the value of the symmetry energy at the saturation density.

Keywords:

`thomas-fermi approximation`, `symmetry energy`, `isovector properties`

1. Introduction

The nuclear symmetry energy (SE) is the basic regulator of the isospin properties of the neutron rich nuclei [1, 2]. It is expected to affect the neutron skin thickness, the coefficient of the asymmetry energy in Bethe-Weizsacker formula, e.t.c. In addition, the density dependence of the SE is the main ingredient of the equation of state of neutron rich nuclear matter. However, the experimental data for the SE still remain limited and only for low values of density ($\rho < \rho_0$)

[1] e-mail:moustaki@auth.gr

are accurately constrained. From the theoretical point of view there is an effort to constrain the trend of SE, even for low values of density, from finite nuclei properties and to extrapolate in a way to densities related to neutron stars equation of state (up to $\simeq 5\rho_0$). In any case, the constraints of L or in general the density dependence of SE, even for low values of ρ, are very important for astrophysical applications [2, 3, 4, 5].

The structure of a heavy nucleus is a result of the interplay between the strong short range nuclear forces and long range Coulomb interaction. However, in order to exhibit the isovector character of nuclear forces, we have to focus mainly on heavy and additional neutron rich nuclei. We employ a variational approach, based on the Thomas-Fermi approximation, by suitably constructing an energy density functional, and solving the derived Euler-Lagrange equation. Special attention is devoted to the contribution of the nuclear symmetry energy and the self-consistent treatment of the Coulomb interaction.

2. Energy density functional and variational approach

According to the empirical Bethe-Weizsacker formula the binding energy of a finite nucleus with A nucleons and atomic number Z is given by

$$B(A,Z) = -a_V A + a_S A^{2/3} + a_C \frac{Z(Z-1)}{A^{1/3}} + a_A \frac{(N-Z)^2}{A} + \Delta E_{mic}. \qquad (1)$$

The energy density functional is a natural extension of the above formula, where now the total energy is a functional of the proton and neutron densities and consists of terms corresponding with those appearing in relation (1). The minimization of the total energy defines the related densities and consequently the contribution of each term separately. In the present work we apply the energy density formalism, where the total energy of finite nuclei is a functional of the total density $\rho(r)$ and the isospin asymmetry function $\alpha(r)$, that is

$$E[\rho(r),\alpha(r)] = \int_{\mathcal{V}} \mathcal{E}\left(\rho(r),\alpha(r)\right) d^3r, \qquad (2)$$

where $\mathcal{E}(r)$ is the local energy density. The integration is performed over the total volume $\mathcal{V}$ occupied by the relevant nuclei.

Now we consider the functional

$$E[\rho,\alpha]=\int_{\mathcal{V}}\left[\epsilon_{ANM}(\rho(r),\alpha(r))+F_0|\nabla\rho(r)|^2+\frac{1}{4}\rho(1-\alpha)V_c(r)\right]d^3r. \quad (3)$$

The density $\rho(r)$ and the asymmetry function $\alpha(r)$ must obey the following constraints

$$\int\rho(r)d^3r=A, \qquad \int\alpha(r)\rho(r)d^3r=N-Z. \quad (4)$$

The functional (3) and the constraints (4) constitute a variational problem with constraints.

In the present study we consider the trial function given by the Fermi type formula

$$\rho(r)=\frac{n_0}{1+\exp[(r-d)/w]}. \quad (5)$$

In addition, for the basic ingredients of the energy functional (3) we consider a model where the energy of the symmetric nuclear matter is given by [12]

$$\epsilon_{SNM}(\rho)=\rho T_o\left(au^{2/3}-bu+cu^{5/3}\right), \qquad u=\rho/\rho_0, \quad (6)$$

The total energy density of the asymmetric nuclear matter is

$$\epsilon_{ANM}(\rho,\alpha)=\rho T_o\left(au^{2/3}-bu+cu^{5/3}\right)+\alpha^2\rho Ju^{\gamma}. \quad (7)$$

where $T_o=37.0206$ MeV and $\rho_0=0.16144$ fm^{-3} (the saturation density). The corresponding constants are: $a=-0.08203$, $b=0.97342$ and $c=0.61687$. Here we employ the simple parameterization

$$S(\rho)=S(\rho_0)\left(\frac{\rho}{\rho_0}\right)^{\gamma}=Ju^{\gamma}, \quad S(\rho_0)=J. \quad (8)$$

In this case the parameter γ is related with both the slope L and J by the expression

$$\gamma=\frac{L}{3J}. \quad (9)$$

For each specific set of the Fermi type distribution parameters n_0, d, and w and a given symmetry energy $S(\rho)$, we calculate the asymmetry density $\alpha(r)$ and the total energy of the specific nucleus. After finding the density $\rho(r)$

and asymmetry function $\alpha(r)$ which minimizes the total energy, all the relevant quantities are easily calculated.

In this approach a_A is defined by the integral

$$a_A = \frac{A}{(N-Z)^2} \int \rho(r) S(\rho) \alpha^2(r) d^3r. \tag{10}$$

One of the most important quantities concerning the isovector character of the nuclear forces is the neutron skin thickness defined as

$$R_{skin} = R_n - R_p, \tag{11}$$

with R_n and R_p the neutron and proton and radii respectively defined as

$$R_n = \left(\frac{1}{N} \int r^2 \rho_n(r) d^3r \right)^{1/2}, \qquad R_p = \left(\frac{1}{Z} \int r^2 \rho_p(r) d^3r \right)^{1/2}. \tag{12}$$

Actually, R_{skin} is not directly dependent on $S(\rho)$, compared to the case of a_A, but indirectly via the dependence of $\alpha(r)$. However, recent studies conjecture that R_{skin} is a strong indicator of the isospin character of the nuclear interaction expected to be strongly correlated with the symmetry energy slope L and the value J or in general with the values of the symmetry energy close to the saturation density.

3. Results and Discussion

In the present work we employ a variational treatment of an energy functional, without any additional constraints requiring just the minimization of the binding energy. This approach will be suitable if we intend to impose stronger constraints on the values of L and J and might be of interest for future work.

In Fig. 1, the symmetry energy versus the total density is plotted, according to Eq. (8) for various values of the slope parameter L. It is noted that lower values of L, for low values of densities ($\rho < \rho_0$), correspond to higher values of $S(\rho)$. This behavior of $S(\rho)$ is well reflected on the values of the total binding energy E_{tot} and the asymmetry function $\alpha(r)$.

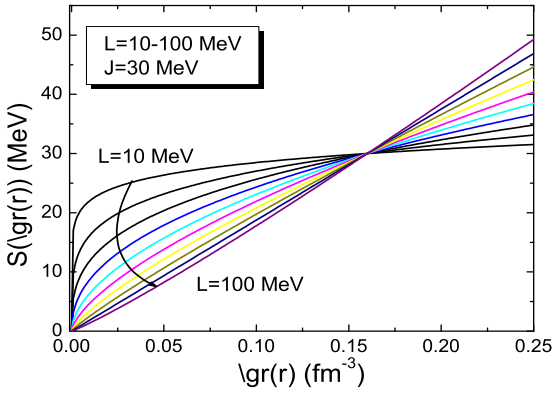

Figure 1: (Color online) The nuclear symmetry energy $S(\rho)$, defined in Eq. (8), as a function of the density ρ for various values of the slope parameter L and the specific value $J = 30$ MeV.

In Fig. 2 we plot the density distributions (total, proton and neutron) as well as the corresponding asymmetry function $\alpha(r)$ for various values of L for(^{208}Pb. The softness symmetry energy (higher values of L) shift the neutron distribution to the outer part of the nucleus, while at the same time it concentrates deeper the protons. The effects of the symmetry energy is even more pronounced on the trend of the asymmetry function.

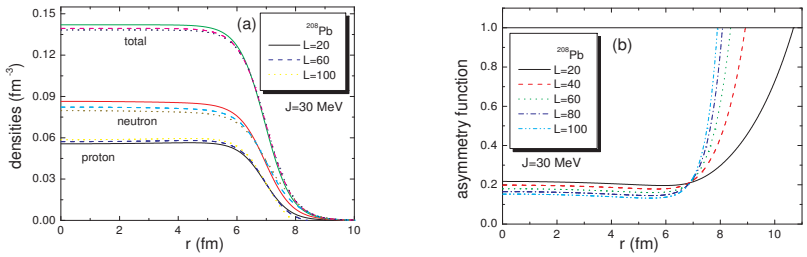

Figure 2: (Color online) The density distribution of neutrons, protons and the total one (2(a) for ^{208}Pb for three values of L (figures 2(a)) and the corresponding asymmetry functions $\alpha(r)$ for a variety of values of L (figures 2(b)

Fig. 3(a) displays the neutron skin R_{skin} as a function of L for various values of J for ^{208}Pb. The most striking feature is, in all cases, the strong dependence of R_{skin} on L. For a comparison, we include for the case of ^{208}Pb an approximate linear dependence

$$R_{skin}(\text{fm}) = 0.101 + 0.00147\ L\ (\text{MeV}), \tag{13}$$

established by Centelles *et. al.,* [7] using a wide range of non-relativistic and relativistic models. It is obvious that relation (13) supports a softer dependence of R_{skin} on L compared to the present study. However we note that we present a systematic study of the effects of L on R_{skin} and in a large range of values of L without trying to reproduce for example the experimental value of the binding energy or the charge radius of the specific nucleus. The Lead Radius Experiment (PREX) at the Jefferson Laboratory has provided the first model-independent evidence for the existence of a neutron-rich skin in ^{208}Pb [10, 11].In addition the large determined neutron skin creates a new open problem concerning the correlation between the nuclear equation of state of nuclear matter and the density functional theory in finite nuclei[8, 9].

In Fig. 3(b) we display the coefficients a_A as a function of L, for various values of J. a_A is a decreasing function of L. Actually, for specific pairs of values of N and Z a softer $S(\rho)$ (high values of L) leads to a lower value of $\alpha(r)$. Obviously, a_A exhibits a mass depended A behavior.

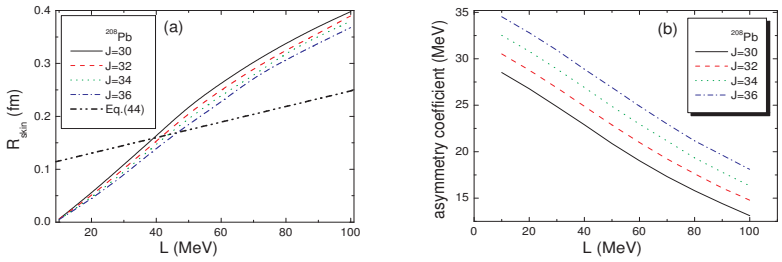

Figure 3: (Color online) (a) The neutron skin R_{skin} for ^{208}Pb as a function of the symmetry energy slope L, for various values of J. (b) The asymmetry coefficient a_A for ^{208}Pb as a function of the symmetry energy slope L for various values of the parameter J.

In Fig. 4 we compare the allowed pairs of L and J constrained from heavy-ion collisions and nuclear structure observable [6] with those found in the present approach. Actually the present results lie inside the intersection area suggested by the measurements of the dipole polarizability a_D as well as those found by heavy-ion collisions experiments.

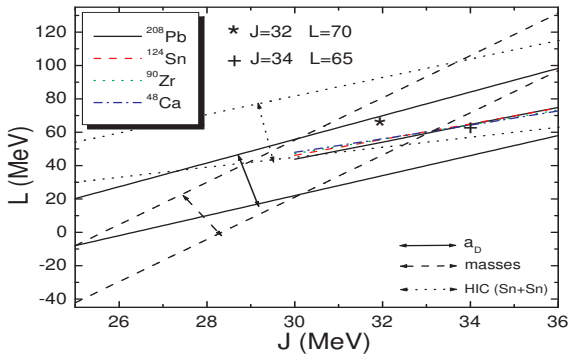

Figure 4: (Color online) Regions of allowed values of pairs J and L (three bands) constrained from heavy-ion collisions (HIC(Sn+Sn) case) and nuclear structure observables (a_D and nuclear masses) (for more details see Ref. [6]) in comparison with the corresponding results constrained from the present approach.

4. Conclusion

In the present work we employ a variational method, in the framework of the Thomas-Fermi approximation, in order to study the symmetry energy effects on isovector properties of various neutron rich nuclei. All the calculated properties are studied as a function of the slope of the symmetry energy and the value of the symmetry energy at the nuclear saturation density. Since, the SE even for low values of nuclear matter is uncertain, the above parameterization is necessary. We find that the neutron skin thickness is very sensitive to L i.e. it increases rapidly with L. This is expected at least in the present approximation, since the main ingredient of the relevant calculated integrals, the function $\alpha(r)$

approaches unity very rapidly close to the critical value of r_c (at the surface of the proton distribution). Our findings, from the present study, show that the experimental knowledge of the symmetry energy at the saturation density J will impose, via the values of the symmetry coefficient a_A, strong constraints on L. In any case, further experimental and theoretical work is necessary for a more detailed exploration of the effects of the symmetry energy on the properties of finite nuclei as well as on the neutron star structure.

References

[1] P. Danielewicz, *et. al.*, Science **298**, 1592 (2002).

[2] J.M. Lattimer and M. Prakash, Phys. Rep. **442**, 109 (2007).

[3] B.A. Li, L.W. Chen, C.M. Ko, Phys. Rep. **464**, 113 (2008).

[4] A.W. Steiner, M. Prakash, J.M. Lattimer, and P.J. Ellis, Phys. Rep. **411**, 325 (2005).

[5] J.M. Lattimer, Annu. Rev. Nucl. Part. Sci. **62**, 485 (2012).

[6] C.J. Horowitz, E.F. Brown, Y. Kim, W.G. Lynch, R. Michaels, A. Ono, J. Piekarewicz, M.B. Tsang, and H.H. Wolter, arXiv:1401.5839 [nucl-th].

[7] M. Centelles, X. Roca-Maza, X. Viñas, and M. Warda, Phys. Rev. Lett., **102**, 122502 (2009).

[8] F.J. Fattoyev and J. Piekarewicz, Phys. Rev. C **86**, 015802 (2012).

[9] F.J. Fattoyev, J. Carvajal, W.G. Newton, and B.A. Li, Phys. Rev. C **87**, 015806 (2013).

[10] S. Abrahamyan, Z. Ahmed, H. Albataineh, K. Aniol, D. Armstrong *et al*, Phys. Rev. Lett., **108**, 112502 (2012).

[11] C. Horowitz, Z. Ahmed, C. Jen, A Rakhman, P. Souder *et al*, Phys. Rev. C **85**, 032501 (2012).

[12] W.D. Myers and W.G. Swiatecki, Phys. Rev. C **57**, 3020 (1998).

Study of ^{nat}Mg(d,d_0) reaction at detector angles between 90° and 170°, for the energy range $E_{d,lab}$=1660-1990 keV

A. Georgiadou, N. Patronis, X. Aslanoglou
Department of Physics, University of Ioannina,
45110 Ioannina, Greece

M. Kokkoris, V. Paneta, R. Vlastou
Department of Physics, National Technical University of Athens, Zografou Campus,
15780 Athens, Greece

M. Axiotis, A. Lagoyannis
Tandem Accelerator Laboratory, Institute of Nuclear Physics, N.C.S.R. Demokritos,
Aghia Paraskevi, 15310 Athens, Greece

P. Misailides
Department of Chemistry, Aristotle University,
GR-54124 Thessaloniki, Greece

Abstract

In the present work, the detailed study of the ^{nat}Mg(d,d_0) is presented for the energy range $E_{d,lab}$=1680-2000 keV (in steps of 5 keV) and for detector angles between 90° and 170°. Elastic scattering data for two forward angles (55° and 70°) were also obtained. The results of the present work are complementary to the recently published ^{24}Mg(d,$p_{0,1,2}$) reaction cross section data utilising the simultaneous depth profiling study of magnesium by d-NRA and EBS methods.

Quantum Phase Transitions and Conformality in nuclear structure

Panagiotis E. Georgoudis
Institute of Nuclear and Particle Physics, National Center for Scientific Research "Demokritos",
GR-15310 Aghia Paraskevi, Athens, and
Physics department, National Technical University of Athens, GR-15780 Zografou Campus, Athens, Greece

Abstract

The $E(5)$ symmetry [1] and the 2nd order shape/phase transition [2] of the Interacting Boson Model [3] will be discussed after the appearance of conformality in the Bohr model [4, 5].

Acknowledgments

Many useful discussions with Piet Van Isacker, Dennis Bonatsos and Francesco Iachello are gratefully acknowledged.

References

[1] F. Iachello, Phys. Rev. Lett. **85**, 17, (2000).

[2] P. Cejnar, J. Jolie and R. F. Casten, Rev. Mod. Phys., **82**, (2010).

[3] F. Iachello and A. Arima, *The Interacting Boson Model Cambridge University Press*, (Cambridge, 1987).

[4] D. Bonatsos, P.E. Georgoudis, D.Lenis, N.Minkov and C.Quesne, Phys. Rev.C **83**, 044321 (2011).

[5] P.E. Georgoudis, Phys. Lett. B731, (2014), 122-125.

Structure of transactinides with relativistic Energy Density Functionals

Vaia Prassa
Department of Physics, University of Zagreb,
10000 Zagreb, Croatia

Abstract

A fully microscopic theoretical framework based on nuclear relativistic energy density functionals (REDFs) [1] is applied to studies of shape evolution, excitation spectra and decay properties of heavy and superheavy nuclei. On the self-consistent mean-field level the microscopic approach is used in the description of rapid shape transitions, from spherical to axial and triaxial, in alpha-decay chains of superheavy nuclei [2, 3]. An especially interesting feature in this region of elements is the possible occurrence of shape-phase transitions and critical-point phenomena. A collective Hamiltonian model [4], based on microscopic REDFs is employed in studies of shape coexistence phenomena, complex excitation patterns and electromagnetic transition rates associated in Hs isotopes with the evolution of shell structures. Microscopic signatures of ground-state shape phase transitions are analyzed [5] using excitation spectra and collective wave functions obtained by diagonalization of a quadrupole collective Hamiltonian, with parameters fully determined by microscopic self-consistent mean-field calculations for triaxial shapes.

Acknowledgments

The author is grateful to Dario Vretenar and Tamara Nikšić for their valuable collaboration. This work has been supported in part by the Finland Distinguished Professor Programme (FiDiPro), and by the MZOS - project 1191005-101

References

[1] T. Nikšić, D. Vretenar, and P. Ring, Phys. Rev. C 78, 034318 (2008)

[2] V. Prassa, T. Nikšić , G. A. Lalazissis, and D. Vretenar, Phys. Rev. C 86, 024317 (2012).

[3] Bing-Nan Lu, En-Guang Zhao, and Shan-Gui Zhou, Phys. Rev. C 85, 011301 (2012).

[4] T. Nikšić, Z. P. Li, D. Vretenar, L. Próchniak, J. Meng, and P. Ring, Phys. Rev. C 79, 034303 (2009).

[5] V. Prassa, T. Nikšić , and D. Vretenar, Phys. Rev. C 88, 044324 (2013).